The Deep Space Network Progress Report 42-47

July and August 1978

October 15, 1978

National Aeronautics and Space Administration

Jet Propulsion Laboratory
California Institute of Technology
Pasadena, California

The Deep Space Network Progress Report 42-47

July and August 1978

October 15, 1978

National Aeronautics and
Space Administration

Jet Propulsion Laboratory
California Institute of Technology
Pasadena, California

The research described in this publication was carried out by the Jet Propulsion Laboratory, California Institute of Technology, under NASA Contract No NAS7-100.

Preface

Beginning with Volume XX, the Deep Space Network Progress Report changed from the Technical Report 32- series to the Progress Report 42- series. The volume number continues the sequence of the preceding issues. Thus, Progress Report 42-20 is the twentieth volume of the Deep Space Network series, and is an uninterrupted follow-on to Technical Report 32-1526, Volume XIX.

This report presents DSN progress in flight project support, tracking and data acquisition (TDA) research and technology, network engineering, hardware and software implementation, and operations. Each issue presents material in some, but not all, of the following categories in the order indicated.

Description of the DSN

Mission Support
- Ongoing Planetary/Interplanetary Flight Projects
- Advanced Flight Projects

Radio Astronomy

Special Projects

Supporting Research and Technology
- Tracking and Ground-Based Navigation
- Communications–Spacecraft/Ground
- Station Control and Operations Technology
- Network Control and Data Processing

Network and Facility Engineering and Implementation
- Network
- Network Operations Control Center
- Ground Communications
- Deep Space Stations
- Quality Assurance

Operations
- Network Operations
- Network Operations Control Center
- Ground Communications
- Deep Space Stations

Program Planning
- TDA Planning

In each issue, the part entitled "Description of the DSN" describes the functions and facilities of the DSN and may report the current configuration of one of the seven DSN systems (Tracking, Telemetry, Command, Monitor & Control, Test & Training, Radio Science, and Very Long Baseline Interferometry).

The work described in this report series is either performed or managed by the Tracking and Data Acquisition organization of JPL for NASA.

Contents

DESCRIPTION OF THE DSN

MISSION SUPPORT

Ongoing Planetary/Interplanetary Flight Projects

SUPPORTING RESEARCH AND TECHNOLOGY

Tracking and Ground-Based Navigation

Communications—Spacecraft/Ground

NETWORK AND FACILITY ENGINEERING AND IMPLEMENTATION

Network

Deep Space Stations

OPERATIONS

Deep Space Stations

Network Functions and Facilities

N. A. Renzetti
Office of Tracking and Data Acquisition

The objectives, functions, and organization of the Deep Space Network are summarized; deep space station, ground communication, and network operations control capabilities are described.

The Deep Space Network was established by the National Aeronautics and Space Administration (NASA) Office of Space Tracking and Data Systems and is under the system management and technical direction of the Jet Propulsion Laboratory (JPL). The network is designed for two-way communications with unmanned spacecraft traveling approximately 16,000 km (10,000 miles) from Earth to the farthest planets and to the edge of our solar system. It has provided tracking and data acquisition support for the following NASA deep space exploration projects: Ranger, Surveyor, Mariner Venus 1962, Mariner Mars 1964, Mariner Venus 1967, Mariner Mars 1969, Mariner Mars 1971, and Mariner Venus-Mercury 1973, for which JPL has been responsible for the project management, the development of the spacecraft, and the conduct of mission operations; Lunar Orbiter, for which the Langley Research Center carried out the project management, spacecraft development, and conduct of mission operations; Pioneer, for which Ames Research Center carried out the project management, spacecraft development, and conduct of mission operations; and Apollo, for which the Lyndon B. Johnson Space Center was the project center and the Deep Space Network supplemented the Manned Space Flight Network, which was managed by the Goddard Space Flight Center. The network is currently providing tracking and data acquisition support for Helios, a joint U.S./West German project; Viking, for which Langley Research Center provides the project management, the Lander spacecraft, and conducts mission operations, and for which JPL provides the Orbiter spacecraft; Voyager, for which JPL provides project management, spacecraft development, and conduct of mission operations; and Pioneer Venus, for which the Ames Research Center provides project management, spacecraft development, and conduct of mission operations. The network is adding new capability to meet the requirements of the Jupiter Orbiter Probe Mission, for which JPL provides the project management, spacecraft development and conduct of mission operations.

The Deep Space Network (DSN) is one of two NASA networks. The other, the Spaceflight Tracking and Data Network (STDN), is under the system management and technical direction of the Goddard Space Flight Center (GSFC). Its function is to support manned and unmanned Earth-orbiting satellites. The Deep Space Network supports lunar, planetary, and interplanetary flight projects.

From its inception, NASA has had the objective of conducting scientific investigations throughout the solar system. It was recognized that in order to meet this objective, significant supporting research and advanced technology development must be conducted in order to provide deep space telecommunications for science data return in a cost effective manner. Therefore, the Network is continually evolved to keep pace with the state of the art of telecommunications and data

handling. It was also recognized early that close coordination would be needed between the requirements of the flight projects for data return and the capabilities needed in the Network. This close collaboration was effected by the appointment of a Tracking and Data Systems Manager as part of the flight project team from the initiation of the project to the end of the mission. By this process, requirements were identified early enough to provide funding and implementation in time for use by the flight project in its flight phase.

As of July 1972, NASA undertook a change in the interface between the Network and the flight projects. Prior to that time, since 1 January 1964, in addition to consisting of the Deep Space Stations and the Ground Communications Facility, the Network had also included the mission control and computing facilities and provided the equipment in the mission support areas for the conduct of mission operations. The latter facilities were housed in a building at JPL known as the Space Flight Operations Facility (SFOF). The interface change was to accommodate a hardware interface between the support of the network operations control functions and those of the mission control and computing functions. This resulted in the flight projects assuming the cognizance of the large general-purpose digital computers which were used for both network processing and mission data processing. They also assumed cognizance of all of the equipment in the flight operations facility for display and communications necessary for the conduct of mission operations. The Network then undertook the development of hardware and computer software necessary to do its network operations control and monitor functions in separate computers. A characteristic of the new interface is that the Network provides direct data flow to and from the stations; namely, metric data, science and engineering telemetry, and such network monitor data as are useful to the flight project. This is done via appropriate ground communication equipment to mission operations centers, wherever they may be.

The principal deliverables to the users of the Network are carried out by data system configurations as follows:

(1) The DSN Tracking System generates radio metric data, i.e., angles, one- and two-way doppler and range, and transmits raw data to Mission Control.

(2) The DSN Telemetry System receives, decodes, records, and retransmits engineering and scientific data generated in the spacecraft to Mission Control.

(3) The DSN Command System accepts spacecraft commands from Mission Control and transmits the commands via the Ground Communication Facility to a Deep Space Station. The commands are then radiated to the spacecraft in order to initiate spacecraft functions in flight.

(4) The DSN Radio Science System generates radio science data, i.e., the frequency and amplitude of spacecraft transmitted signals affected by passage through media such as the solar corona, planetary atmospheres, and plantetary rings, and transmits this data to Mission Control.

The data system configurations supporting testing, training, and network operations control functions are as follows:

(1) The DSN Monitor and Control System instruments, transmits, records, and displays those parameters of the DSN necessary to verify configuration and validate the Network. It provides the tools necessary for Network Operations personnel to control and monitor the Network and interface with flight project mission control personnel.

(2) The DSN Test and Training System generates and controls simulated data to support development, test, training and fault isolation within the DSN. It participates in mission simulation with flight projects.

The capabilities needed to carry out the above functions have evolved in the following technical areas:

(1) The Deep Space Stations, which are distributed around Earth and which, prior to 1964, formed part of the Deep Space Instrumentation Facility. The technology involved in equipping these stations is strongly related to the state of the art of telecommunications and flight-ground design considerations, and is almost completely multimission in character.

(2) The Ground Communications Facility provides the capability required for the transmission, reception, and monitoring of Earth-based, point-to-point communications between the stations and the Network Operations Control Center at JPL, Pasadena, and to the JPL Mission Operations Centers. Four communications disciplines are provided: teletype, voice, high-speed, and wideband. The Ground Communications Facility uses the capabilities provided by common carriers throughout the world, engineered into an integrated system by Goddard Space Flight Center, and controlled from the communications Center located in the Space Flight Operations Facility (Building 230) at JPL.

The Network Operations Control Center is the functional entity for centralized operational control of the Network and interfaces with the users. It has two separable functional elements; namely, Network Operations Control and Network

DSN Radio Science System, Mark III-78

A. L. Berman
TDA Engineering Office

The DSN Radio Science System was created in February 1977, following a successful review of radio science requirements. This article describes the DSN Radio Science System, Mark III-78, as it has evolved in the eighteen months following its inception. Included in the article are the system definition, key characteristics, functional description, and functions of the Deep Space Stations, Ground Communications Facility, Network Operations Control Center, and Network.

Implementation of the "real-time bandwidth reduction," "wideband recording," and "non-real-time bandwidth reduction" capabilities in support of Pioneer Venus Orbiter, Voyager (Jupiter Encounter), and Pioneer Venus Multiprobe is nearing completion. Implementation of the "medium bandwidth recording" capability in support of Voyager (Saturn Ring Experiment) is under way, and is scheduled for completion in May of 1979.

I. Introduction

The DSN Radio Science System, Mark III-78, is one of eight DSN Data Systems which provide major data types and functional capabilities to the flight projects. In the broadest sense, the DSN Data Systems encompass the equipment, software, personnel, documentation, procedures, and resources necessary to deliver the required data to the flight projects. The Radio Science System was brought into existence on February 4, 1977, when the system requirements were reviewed and accepted by the Radio Science Review Board. The February 4, 1977 Radio Science Requirements Review has been described by Mulhall (Ref. 1).

This article describes the DSN Radio Science System as it has evolved in the eighteen months since its inception. Included in this article are the system definition, key characteristics, functional description, system configuration, testing, implementation status, and system schedule.

A. DSN Definition of Radio Science

The formal DSN definition of *Radio Science* is as follows:

> The acquisition and extraction of information from spacecraft transmitted signals which have been directly affected by passage through:
>
> (1) Planetary neutral atmospheres
>
> (2) Planetary ionospheres
>
> (3) Planetary magnetospheres
>
> (4) Solar corona (plasma)
>
> (5) Gravitation (relativity)
>
> (6) Interplanetary media
>
> (7) Planetary rings (particles)

Data Processing. The functions of the Network Operations Control are:

(1) Control and coordination of Network support to meet commitments to Network users.

(2) Utilization of the Network data processing computing capability to generate all standards and limits required for Network operations.

(3) Utilization of Network data processing computing capability to analyze and validate the performance of all Network systems.

The personnel who carry out the above functions are located in the Space Flight Operations Facility, where mission operations functions are carried out by certain flight projects. Network personnel are directed by an Operations Control Chief. The functions of the Network Data Processing are:

(1) Processing of data used by Network Operations Control for control and analysis of the Network.

(2) Display in the Network Operations Control Area of data processed in the Network Data Processing Area.

(3) Interface with communications circuits for input to and output from the Network Data Processing Area.

(4) Data logging and production of the intermediate data records.

The personnel who carry out these functions are located approximately 200 meters from the Space Flight Operations Facility. The equipment consists of minicomputers for real-time data system monitoring, two XDS Sigma 5s, display, magnetic tape recorders, and appropriate interface equipment with the ground data communications.

and indirectly affected by forces acting upon the spacecraft:

(8) Gravity waves

(9) Gravitational fields

(10) Planetary atmospheric winds (e.g., Pioneer Venus wind experiment)

(11) Solar radiation (solar sailing)

It should be noted that the DSN Radio Science System specifically *excludes* the often confused *Radio Astronomy* functions which are, according to the formal DSN definition, as follows:

> The acquisition and extraction of information from signals emitted or reflected by natural sources (i.e., all sources other than spacecraft), such as:
>
> (1) Planetary radar
>
> (2) Planetary and lunar observations
>
> (3) Discrete radio sources (pulsars, quasars, K-band, X-ray burst, etc.)
>
> (4) Interstellar observations (formaldehyde, molecular lines, dark cloud recombination lines, etc.)

B. Origins of the DSN Radio Science System

The DSN Radio Science System traces its roots to the Pioneer Venus Mission, which includes two radio science experiments with major impact on the DSN. A brief description of these experiments and their resulting impact ensues.

In December 1978 the Pioneer Venus Multiprobe Mission Spacecraft will encounter the planet Venus. At that time, the Differential Long Baseline Interferometry (DLBI) experiment will attempt to measure wind velocities in the atmosphere of Venus as four probes descend through the atmosphere. Also starting in December 1978, the Pioneer Venus Orbiter will undergo daily occultations by Venus for a period of approximately three months. In addition, a smaller period of occultations occurs in May 1979.

As the Pioneer Venus Mission planning evolved, it became clear that the DLBI experiment would require that the signals from the four descending probes and the spacecraft be received on one high-phase stability, wideband (~2 MHz) open-loop receiver, and that the output of this receiver be recorded on a high-precision, very high-rate recorder. In addition, it was also clear that costs associated with processing approximately 100 S- and X-band occultations of the Pioneer Venus orbiter by previously used techniques would be quite burdensome. To reduce these costs, the idea was conceived of driving the open-loop receiver first local oscillator with the predicted (atmospherically refracted) frequency, so that only a very narrow open-loop receiver output bandwidth would need to be recorded. Since processing costs are approximately linear with recorded bandwidth, this procedure would be expected to result in substantial savings.

As a result of these new radio science experiment requirements it became apparent that it would be appropriate for the DSN to create a Radio Science System. The equipment which will perform "real-time bandwidth reduction"[1] and wideband recording was combined to form the DSS Radio Science Subsystem (DRS) at 64-meter subnet stations.

In addition, it was decided that non-real-time bandwidth reduction of the wideband radio science data (DLBI data) would be performed at the Jet Propulsion Laboratory, Pasadena. The necessary equipment was located at the Compatibility Test Area (CTA 21), and constitutes the CTA 21 Radio Science Subsystem (CRS).

It should be emphasized that although the initial implementation of the Radio Science System is geared toward the Pioneer Venus mission, the Radio Science System provides multimission radio science capabilities, and will be extensively utilized in fulfillment of the radio science requirements of other projects, such as Viking, Voyager, Galileo, etc.

C. Flight Project Users of the DSN Radio Science System

Flight projects with active spacecraft which will be supported by the Radio Science System are as follows:

(1) Viking

(2) Pioneer Venus

(3) Voyager

(4) Pioneer Saturn

New or anticipated flight projects which can be expected to utilize the Radio Science System are:

(1) Galileo

(2) Solar Polar

[1]The expression "real-time bandwidth reduction" is defined as the process of driving the open-loop receiver local oscillator with frequency predictions, and subsequently filtering, digitizing, and recording a narrow bandwidth containing the (mixed) signal.

II. Radio Science System Definition

The DSN Radio Science System is defined as follows:

> The DSN Radio Science System generates radio science data (digitized amplitude samples) from spacecraft signals which are both left circularly polarized (LCP) and right circularly polarized (RCP) and are at S-band and X-band frequencies. The radio science data bandwidth is reduced in either real-time or non-real-time via differencing with a predicted signal profile. Bandwidth reduced radio science data are delivered to the project via computer compatible magnetic tape (Intermediate Data Record).
>
> The DSN Radio Science System additionally provides graphical displays in real-time of both radio metric and radio science data.

It should be noted that radio metric data (Doppler, Range, etc.) constitutes prime radio science information. However, all radio metric data is and will continue to be delivered by the DSN *Tracking* System.

Figure 1 presents the Radio Science System functions and interfaces. The Radio Science System functional block diagram is presented in Fig. 2. Note that Fig. 2 also includes DSN Tracking System functional capabilities which deliver the closed-loop radio science (radio metric) data. Finally, Fig. 3 presents the Radio Science System functions and data flow.

III. Radio Science System Key Characteristics

The key characteristics of the DSN Radio Science System, Mark III-78, are as follows:

(1) Acquires left and right circularly polarized spacecraft signals at S- and X-bands.

(2) Digitizes and bandwidth reduces up to four open-loop receiver channels simultaneously via use of automatically controlled programmed oscillator.

(3) Digitizes and records wideband open-loop receiver output.

(4) Generates programmed oscillator frequency predictions which incorporate effects due to planetary atmospheres.

(5) Performs real-time system performance monitoring and provides system performance data in real-time to the project.

(6) Provides transmission of radio science data from Deep Space Station (DSS) to Network Operations Control Center (NOCC) via High-Speed Data Line (HSDL).

(7) Performs non-real-time bandwidth reduction of wideband radio science data.

(8) Provides wideband back-up of all unique radio science events.

(9) Provides radio science data to the project via Intermediate Data Record (IDR).

IV. Radio Science System Functional Description

Major functional capabilities of the DSN Radio Science System, Mark III-78, can be conveniently categorized as follows:

(1) Wideband recording and subsequent non-real-time bandwidth reduction (Pioneer Venus DLBI Experiment).

(2) Real-time bandwidth reduction (planetary occultations and solar corona operations).

(3) Medium bandwidth recording (planetary ring operations).

(4) System performance validation.

These are described in detail below.

A Wideband Recording and Subsequent Non-Real-Time Bandwidth Reduction

Multiple probe signals are acquired by the Wideband (~2 MHz) Multimission Open-Loop Receiver (MMR). These signals are digitized and recorded on a high-rate, high-precision digital recorder (the Digital Recording Assembly, or DRA). The DRA recorded tapes are shipped via Network Information Control (NIC) to CTA 21, where the (radio science) data bandwidth is reduced via CTA 21 Radio Science Subsystem (CRS) processing. The final digital, bandwidth-reduced data are supplied to the project on computer compatible magnetic tape ("Wideband Radio Science" IDR). References 2, 3, and 4 describe in detail the MMR, DRA, and CRS, respectively.

B. Real-Time Bandwidth Reduction

Real-time bandwidth reduction starts with provision of a spacecraft state vector to the "POEAS" software program. The output of the POEAS program is a Polynomial Coefficient Tape (PCT), which includes the frequency-independent, planetary atmosphere-refracted spacecraft observables. The

PCT is input to the Network Control (NC) Support Subsystem software program "PREDIK." The output of PREDIK is radio science formatted downlink frequency predictions, which are transmitted to the appropriate 64-m DSS via High-Speed Data Line (HSDL). The predictions are received by the Occultation Data Assembly (ODA) of the DSS Radio Science Subsystem (DRS). The ODA processes the predictions and provides them to the Programmed Oscillator Control Assembly (POCA). The POCA drives a Programmed Oscillator (PO), the output of which is multiplied up to S-band and X-band in a two-channel open-loop receiver (either the Block III OLR at DSSs 14 and 43, or the new narrow bandwidth MMR at DSS 63) and mixed with the two (S- and X-band) spacecraft downlinks. The open-loop receiver filters the baseband product(s) of the mixing, and provides the filtered signals to the ODA. The baseband signals are digitized and recorded on magnetic tape along with the counted output of the PO. During actual operations, the ODA recorded data are validated via usage of the Signal Spectrum Indicator (SSI). After data acquisition is complete, the ODA formats the data for HSDL transmission to the GCF Data Records Subsystem (GDR). The real-time bandwidth reduced data are supplied on computer compatible tape ("Radio Science" IDR) to the appropriate flight project.

Radio science predictions are further described in Ref. 5, while Ref. 3 describes ODA operations in detail.

C. Medium Bandwidth Recording

Generation of radio science predictions and subsequent handling by the ODA, POCA, and PO are the same as described in Subsection B. In this case, however, four spacecraft signals (permutations of LCP and RCP, and S- and X-band) are acquired by the four-channel Narrow Bandwidth MMR, and mixed with appropriate PO frequencies. The mixed product(s) are filtered and provided to the DRS. Within the DRS, the signals are digitized and recorded on the DRA. During data acquisition, the recorded signals are verified via use of the SSI. Subsequent to data acquisition, the ODA reformats the DRA recorded data and re-records it on computer compatible tape. The data are finally provided to the project via computer compatible tape ("Medium Bandwidth Radio Science" IDR).

D. System Performance Validation

Digital spectrum (radio science) data from the Spectral Signal indicator (SSI) are provided to the Occultation Data Assembly (ODA), where they are formatted for HSDL transmission to the NOCC. The digital spectrum data are routed to the NC Radio Science Subsystem (NRS) which processes the data to form a replica of the original (SSI) spectral display. The NC Display Subsystem (NDS) displays the spectra in the Network Operations Control Area (NOCA) and, additionally, provides the displays to the appropriate project area(s) for viewing by radio science experimentors. Additionally, the NRS provides displays of the DRS status and configuration.

Display of radio science data and radio science equipment status is described in greater detail in Ref 6.

V. Deep Space Station Functions

A. DSS Antenna Mechanical Subsystem (ANT)

The DSS Antenna Mechanical Subsystem points the antenna at spacecraft via NOCC generated tracking predictions, and collects and focuses spacecraft signal energy at S- and X-band frequencies.

B. DSS Antenna Microwave Subsystem (UWV)

The DSS Antenna Microwave Subsystem performs low noise amplification of left and right circularly polarized signals at both S- and X-band frequencies.

C. DSS Receiver-Exciter Subsystem (RCV)

The DSS Receiver-Exciter Subsystem acquires via open-loop receivers left and right circularly polarized signals at both S- and X-band frequencies. The signals are hetrodyned down to baseband via use of automatically controlled Programmed Oscillators, filtered, and provided to the DSS Radio Science Subsystem (DRS). The RCV displays DRS provided signals on the Spectrum Signal Indicator (SSI) for purposes of validation of DRS operations.

D. DSS Radio Science Subsystem (DRS)

The DSS Radio Science Subsystem digitizes, bandwidth reduces and records radio science data, and digitizes and records wideband radio science data. The DRS receives radio science predictions from NOCC, configuration and control data from the DSS Monitor and Control Subsystem, and signals from the DSS Receiver-Exciter Subsystem. The DRS provides radio science data and wideband radio science data to NOCC, status and configuration data to the DSS Monitor and Control Subsystem, and Programmed Oscillator frequencies to the Receiver-Exciter Subsystem.

E. DSS Monitor and Control Subsystem (DMC)

The DSS Monitor and Control Subsystem provides control data to the DRS, receives and displays DRS status data, and transmits DRS status data to NOCC.

VI. Ground Communications Facility (GCF) Functions

A. High-Speed Data Subsystem (HSDS)

The High-Speed Data Subsystem transmits radio science predictions from the NOCC to the DSS and CTA 21, and radio science data from the DSS to NOCC.

B. GCF Data Records Subsystem (GDR)

The GCF Data Records Subsystem generates and provides to the flight projects radio science Intermediate Data Records (IDRs).

VII. Network Operations Control Center Functions

A. NC Radio Science Subsystem (NRS)

The NC Radio Science Subsystem generates open- and closed-loop radio science DTV graphics displays, and DRS status and configuration displays.

B. NC Display Subsystem (NDS)

The NC Display Subsystem provides NRS generated radio science displays to the Network Operations Control Area (NOCA) and project radio science areas, and provides control data to the NRS.

C. NC Support Subsystem (NSC)

The NC Support Subsystem generates radio science predictions for transmission to the CTA 21 and DSS Radio Science Subsystems.

VIII. Network Functions

A. CTA 21 Radio Science Subsystem (CRS)

The CTA 21 Radio Science Subsystem bandwidth reduces wideband radio science data recorded at the DSS. The CRS receives digital wideband radio science data from the DSS Radio Science Subsystem and provides bandwidth reduced radio science data to the flight projects via wideband radio science Intermediate Data Records (IDRs).

IX. Radio Science System Performance Testing

Radio Science end-to-end system performance testing will be accomplished by comparing open-loop frequency data generated by the Radio Science System to closed-loop frequency data generated by the Tracking System. These tests are described in detail in Ref. 7.

X. Implementation Status

The real-time bandwidth reduction and wideband recording capabilities have been implemented at DSSs 14 and 43, and NOCC. Non-real-time bandwidth reduction capability has been implemented at CTA 21. Major (planned) implementation milestones in the coming year are as follows:

(1) December 1, 1978
Real-time bandwidth reduction at DSS 63.

(2) February 1, 1979
Wideband recording at DSS 63.

(3) May 1, 1979
Four channel open-loop receiving capability at DSS 14, medium bandwidth recording capability at DSSs 14, 43, and 63, and remote spectrum display in NOCC.

References

1. Mulhall, B. D. L., "DSN Radio Science System Description and Requirements," in *The Deep Space Network Progress Report 42-39*, pp. 119-129, Jet Propulsion Laboratory, Pasadena, Calif., June 15, 1977.

2. Nishimura, H., "Pioneer Venus Wind Experiment Receiver," in *The Deep Space Network Progress Report 42-38*, pp. 141-147, Jet Propulsion Laboratory, Pasadena, Calif., Apr. 15, 1977.

3. Berman, A. L., "The DSS Radio Science Subsystem – Real-Time Bandwidth Reduction and Wideband Recording of Radio Science Data," in *The Deep Space Network Progress Report 42-44*, pp. 180-188, Jet Propulsion Laboratory, Pasadena, Calif., Apr. 15, 1978.

4. Berman, A. L., and Molinder, J. I., "The CTA 21 Radio Science Subsystem – Non-Real-Time Bandwidth Reduction of Wideband Radio Science Data," in *The Deep Space Network Progress Report 42-41*, pp. 127-134, Jet Propulsion Laboratory, Pasadena, Calif., Oct. 15, 1977.

5. Berman, A. L., "Planetary Atmosphere Modeling and Predictions," in *The Deep Space Network Progress Report 42-42*, pp. 125-129, Jet Propulsion Laboratory, Pasadena, Calif., Dec. 15, 1977.

6. Berman, A. L., "DSN Radio Science System Mark III-78 Real-Time Display Capability," in *The Deep Space Network Progress Report 42-40*, pp. 141-145, Jet Propulsion Laboratory, Pasadena, Calif., Aug. 15, 1977.

7. Berman, A. L., and Mehta, J. S., "System Performance Testing of the DSN Radio Science System, Mark III-78," in *The Deep Space Network Progress Report 42-43*, pp. 129-133, Jet Propulsion Laboratory, Pasadena, Calif., Feb. 15, 1978.

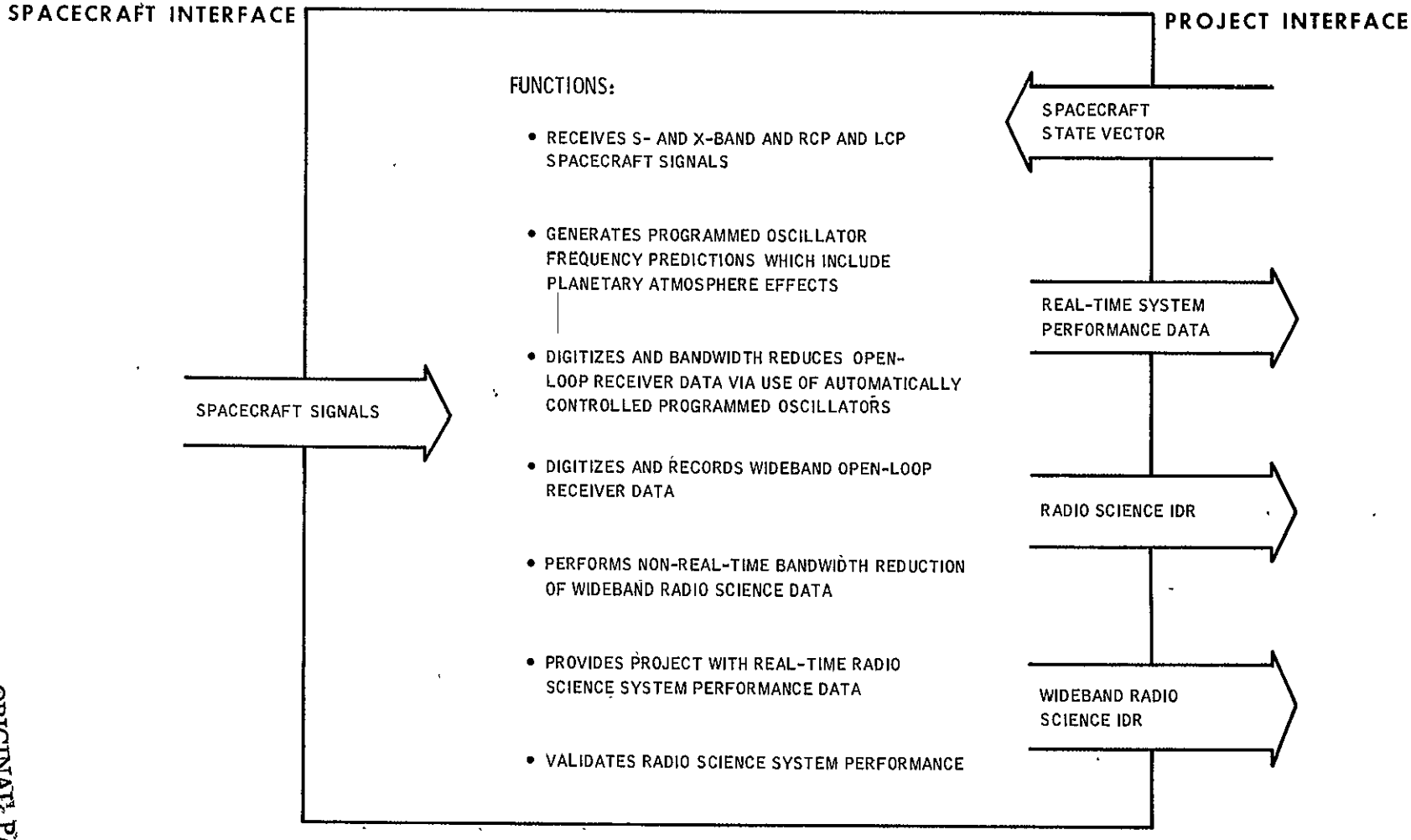

Fig. 1. DSN Radio Science System functions and interfaces

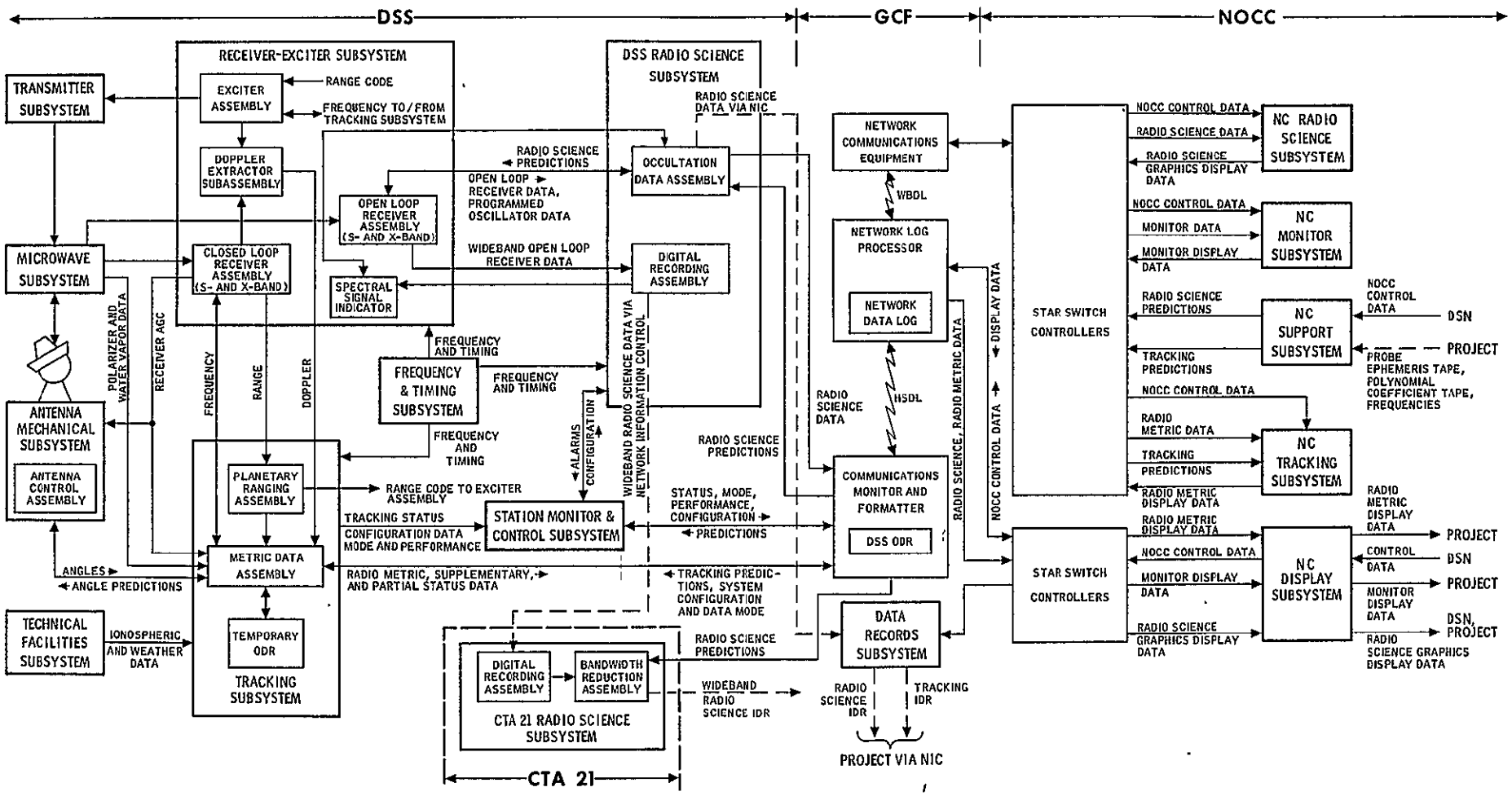

Fig 2 DSN Radio Science System Mark III-76 functional block diagram

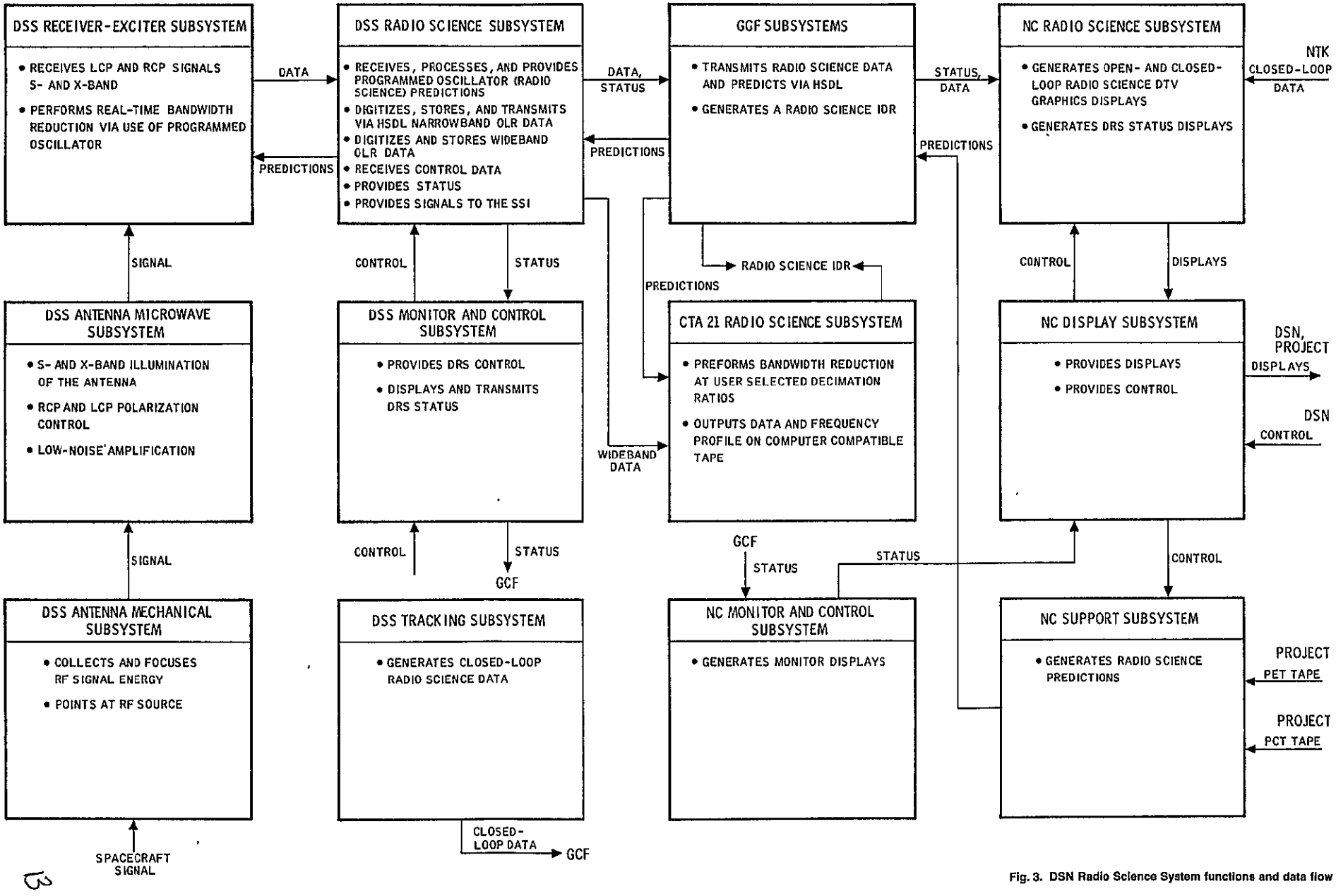

Fig. 3. DSN Radio Science System functions and data flow

Preceding page blank

Viking Extended Mission Support

R. L. Gillette
Deep Space Network Operations Office

This article covers the period from May 1 through June 30, 1978. It reports on DSN support of Viking spacecraft activities during the period and continues reporting on the DSN Viking Command and Tracking support.

I. Introduction

A. Status

The Viking Orbiter 1 (VO-1) spacecraft continued to operate as expected during this reporting period as it collected and returned to Earth weather data and Mars photos as well as relaying to Earth data from the two Viking Landers.

Due to serious gas leaks in the roll-axis control jets the Viking Orbiter 2 (VO-2) spacecraft continued, during the major portion of this reporting period, in a roll drift mode of operation. In the roll drift mode of operation the roll control jets are disabled, allowing the spacecraft to slowly roll as it revolves around Mars. During the roll drift mode the VO-2 spacecraft cannot observe Mars with its science instruments. However, engineering data monitoring the status of the spacecraft continues to be transmitted to Earth.

On June 17 and continuing for an eight-day period, the VO-2 spacecraft was brought out of the roll drift mode of operation to obtain water vapor and temperature measurements in a high latitude region of Mars. VO-2 was returned to a roll drift mode of operation to conserve its nearly exhausted supply of attitude-stabilizing gas for one more science sequence, starting 20 July.

Both Viking Lander spacecrafts (VL-1 and VL-2) were placed in a six-month automatic mode of operation (VL-1 on May 25 and VL-2 on June 15 during this reporting period). During this six-month period few or no instructions will be sent from Earth. Both Landers will send periodic information about weather, soil chemistry calibrations and some photos, mainly to check hazes and clouds in the martian sky.

B. First Commanding from On-Board Telemetry Processing

On March 23, 1978, VO-2 developed a major leak in one of the yaw axis control gas jets. Attempts to clear the leak were unsuccessful and, within a 12-h period, over 6 months supply of gas was lost. To reduce gas consumption, thereby making it possible to save the spacecraft for its final science observations during June and late July, the spacecraft was placed in the roll drift mode of operation.

During roll drift, various stimuli such as solar pressure and gravity gradients during periapsis gradually build up the roll rate to a point where attitude control gas is used at high rates. As a result, periodic roll maintenance is required to slow the rate down. Roll maintenance consists of going to roll inertial

mode of control to stabilize the roll axis with a probable recurrence of another roll valve leak. Because round trip signal times are in excess of 30-min, it is possible to have a leak occur during roll drift maintenance, depleting the remaining gas supply prior to discovery and corrective action by ground command.

To solve this problem, the Viking Orbiter flight software in the Computer Command Subsystem (CCS) was updated to provide for downlink telemetry monitoring. During roll maintenance on May 8 and June 1 the Orbiter 2 spacecraft Computer Command Subsystem successfully issued a series of commands to the Attitude Control Subsystem as a result of the onboard telemetry monitoring. Both the May 8 and June 1 operations were successful on the first try. Backup procedures were available to clear the valve by a series of ground commands if necessary, but they were not needed. The spacecraft automatically terminated roll drift, sampled the data, checked for leaks and returned the spacecraft from roll inertial to roll drift mode.

These operations were the first JPL onboard processing of telemetry data which resulted in spacecraft commanding and as such they represent a milestone in spacecraft operations. Until this time all responses to unusual circumstances have been specified prior to launch and implemented with either subsystem internal design or hardwired interrupts from the subsystem to the CCS. Using telemetry monitoring, a large number of parameters or functions of sets of parameters can be used to control the spacecraft autonomously.

C. Viking Continuation Mission

The primary missions of Viking were terminated on November 15, 1976, at the time of solar conjunction because of the imminent loss of the communication links between Mars and Earth. By December 15, 1976, communication was reestablished and the "Extended Mission" commenced.

The Viking Extended Mission terminated on May 31, 1978. Since both Orbiters and Landers were still operational, funding was approved for a continuation of the Viking mission for another nine months at a reduced level and with a much smaller flight team. The Viking Continuation Mission (VCM) project will be managed by JPL.

The objectives of the Viking Continuation Mission are essentially the same as those of Extended Mission, but with a shift of emphasis more toward Orbiters than Landers. The major goal is to complete one full Mars year of observation of the planet, including filling in the season that was obscured by solar occultation at the end of the Primary Mission, and to make a start on determining the extent to which weather conditions repeat themselves in succeeding years.

During the Continuation Mission both Landers will be in the automatic mission mode, performing repetitive observations. Data will be acquired from imaging, meteorology and seismology experiments. The Lander loaded science missions will terminate on or before December 1, 1978, but at least one Lander will be left in a state such that its data can be read out over the direct link occasionally, and range measurements to it can continue to be made for at least another year.

All three Orbiter science experiments will be continued, but their observational sequences will be simpler and more repetitious than previously. After December 1, 1978, their operation will either be terminated or still further reduced. The operational aspects of the Viking Mission are currently planned to terminate on February 28, 1979. Figure 1 shows the Viking Continuation Mission Profile strategy.

D. Radio Science

Radio science activities and experimentation continued during May and June. These activities include near-simultaneous Lander/Orbiter ranging, VO-1 and -2 Earth occultation coverage, and the Gravity Field Experiment.

During the Viking Continuation Mission radio science investigations, including the occultation experiment, the local gravity anomaly experiment, and Lander ranging, will continue, and in December, January and February, which is the next solar conjunction period, the solar corona and relativity experiments will be repeated.

II. Network Support

Table 1 shows the DSN tracking support for January through June 1978. During the May and June period over 75% of the DSN support was from the 64-m network. This is primarily due to the Earth-Mars distance, which requires the additional 8-dB antenna gain to obtain the Viking high-rate telemetry data. Noticeable also during the May and June period is the reduction in total DSN tracking support, which follows the basic guidelines of a reduced level of operations during the Continuation Mission.

Table 2 gives the total number of commands transmitted by the DSN for the Viking Project during January through June 1978. The reduction in number of commands transmitted in May and June again reflects the reduction in Viking operations for the Continuation Mission.

Figure 2 shows the performance of the DSN delivery of the telemetry Intermediate Data Record (IDR) during the Viking Extended Mission. The IDR is a magnetic tape of digital telemetry data produced by the DSN. As a goal, within exist-

ing time constraints, the DSN attempts to provide 100% of the data recorded at the Deep Space Station on the Digital Original Data Record (DODR) magnetic tape. IDR's are required to be delivered within 24-h following the end of a stations pass.

During the Viking Extended Mission the data content of the IDR exceeded 99.5%. Average delivery time was between 4 to 10-h until February 1978, at which time the IDR delivery time steadily increased but never exceeded the committed 24-h delivery requirement. Several reasons contribute to the increase in delivery times. Primarily the change was due to the increased work load in the Network Data Processing Area (NDPA) brought on by the Voyager and Pioneer Venus Project priorities and the new radio metric IDR requirements. Another major contributing factor was the change in the maintenance and operations contract changeover, resulting in the loss of qualified personnel and the need to train their replacements.

Table 1. VEM Tracking Support, 1978

DSS	Jan	Feb	Mar	Apr	May	Jun	Jul	Aug	Sept	Oct	Nov	Dec
					Tracks/Hours							
11	8/72	–	19/167	–	18/164	1/1						
12	–	4/13	5/22	1/8	–	–						
14	40/319	25/218	37/272	47/365	25/231	34/242						
42	22/166	23/76	30/201	30/192	2/4	–						
43	57/294	14/207	15/68	27/163	40/281	46/346						
44	–	11/51	6/43	–	11/77	3/17						
61	10/88	38/243	25/281	15/159	2/26	–						
62	6/27	2/25	3/22	3/29	8/75	3/33						
63	13/101	21/181	30/293	42/440	26/206	41/343						
Total	156/1067	138/1014	170/1369	165/1356	132/1064	128/982						

Note: Numbers of tracks represent the summation of all Viking spacecraft tracked. Track times, in hours, represent scheduled station support.

Table 2. Number of commands transmitted in Viking extended mission during January through June 1978

DSS	Jan	Feb	Mar	Apr	May	Jun
11	1947	–	119	–	1628	6
12	–	1	1	374	–	–
14	4565	1079	1326	3032	2845	1214
42	1447	1305	261	1079	0	0
43	1593	1732	124	275	1326	1567
44	–	255	3	–	373	0
61	992	3548	1073	1503	0	0
62	1	1006	461	73	0	960
63	895	128	2597	4005	669	2451
Total	11440	9054	5965	10341	6841	3198

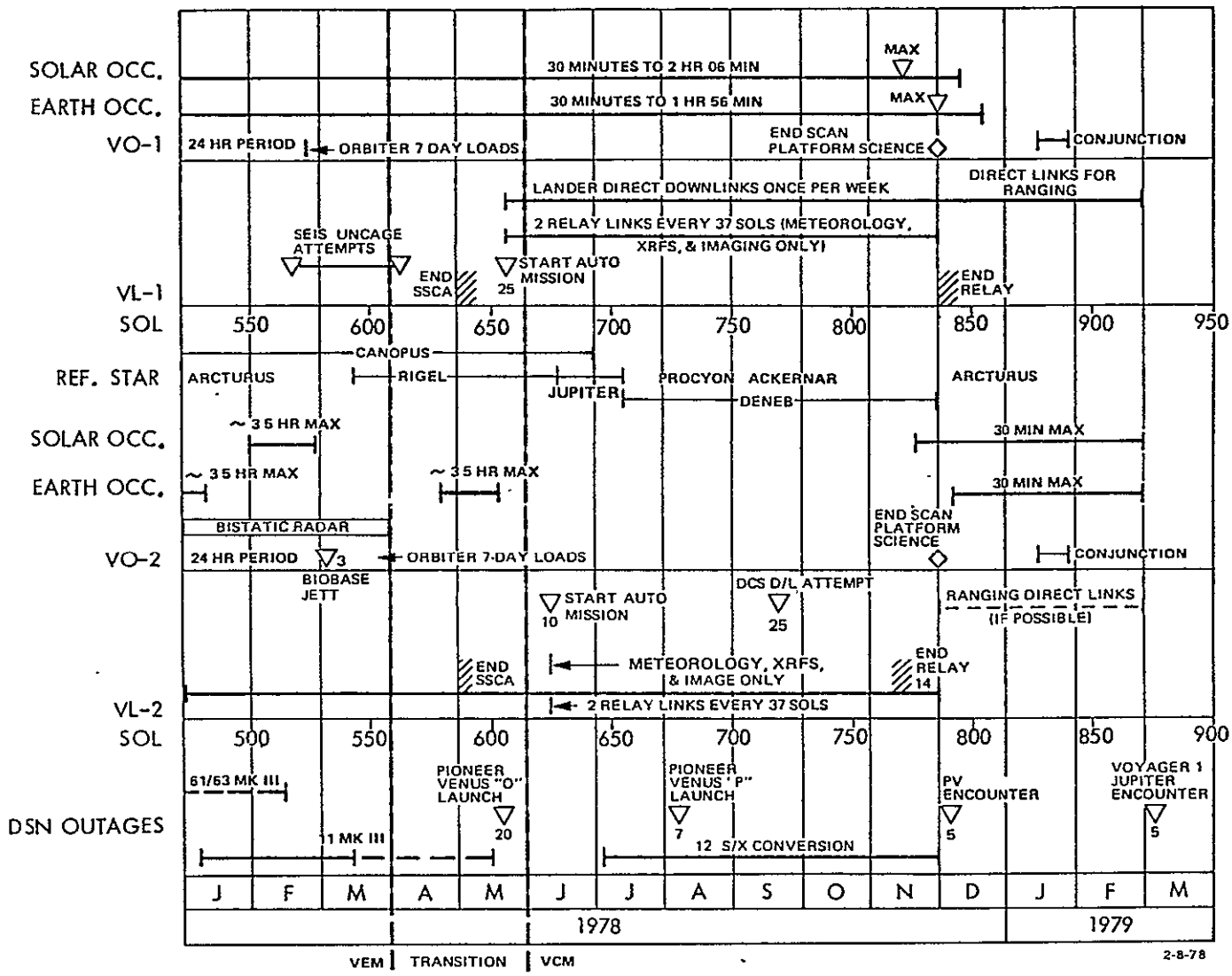

Fig. 1. Viking Continuation Mission profile strategy

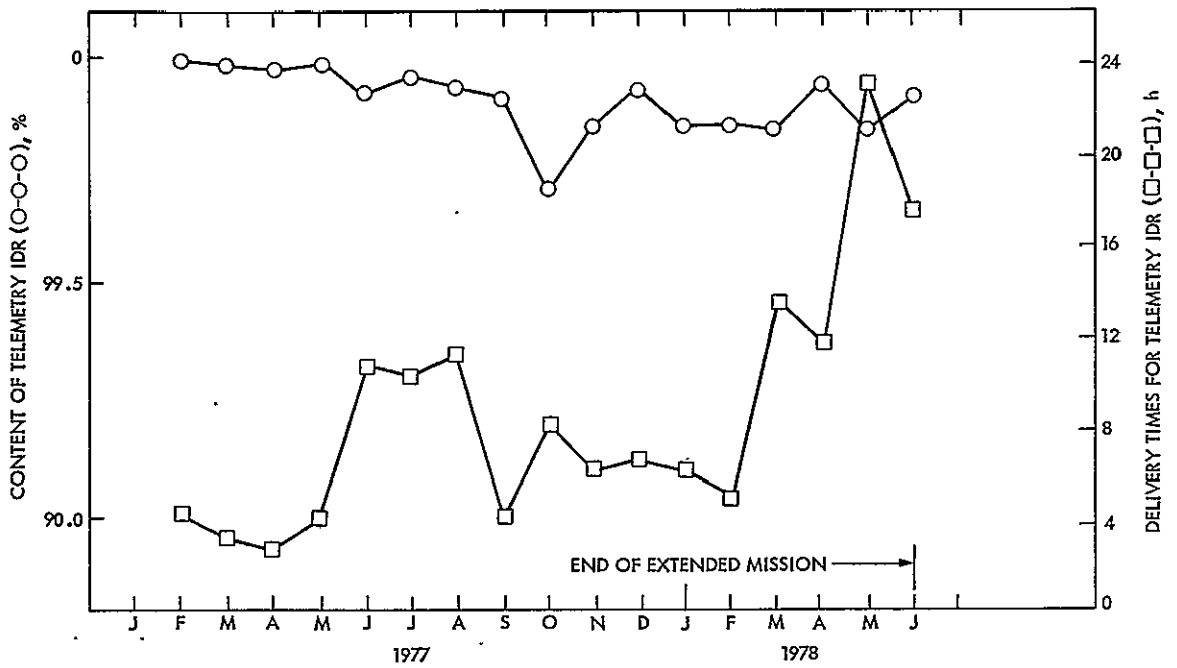

Fig. 2. Viking Extended Mission telemetry IDR performance

Pioneer 10 and 11 Mission Support

R. B. Miller
TDA Mission Support Office

The current estimates of the Deep Space Network performance capability in tracking Pioneer 10 to the telecommunications limit and for Pioneer 11 Saturn encounter are discussed.

I. Introduction

The topic discussed here was previously discussed in a 1976 DSN Progress Report article (Ref. 1). Since the time of that article, the Pioneer 10 spacecraft has thresholded on the DSN 26-meter stations and considerable in-flight measured performance data have been gathered. New estimates of expected performance capability, based on the measured performance, indicate that for a 64-meter station with a 22-deg system noise temperature tracking above 30-deg elevation it should be possible to track Pioneer 10 spacecraft out to 34 AU, which will be reached by the spacecraft in the first part of 1985. This is over 5 AU farther than earlier estimates.

Unfortunately, revision of the Pioneer 11 expected performance at Saturn encounter, based on in-flight experience, has resulted in a reduction in estimated performance at Saturn which makes the Project's desired objective of 1024 b/s at Saturn appear to be out of reach with any practical performance improvements that could be achieved in the time available. It now appears that the new low-noise cones which will be installed prior to Saturn encounter (and were planned with the intention of trying to achieve 1024 b/s will be required just to make 512 b/s marginally possible.

II. Projected Spacecraft Life

The Pioneer 10 spacecraft is projected to have sufficient attitude control propellant (necessary for antenna pointing) out to 1989. The end-of-life projected by the Project is based on when the radioisotope thermoelectric generators (RTG) are expected to have degraded beyond the point where six science instruments can be operated (94.6 W). The new project estimate for reaching the 94.6-W point is late 1985 to mid 1986. If the instrument load were reduced to two instruments, only 90 W would suffice, which level the RTG's are projected to reach by the end of 1987.

The Pioneer 11 RTG prediction is to reach the minimum power for six science instruments in late 1986. (There are still some practical problems which must be solved by the Project in maintaining control of the spacecraft attitude with such a large round-trip light time in the latter part of the mission.)

III. Expected Telecommunications Performance for Pioneer 11 Saturn Encounter

At the closest approach to Saturn, the first week of September 1979, Pioneer 11 will be only 8 deg from the Sun,

heading into conjunction. The desired bit rate by the Project is 1024 b/s, which is the lowest bit rate at which full imaging capability can be achieved. For a description of the imaging instrument and the origin of its data rate requirement, see Ref. 2. Reference 1 had projected that 1024 bits would be marginally possible utilizing the listen-only mode of the new low-noise cones at a system temperature of 14.5 K. Figure 1 shows the updated estimates of Pioneer 10 and 11 downlink performance from the current time through 1983. Using Fig. 1, it can be seen that utilizing the existing 22 K system temperature in the diplex mode capability of the 64-meter stations, only 256 b/s is possible. The 18.5 K system temperature in the diplex mode of the low-noise cones which will be installed at all 64-meter stations prior to Saturn encounter will give a 0.75-dB improvement. From the chart it is seen that 18.5 K system temperature will make 512 b/s possible only near zenith. The listen-only capability of the new cones provides a 14.5 K system temperature, which represents a gain of 1.8 dB over the currently existing 22 K system temperature cones. The 1.8-dB improvement will make 512 b/s possible above about 15-deg elevation. Figure 1 assumes that the spacecraft antenna Earth-pointing is being maintained to within ±0.5 deg, which represents a 0.4-dB loss due to spacecraft antenna-pointing. With more frequent spacecraft precession manuevers to reduce this 0.4-dB loss, it should be possible to achieve the 512 b/s, continuously utilizing the listen-only mode.

The Pioneer 11 spacecraft will require extensive real-time commanding in order to execute its encounter sequence. Utilizing the listen-only mode will therefore require that a 26-meter station be scheduled simultaneously with the 64-meter station in order to handle the uplink. At the time of Saturn encounter, the Voyager and Pioneer view periods have considerable overlap, and Pioneer 10 and the Pioneer Venus Mission will also require continued attention. Therefore, as a practical matter, it will probably be possible to utilize the listen-only mode only for one or two weeks of the 60-day Saturn encounter period. Unfortunately, at the moment it looks like 1024 b/s will not be achievable even with the listen-only mode. At 512 b/s, pictures of 7-deg height instead of 14 deg would be possible at full resolution (7 deg being the look angle from the spacecraft perpendicular to the spin axis). The spacecraft does have a half-resolution mode which would make reduced-resolution 14-deg look angle pictures possible. The effects of the solar conjunction are not accounted for in Fig. 1, and it is expected that because the sunspot cycle was at its peak, significant effects in the telemetry performance would start occurring about 6 deg from the Sun.

IV. The Telecommunications Limit of Pioneer 10

Reference 1 had predicted the telecommunications limit for Pioneer 10 using the existing 64-meter configuration as 24.6 AU, or 28.4 AU if tracking above 30-deg elevation. Figure 2 shows the geocentric range of the Pioneer 10 spacecraft from 1983 through the start of 1990 and contains the revised performance estimates based on in-flight experience since the time of writing Ref. 1. The dB scale on the lefthand edge represents the received carrier power from Pioneer 10 spacecraft for the 64-meter antenna. The sloping curve, labeled 64-meter, 22-deg SNT (system noise temperature) represents the current best estimate of the threshold limit for Pioneer 10 with the existing 64-meter configuration. All the performance numbers on Fig. 1 assume that the spacecraft pointing is maintained within ±0.5 deg, which corresponds to a maximum loss due to spacecraft antenna-pointing of 0.4 dB. One-in-a-thousand deletion rate and the use of the 3-Hz loop in the Block IV receiver are also assumed. The curve for the 64-meter 22-deg SNT case represents the effect of ground antenna elevation. The elevation curve shows that the predicted threshold is 29 AU if tracking is desired as low as 10-deg elevation. Similarly, if tracking is restricted to above 30 deg elevation, the threshold is reached at 34 AU. However, if tracking were limited to above 30-deg elevation, it can be seen that the telecommunications limit is 34 AU, which would not be reached until the first of 1985. Tracking above 30-deg elevation is what has been used in estimating the telecommunications limit for Pioneer 10 for each of the possible performance improvements that will be discussed. The new low-noise cones that will be installed prior to Pioneer 11 Saturn encounter give an 18.5 K system noise temperature in the diplex mode, and from Fig. 1 it is seen that for tracking above 30-deg elevation the telecommunications limit is placed at slightly more than 37 AU, which is not reached until the first part of 1986.

If the listen-only mode were practical for support of Pioneer 10, the resulting 14.5 K system noise temperature would give a capability out to 42 AU, which is not reached until early 1988. Use of the listen-only mode for support of Pioneer 10 for extensive coverage is probably not practical because of the requirement to have a second antenna scheduled for transmitting the uplink in order to command the spacecraft. The 70-meter extension of the 64-meter antenna in the diplex mode with the 18.5-deg cone would give a capability out to almost 41 AU, which would be reached in the first half of 1987. Use of the diplex mode at 14.5 deg at the 70-meter would give coverage capability out to 46 AU, which would be reached in the first part of 1989. Of interest is a 100-meter antenna with 18.5 K system noise temperature (note that the currently discussed large-aperture antenna system of the DSN does not have an S-band capability) which would give a capability with the Pioneer 10 spacecraft design of 58 AU. Pioneer 10 would clearly be out of power but the spacecraft will reach 58 AU sometime in 1993. Figure 2 shows that the orbit of Neptune is at approximately 30 AU and the mean orbit of Pluto at 40 AU. Actually, Pluto is currently

closer to the Earth than Neptune, and its apoapsis range is as far as 49 AU.

Two cautions are in order with regard to estimating the end of the Pioneer 10 mission. The first is that the end of RTG life is only an estimate, and although the RTG performance has been following the updated prediction of its degradation for the past two years, it is possible for the rate of its degradation to change. The second is to notice the tremendous leverage that a small uncertainty in dB has in both range and time for the telecommunications limit. At the area of the currently projected telecommunications limit of 37 AU, 1 dB uncertainty represents more than 4 AU and almost 2 years of time. At this point, ±0.5-dB uncertainty in the performance values shown in Fig. 2 would probably be prudent.

Acknowledgment

Figure 1 was provided by the Network Operations Telemetry Analysis Group.

References

1. Miller, R. B., "Pioneer 10 and 11 Mission Support," in *The Deep Space Network Progress Report 42-33,* pp. 21-25, Jet Propulsion Laboratory, Pasadena, Calif., March-April 1976.

2. Miller, R. B., "Pioneer 10 and 11 Mission Support," in *The Deep Space Network,* Technical Report 32-1526, Vol. XVI, Jet Propulsion Laboratory, Pasadena, Calif., Aug. 15, 1973, pp. 15-21.

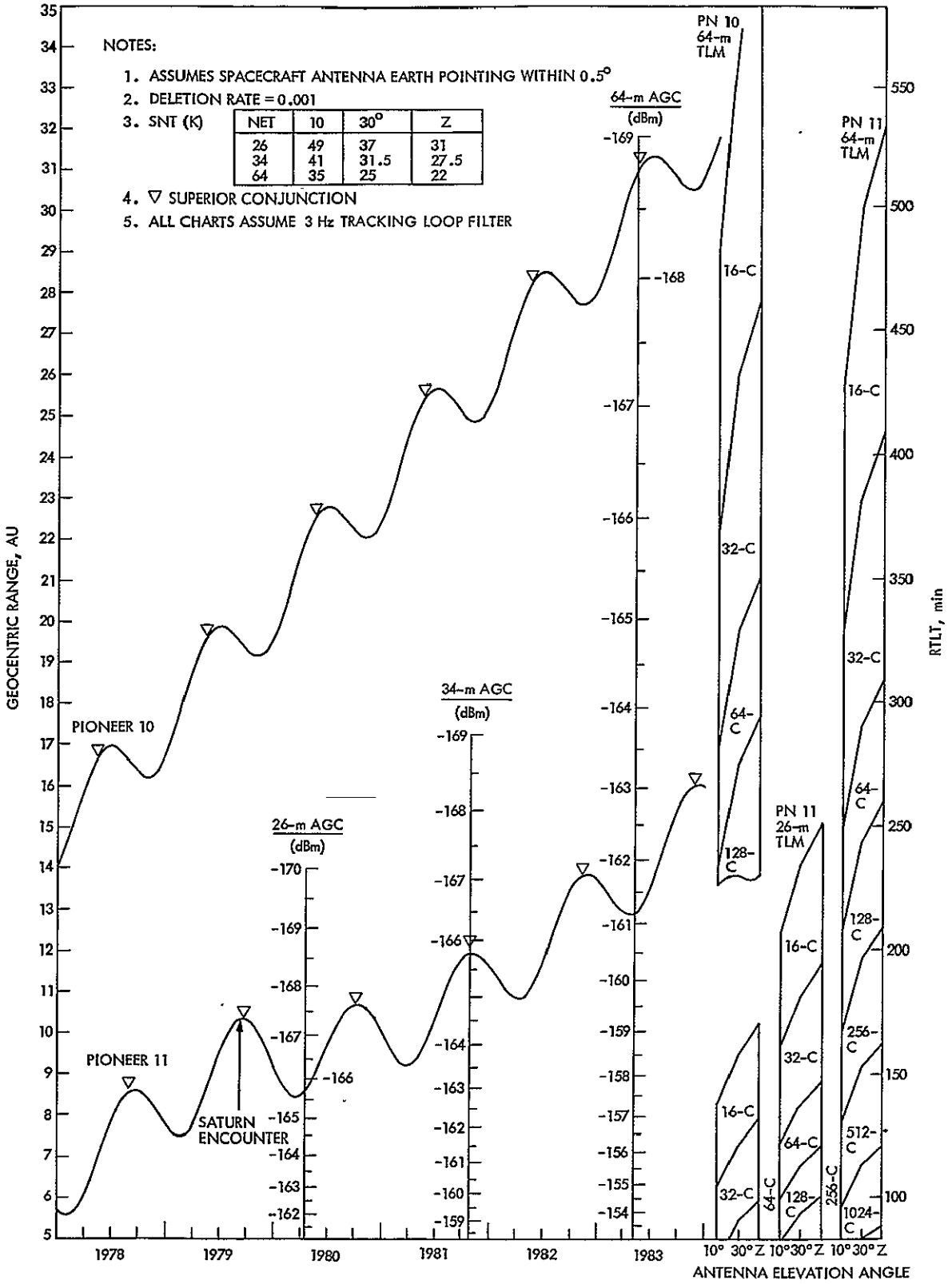

Fig. 1. Downlink performance estimates for Pioneer 10 and 11

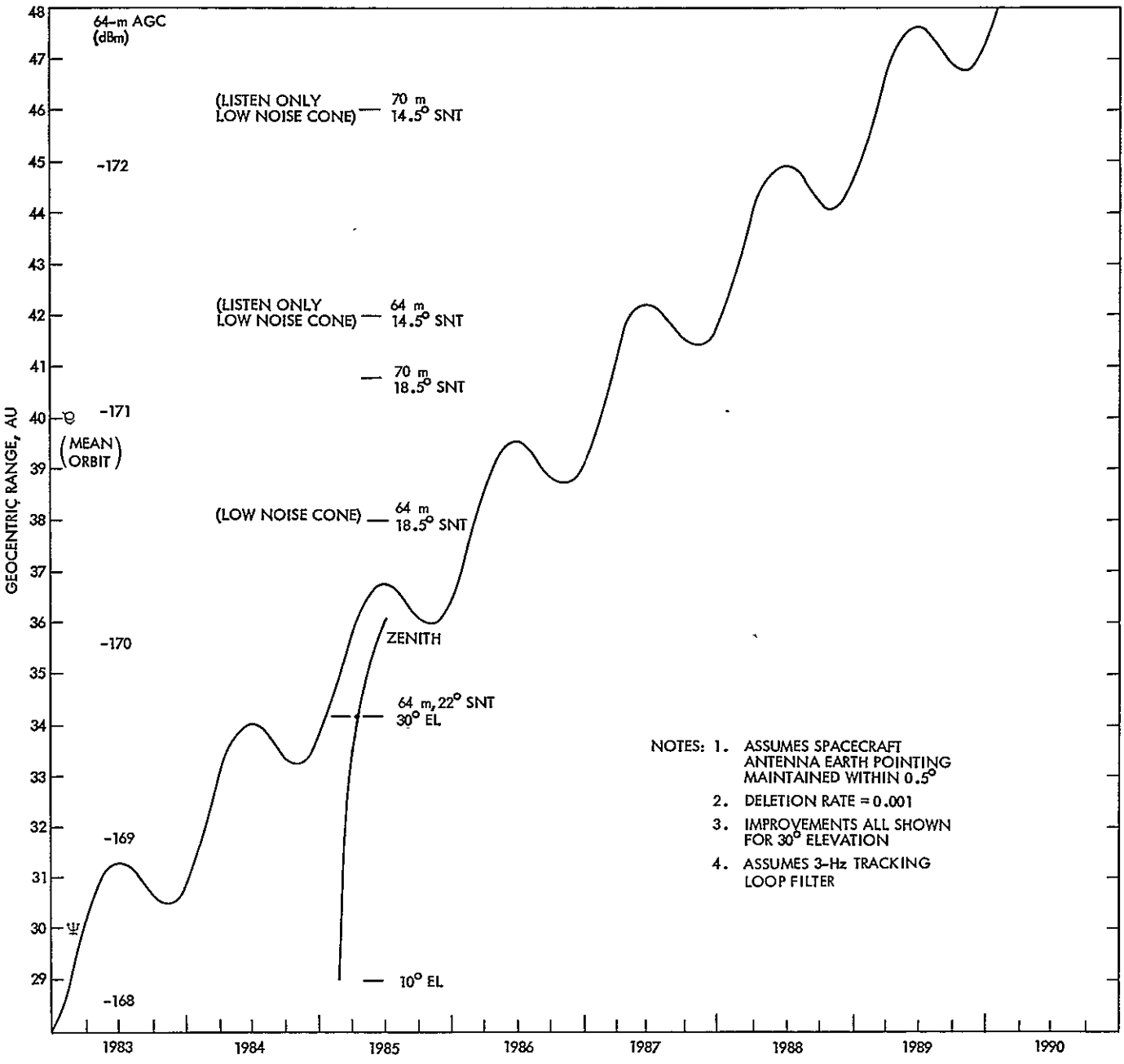

Fig. 2. Downlink performance estimate for Pioneer 10

D5

Helios Mission Support

P. S. Goodwin
TDA Mission Support

W. N. Jensen and G. M. Rockwell
Deep Space Network Operations Section

This article reports on activities of the DSN Network Operations organization in support of the Helios Project from 15 June through 15 August 1978.

I. Introduction

This article is the twenty-third in a continuing series of reports that discuss Deep Space Network support of Helios Mission Operations. Included in this article is information on the Helios 1, 7th aphelion, Helios 2, 5th aphelion, science experiments, 22-bit error polynomial code (EPC) testing, and other mission-related activities.

II. Mission Operations and Status

On 23 July 1978, during a DSS 44 (Honeysuckle Creek, Australia) track, the downlink from Helios 1 was lost at 00:53 Universal Time, Coordinated (UTC). Shortly before that, an unexpected increase of the regulator output power suggested that another switch of the regulator (Ref. 1) had occurred. A spacecraft emergency was declared and 64-m DSS coverage requested from DSS 43 (Canberra, Australia). Helios 1 was acquired by DSS 43 at 03:24:45 UTC. As a result of the regulator switch, the high-gain antenna was off point and had to be commanded back to Earth point before normal operations could resume. Over 600 discrete commands were required to accomplish this pointing. The spacecraft emergency was subsequently lifted at 09:20 UTC. Since all spacecraft systems appeared operational, it was decided to leave Helios 1 in telemetry format 4 (no science data) and to monitor it 2 to 6 h per day, and further, to place the remaining available tracking coverage onto Helios 2 for science data collection.

On 2 August 1978, Helios 1 passed through its 7th aphelion at 08:11 UTC. No station coverage was provided because all experiments were turned off following the regulator switch on 23 July 1978. Five hours after aphelion, DSS 67/68 (Weilheim, Germany) tracked Helios 1 at a bit rate of 32 bits per second (bps) coded, in format 4.

On 2 July 1978, a regulator switch occurred on Helios 2 prior to an acquisition of signal (AOS) over DSS 67/68. As result, the AOS was not successful and at 07:00 UTC a spacecraft emergency was declared and 64-m DSS coverage requested by the Project. At 08:20 UTC, DSS 63 (Madrid, Spain) was released from Pioneer support to acquire Helios 2. DSS 63 had AOS at 10:24:47 UTC with a bit rate of 8 (bps) coded, format 4 (safe mode).

Spacecraft telemetry indicated that several bits had changed. Ground commanding set these status bits back to

normal configuration by 15:15 UTC. The spacecraft experiments were then turned on, and at 22:00 UTC the emergency was lifted.

The Helios 2,5th aphelion occurred on 1 August 1978. The spacecraft was at a bit rate of 32 bps coded with experiments E1, E6, and E8 on and all others off. On 10 August 1978, additional experiments were turned on. Overall coverage of both Helios spacecraft for this period is listed in Table 1.

III. Special Activities

A. Support of On-Board and Ground Experiments

As reported in the last article (Ref. 2), Faraday rotation data were collected over 64-m stations from 9 June 1978 through 28 June 1978. These data are still being collected and analysis has not yet begun. Following this period, we have returned to the 2-h, biweekly 64-m polarimetry-MMA training periods mentioned previously (Ref. 2).

Also, during the period of June through August 1978, a series of solar wind experiment tracks was scheduled. This experiment involves DSS 11, DSS 13, and DSS 14 at Goldstone, California, in addition to DSS 61 and 62 in Spain. The objective of this experiment is to measure the solar wind velocity near the Sun. This period has been designated STIP (Study of Traveling Interplanetary Phenomena) Interval V. The Helios 2 trajectory during this time presented a unique opportunity to study a region of solar wind in which enhanced turbulance existed. Last year, a similar solar wind experiment was conducted and was highly successful (Ref. 3).

B. German Space Operations Center (GSOC) Conversion to the 22-Bit-Error Polynomial Code (EPC) and the Mark III Command System:

On 31 July 1978, the Helios Network Operations Project Engineer (NOPE) conducted a highly successful data flow test between the DSN Compatibility Test Area-21 (CTA-21) at JPL and GSOC, while in the 22-bit EPC. This test verified that 22-bit interface between the DSN and GSOC is functional and that the conversion to flight operation support in October 1978 would go smoothly.

The first attempt to link up the Remote Command Terminal (RCT) at GSOC with the Mission Control and Computing Center (MCCC) Mark III Command System and with the DSN (CTA-21) was accomplished on 3 August 1978. All interfaces were validated and GSOC, via the RCT, was able to send command files to CTA-21's Command Processor Assembly (CPA), control the active/idle state of the Command Modulation Assembly (CMA), and receive transmission confirmation messages.

More tests are scheduled between now and October to further verify and refine interfaces and procedures. During this interval, telemetry, monitor, and Mark III Command System data will be tested. All tests will be conducted using the 22-bit EPC configuration.

References

1. Goodwin, P. S., Jensen, W. N., and Rockwell, G. M., "Helios Mission Support," in *The Deep Space Network Progress Report 42-44*, pp. 50-53, Jet Propulsion Laboratory, Pasadena, Calif., Feb. 15, 1978.

2. Goodwin, P. S., Rockwell, G. M., and Jensen, W. N., "Helios Mission Support," in *The Deep Space Network Progress Report 42-46*, Jet Propulsion Laboratory, Pasadena, Calif., June 15, 1978.

3. Goodwin, P. S., and Rockwell, G. M., "Helios Mission Support," in *The Deep Space Network Progress Report 42-41*, pp. 39-42, Jet Propulsion Laboratory, Pasadena, Calif., Aug. 15, 1977.

Table 1. Helios tracking coverage

Month	Spacecraft	Station type	Number of tracks	Tracking time (h, min)
June	Helios 1	26 meter	50	320:21
		64 meter	0	00:00
	Helios 2	26 meter	0	00:00
		64 meter	36	142:19
July	Helios 1	26 meter	47	269:26
		64 meter	2	6:47
	Helios 2	26 meter	2	14:49
		64 meter	27	120:50

Hydrogen Maser Frequency Standard Computer Model for Automatic Cavity Tuning Servo Simulations

P. D. Potter and C. Finnie
Radio Frequency and Microwave Subsystems Section

A computer model of the JPL hydrogen maser frequency standard has been developed. This model allows frequency stability data to be generated, as a function of various maser parameters, many orders of magnitude faster than these data can be obtained by experimental test. In particular, the maser performance as a function of the various automatic tuning servo parameters may be readily determined.

I. Introduction

Hydrogen maser frequency standards generally display frequency stability characteristics which are strong functions of the observation period over which the stability is measured. As long-term (hours to weeks) stability is of great interest in DSN tracking, testing periods for hydrogen masers are lengthy. In some cases a computer simulation may expeditiously provide performance data which would be impractical to obtain experimentally.

A convenient and widely accepted characterization of frequency stability is the Allan Variance Chart (Ref. 1). Given a frequency standard whose output voltage $V(t)$ may be expressed as

$$V(t) = [V_0 + \epsilon(t)] \sin [2\pi\nu_0 t + \phi(t)] \quad (1)$$

The fractional instantaneous frequency deviation $y(t)$ may be defined as

$$y(t) \equiv \left(\frac{1}{2\pi\nu_0}\right) \frac{d\phi(t)}{dt} \quad (2)$$

The kth average value of $y(t)$, $\bar{y}_k$, over a time interval of length τ is given by

$$\bar{y}_k = \frac{1}{\tau} \int_{t_k}^{t_k+\tau} y(t)\, dt \quad (3)$$

The Allan variance $\sigma_y^2(\tau)$ is defined as

$$\sigma_y^2(\tau) \equiv \left\langle \frac{(\bar{y}_{k+1} - \bar{y}_k)^2}{2} \right\rangle \quad (4)$$

where $\langle\ \rangle$ denotes an infinite time average. In practice $\sigma_y^2(\tau)$ is estimated as

$$\sigma_y^2(\tau) \approx \frac{1}{m} \sum_{k=1}^{m} \frac{(\bar{y}_{k+1} - \bar{y}_k)^2}{2} \quad (5)$$

In this article a hydrogen maser computer model is described which generates the $y(t)$ and $\sigma_y^2(\tau)$ corresponding to the selected values of noise sources and the autotuner (if used) parameters.

II. The Hydrogen Maser Autotuner Servo

The maser cavity autotuner system has been previously described (Refs. 2, 3, 4). The purpose of the autotuner is to electronically bring the cavity resonant frequency f_c into alignment with the atomic hydrogen transition frequency f_n. The effect of cavity pulling on the maser output frequency f_0 is given by (Ref. 2)

$$f_n - f_0 \approx (f_n - f_c)\frac{Q_c}{Q_L} \tag{6}$$

where

Q_c = loaded cavity quality factor ($\approx 3.5 \times 10^4$)

Q_L = atomic hydrogen transition quality factor ($\approx 10^9$)

The basic principle of operation of the autotuner is to periodically change Q_L and to electronically adjust f_c until the change of Q_L does not affect f_0. In this way changes in the maser output frequency f_0 due to mechanical changes in the cavity may be eliminated.

Figure 1 (from Ref. 4) shows the block diagram of the cavity tuning servo system. The atomic quality factor Q_L is varied by an atomic hydrogen beam flux chopper. Variations in the maser output frequency relative to a reference frequency standard are measured by the zero crossing detector and are used to generate a correction voltage on a varactor in the cavity output circuit. The maser fractional frequency deviation $\Delta f/f_0$ is related to the time deviation $\Delta\tau$ in the zero crossing detector by

$$\frac{\Delta f}{f_0} = \left(\frac{\Delta\tau}{\tau_0^2}\right)\left(\frac{1}{f_0}\right) \tag{7}$$

where

τ_0 = nominal beat period = 100 s

f_0 = frequency = 100 MHz

Thus, for example, a beat period change of 0.1 s corresponds to a fractional frequency variation of 10^{-13}.

Figure 2 (from Ref. 4) shows the method used to develop the cavity tuning error signal. In the period τ_1 the up count is during a time of high beam flux, and during the period τ_3 the down count is during a period of low flux. During the τ_5 and τ_7 periods the up-down count has a reversed relationship to the flux level. By subtracting these two up-down counts, a first-order correction is made for frequency shifts which are not caused by the flux level modulation.

Figure 3 (from Ref. 3) is the autotuner servo diagram, where the four-position switches schematically represent the four counting periods shown in Fig. 2. The summing counter is a perfect integrator, resulting in a first-order servo loop with the only adjustable parameter being the loop gain factor K_5. Performance of this servo loop and also possible second-order loop designs are discussed in Sections V and VI below.

III. Hydrogen Maser Computer Model Noise Sources

The computer model operates as a sampled-data system in the same fashion as experimental setups, except the sampling rate is many orders of magnitude greater than with the experimental system, thus allowing for expeditious evaluation of the effects of maser parameters upon the Allan Variance Chart.

Four different types of noise are presently available in the computer model: (1) oscillator shot noise, (2) flicker noise, (3) linear drift and (4) sinusoidally varying drift. Each of these types of noise has a characteristic slope relationship to the averaging period τ on an Allan Variance Chart (Ref. 1). For the oscillator shot noise, the square root of the Allan variance $\sigma(\tau)$ decays as $1/\tau^{1/2}$ and is typically only significant for τ values less than approximately 10^3 s. The theoretical value for this type of noise for the JPL maser is (Ref. 5)

$$\sigma_y(\tau) = \left[\left(\frac{Q_c}{Q_e}\right)\left(\frac{S_0}{2P_sQ_L^2}\right)\left(\frac{1}{\tau}\right)\right]^{1/2} \approx \frac{2.3 \times 10^{-14}}{\tau^{1/2}} \tag{8}$$

where

Q_c = loaded cavity $Q \approx 3.5 \times 10^4$

Q_e = external cavity $Q \approx 9.6 \times 10^4$

Q_L = hydrogen line $Q \approx 10^9$

S_0 = thermal power spectral density $\approx 4.4 \times 10^{-21}$ W/Hz

P_s = cavity power output $\approx 1.5 \times 10^{-12}$W

This type of noise has a flat frequency spectrum and is obtained in the computer model from a pseudorandom number generator.

The flicker noise has no theoretical basis. This type of

noise has a $1/f$ spectral density and results in an Allan variance which is independent of τ. An algorithm for generating this type of noise with a computer has been published (Ref. 6); however, the required computer time for this algorithm is proportional to the square of the number of data points, resulting in unreasonable execution times. The method used in the computer model described here is as follows. A set of 2^M data points is obtained from a pseudorandom number generator and then transformed to the frequency domain by a fast Fourier transform (FFT). The resulting spectral components are multiplied by a $1/f^{1/2}$ factor and inverse-transformed to the time domain. The time required for N data points is approximately proportional to NLOGN for this algorithm. Figure 4 shows an Allan Variance Chart for flicker noise generated by this algorithm; also shown are the 1-sigma error bars for the square root of the Allan variance.

The linear drift noise is characteristic of aging and/or mechanical creep in the maser cavity and has a characeristic slope of unity on the Allan Variance Chart. The sinusoidal noise typically results from diurnal variations in the temperature and barometric pressure environment of the maser. Figure 5 is an Allan Variance Chart of computed performance for typical values of shot noise, flicker noise and diurnal noise.

IV. Autotuner Computer Model

The autotuner is a sampled-data servo loop (Ref. 7) which performs the operations shown in Figs. 2 and 3. For such systems the signal exists only at discrete times, separated by the switching interval τ. The S-plane response of such systems is repetitive at frequencies of $\omega = \pm 2\pi n/\tau$. For purposes of analysis it is convenient to use the Z-transform, defined by

$$Z \equiv \epsilon^{\tau s} = \epsilon^{\alpha\tau} e^{j\omega\tau} \tag{9}$$

Using this transform, the central S-plane strip defined by $-(\pi/\tau) \leqslant \omega \leqslant (\pi/\tau)$, $-\infty \leqslant \alpha \leqslant 0$ is mapped into a unit circle in the Z-plane. The other repetitive strips of the left half of the S-plane are mapped into this same unit circle in the Z-plane.

A general second-order sampled-data servo loop is shown in Fig. 6. A first-order loop such as the existing autotuner is a special case with $K3 = K2 = 0$. Figure 6 is easily implemented in the computer model with each of the "τ" boxes representing a storage register. Figure 7 is a simplified flowchart for the hydrogen maser computer model including the autotuner servo.

V. First-Order Autotuner Loop

For the existing autotuner with a first-order loop, the loop gain is the only servo parameter which is available for optimization. Presently available values for loop gain with the JPL maser nominal 10% line Q modulation (a ratio of 0.9) are approximately 0.001, 0.01 and 0.1; these correspond to autotuner noise gain settings of 0.01, 0.1 and 1 respectively. Figure 8 shows the computer model responses to step inputs of 10^{-12}, for noise gain settings of 0.1 and 1.0. In normal usage the 0.1 setting is used to prevent excessive noise on the varactor as shown in Fig. 8. The response time for this setting is approximately 10 hours, which is too slow for control of diurnal effects.

Figure 9 shows the computer model Allan Variance Chart for a noise gain setting of 1.0 and various flux modulation ratios and illustrates the effect of beam modulation noise. Also shown in Fig. 9 is a set of experimental data, confirming the high noise level associated with the 1.0 gain setting. Figure 10 shows a comparison of computed and measured data for the normally used noise gain setting of 0.1. Figure 11 shows the expected autotuner response for various values of the Q ratio. The improved performance for increased Q modulation is clearly evident. This parameter is fixed by the maser cavity coupling design, however; substantial redesign would be necessary to reduce the Q ratio to 0.4 - 0.6.

VI. Second-Order Autotuner Loop

Using the computer model, a second-order autotuner loop was investigated. With reference to Fig. 6, the closed loop response, $H(Z)$ may be expressed as

$$H(Z) = \frac{K_1(Z - K_3)}{(Z - Z_1)(Z - Z_2)} \tag{10}$$

where

$$Z_1, Z_2 = \frac{1 + K_2 - K_1}{2} \pm j\frac{\sqrt{4(K_2 - K_1K_3) - (1 + K_2 - K_1)^2}}{2} \tag{11}$$

$$\equiv \epsilon^{-\omega_0\tau \cos\alpha} \epsilon^{\pm j\omega_0\tau \sin\alpha}$$

$\cos \alpha$ = loop damping

$\omega_0 \tau \sin \alpha = \omega_n$ = loop natural frequency

With the second-order loop, the natural frequency (bandwidth) and the damping may be independently selected. Figure 12 shows the loop response as a function of damping for a loop natural frequency of 8.7×10^{-5} rad/s (20-h time constant); a damping value of 0.707 ($1/\sqrt{2}$) critical is optimal, a result generally obtained in servo design. Figure 13 shows the performance as a function of loop time constant for the optimal 0.707 critical damping; a time constant value of approximately 20 h appears optimal.

VII. Comparison of Second- and First-Order Loops

Figure 14 shows a comparison of optimal second- and first-order loops, for 10% Q modulation. It is concluded from this study that for the present JPL maser parameter values, the additional complexity of a second-order loop is not warranted.

References

1. Barnes, J. A., et al., "Characterization of Frequency Stability," NBS Technical Note 394, October 1970.
2. Finnie, C., "Frequency Generation and Control: Atomic Hydrogen Maser Frequency Standard," in *The Deep Space Network,* Technical Report 32-1526, Vol. I, Jet Propulsion Laboratory, Pasadena, Calif., pp 73-75.
3. Finnie, C., "Design of Hydrogen Maser Cavity Tuning Servo," in *The Deep Space Network,* Technical Report 32-1526, Vol. II, Jet Propulsion Laboratory, Pasadena, Calif., pp 86-88.
4. Finnie, C., "Tracking and Ground-Based Navigation: Hydrogen Maser Frequency Standard Automatic Cavity Tuning Servo," in *The Deep Space Network,* Technical Report 32-1526, Vol. XIV, Jet Propulsion Laboratory, Pasadena, Calif., pp 56-59.
5. Cutler, L. S., and Searle, C. L., "Some Aspects of the Theory and Measurement of Frequency Fluctuations in Frequency Standards," Proc. IEEE, Vol. 54, No. 2, Feb. 1966, pp 136-154.
6. Barnes, J. A., and Allan, D. W., "A Statistical Model of Flicker Noise," Proc. IEEE, Vol. 54, No. 2, Feb., 1966, pp 176-178.
7. Jury, E. I., *Sampled-Data Control Systems,* John Wiley and Sons, Inc., New York, 1958.

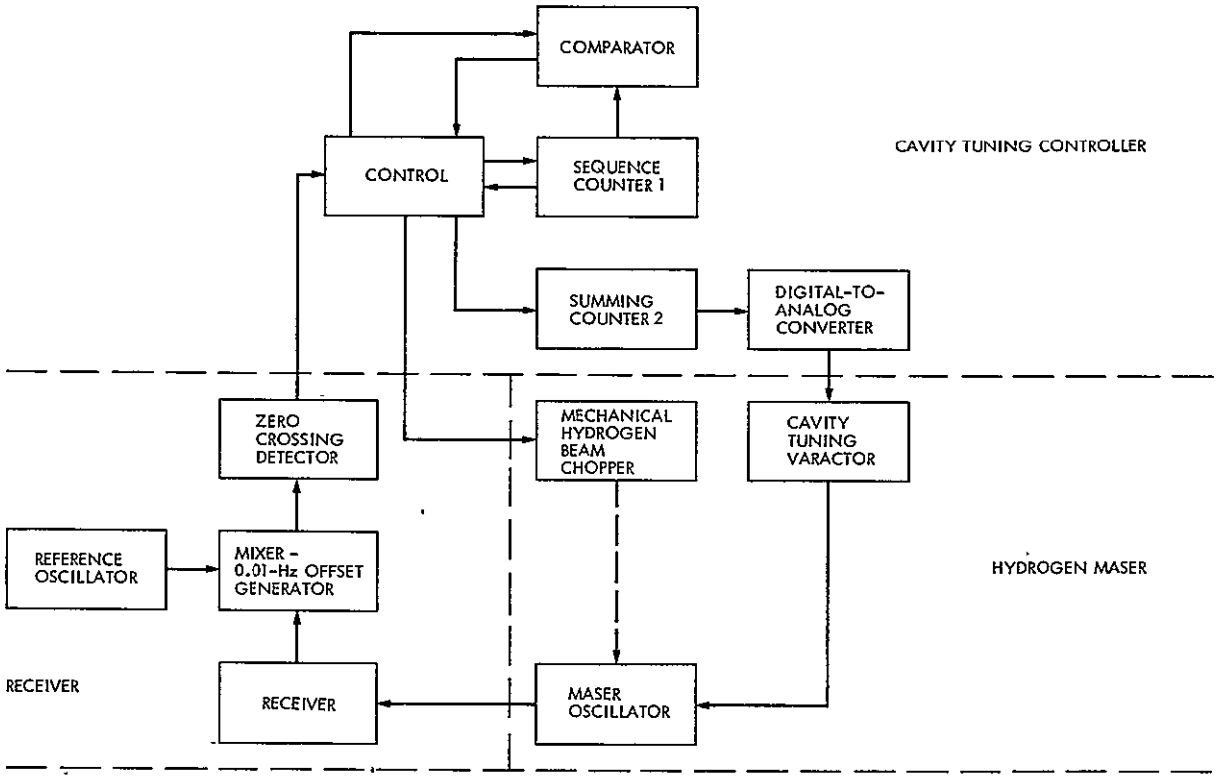

Fig. 1. Cavity tuning servo system block diagram

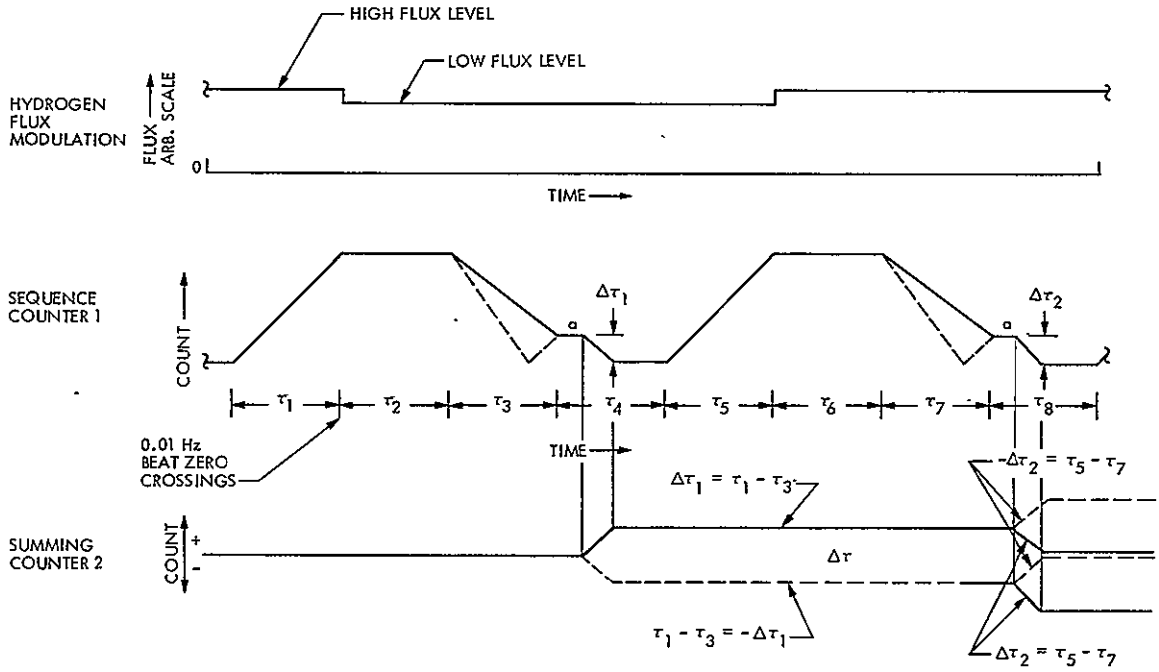

Fig. 2. Tuning mode count sequence diagram

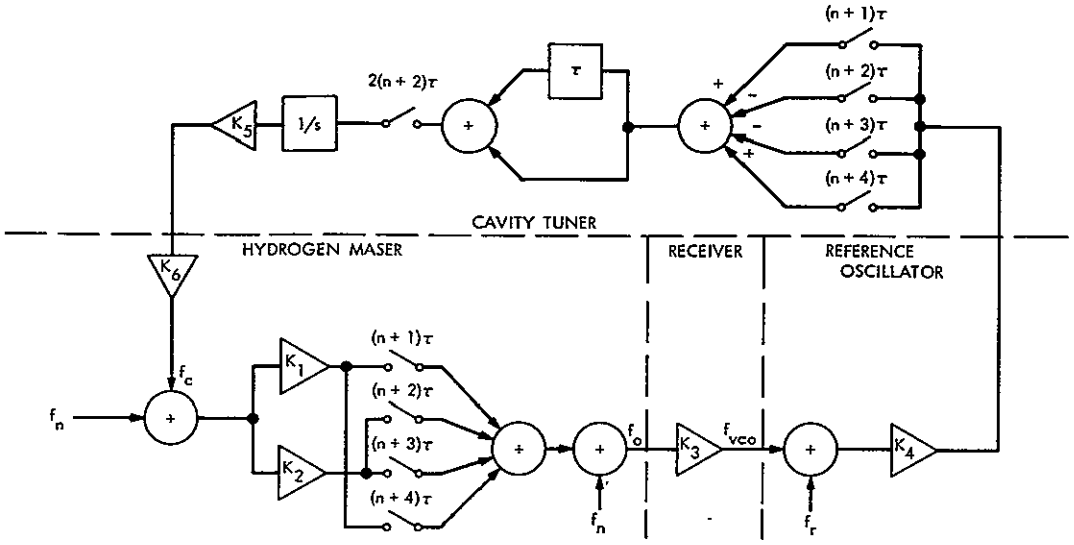

Fig. 3. Cavity tuner servo diagram

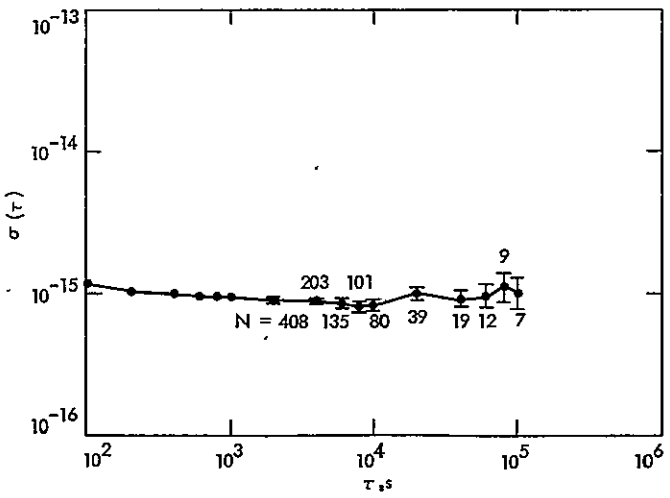

Fig. 4. Flicker noise generator performance

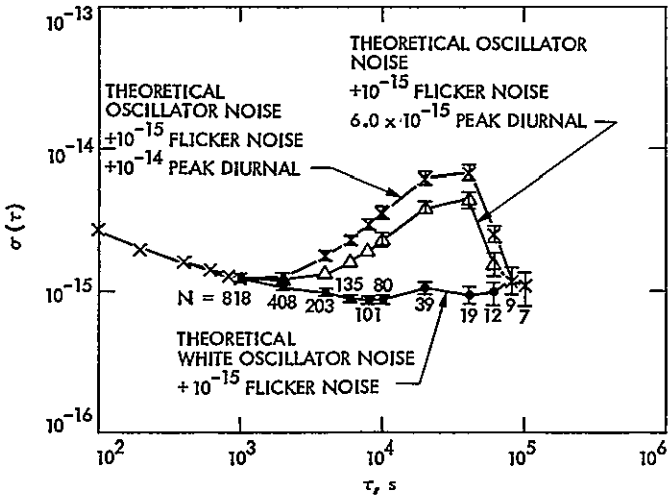

Fig. 5. JPL hydrogen maser computer simulations, no autotuning

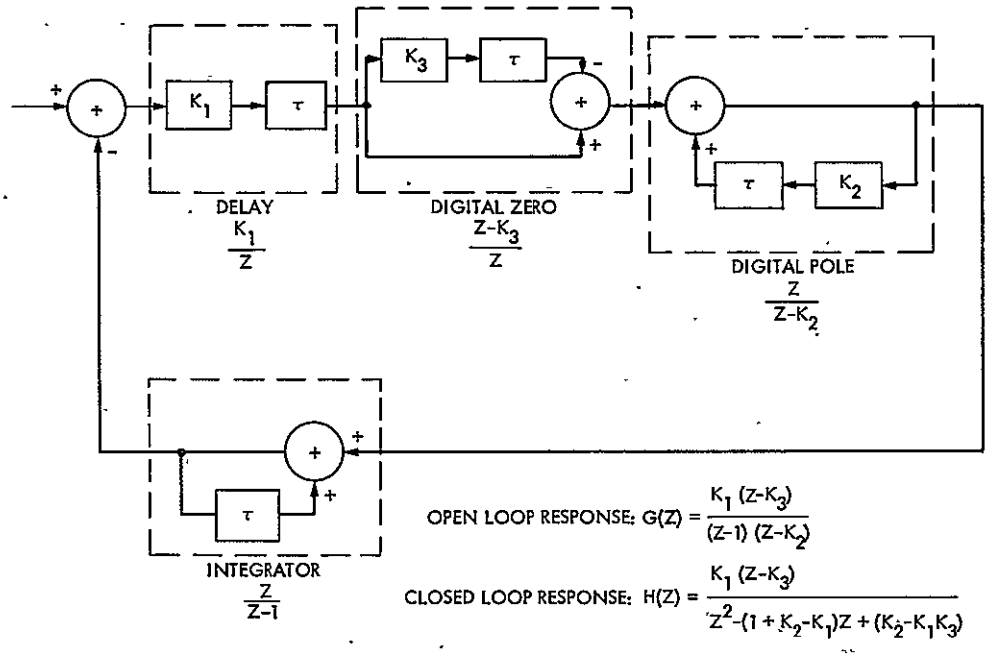

Fig. 6. Second-order sampled data servo loop

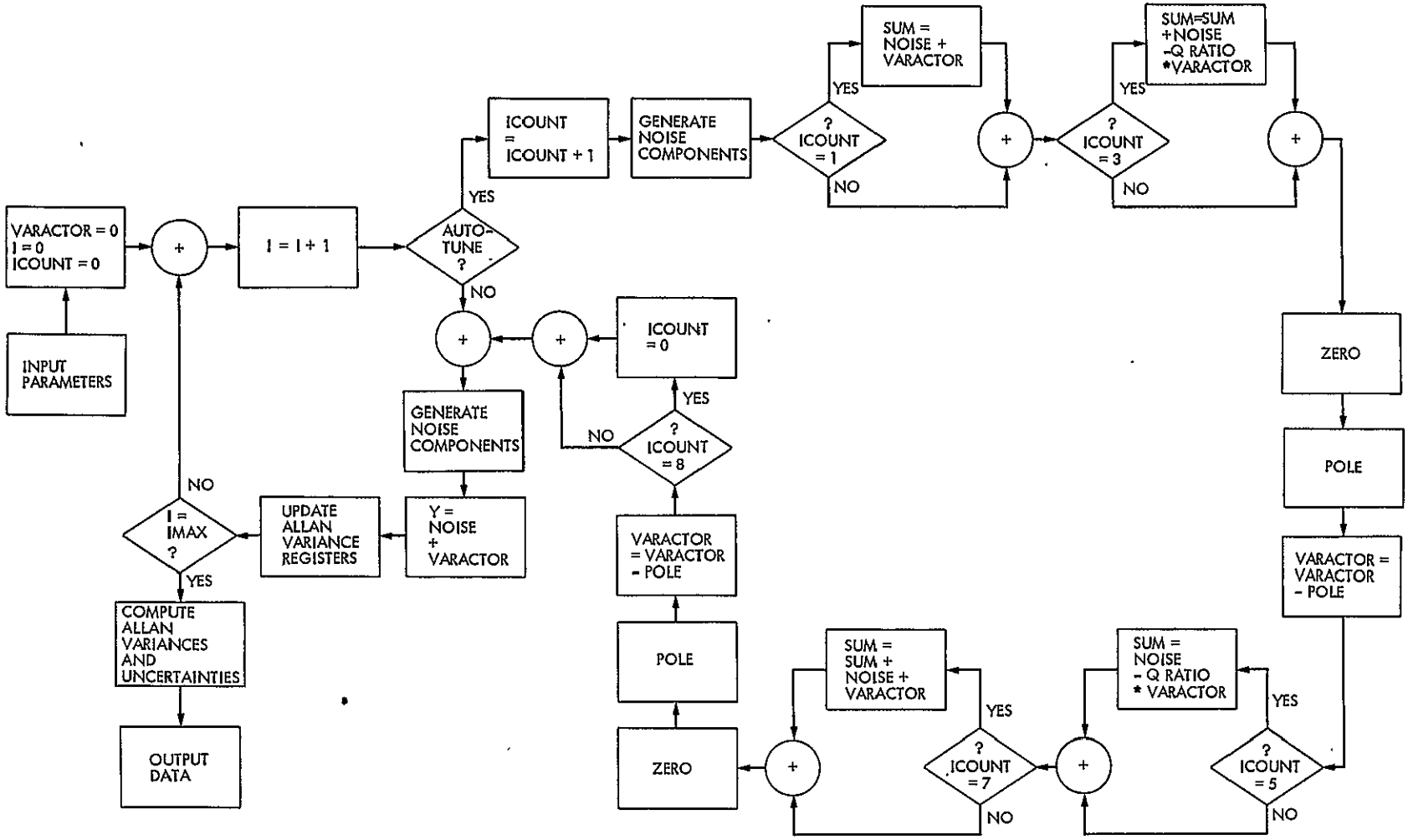

Fig. 7. Simplified hydrogen maser computer model flow chart

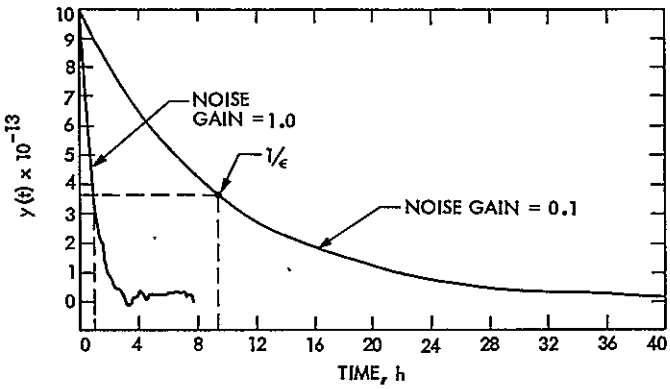

Fig. 8. Computer simulation of autotuner response to a 10^{-12} step input, .90 Q ratio

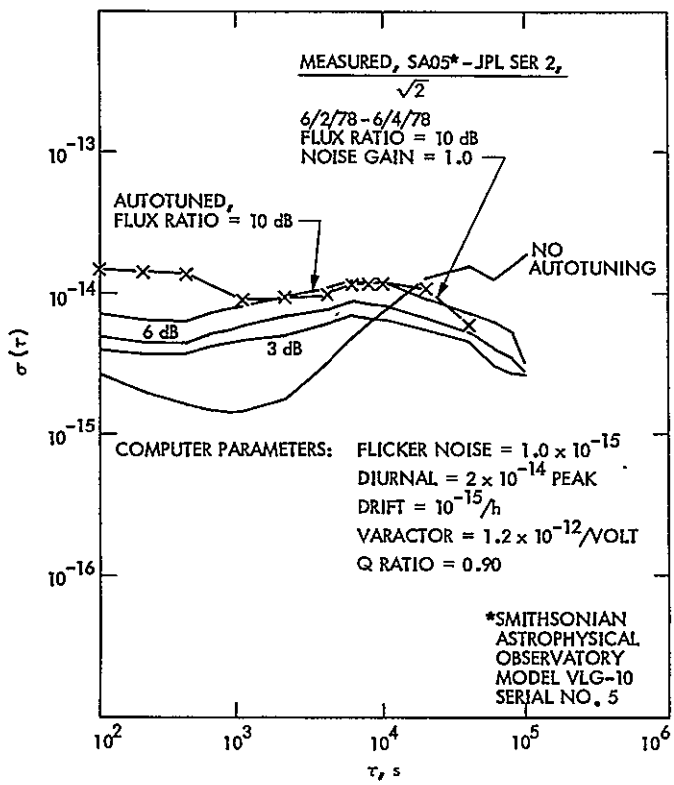

Fig. 9. Computer autotuner simulations, noise gain = 1.0 V/s, Q ratio = 0.90

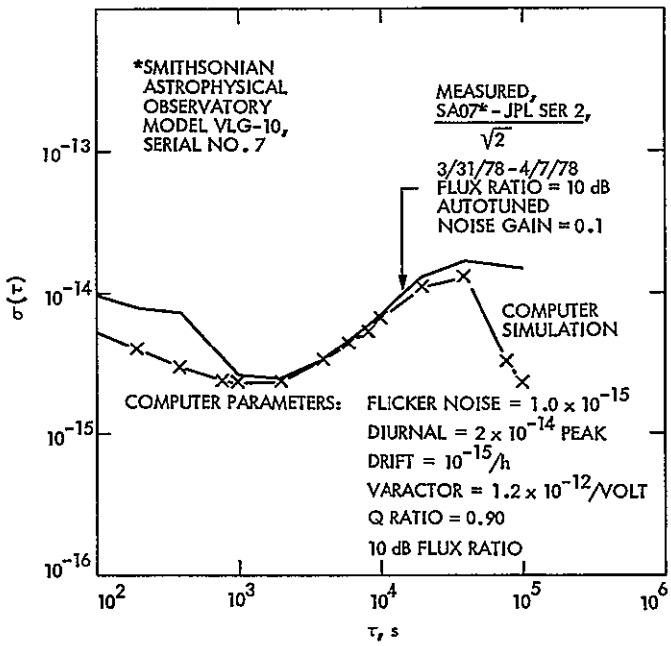

Fig. 10. Computer autotuner simulation, noise gain = 0.1 V/s, Q ratio = 0.90

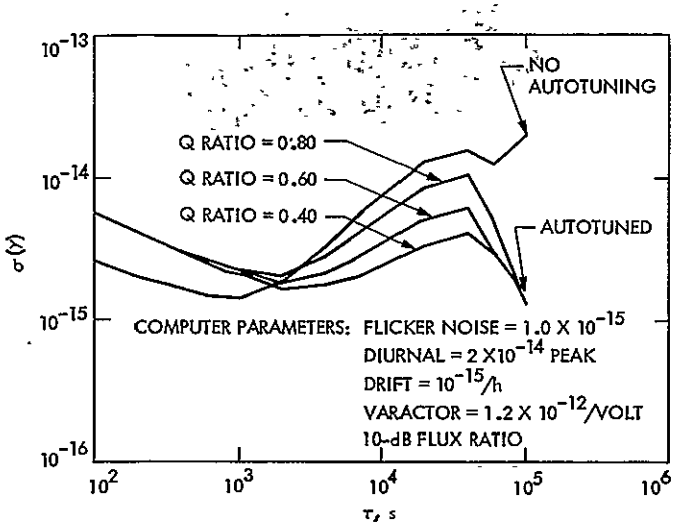

Fig. 11. Computer autotuner simulations, effect of Q ratio

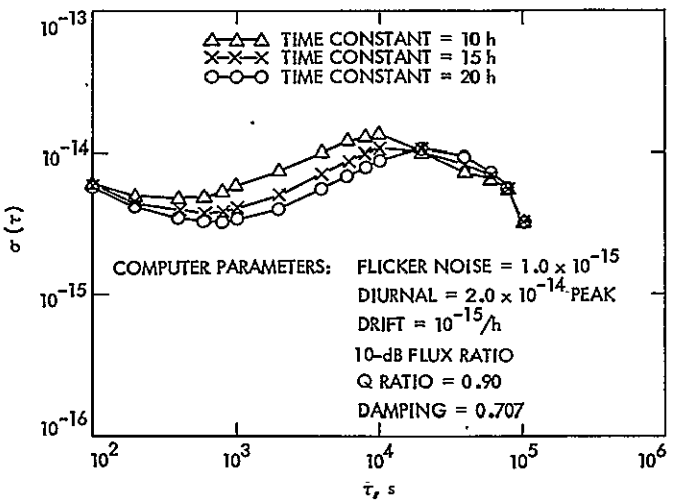

Fig. 13. Second-order autotuner simulations, effect of loop time constant

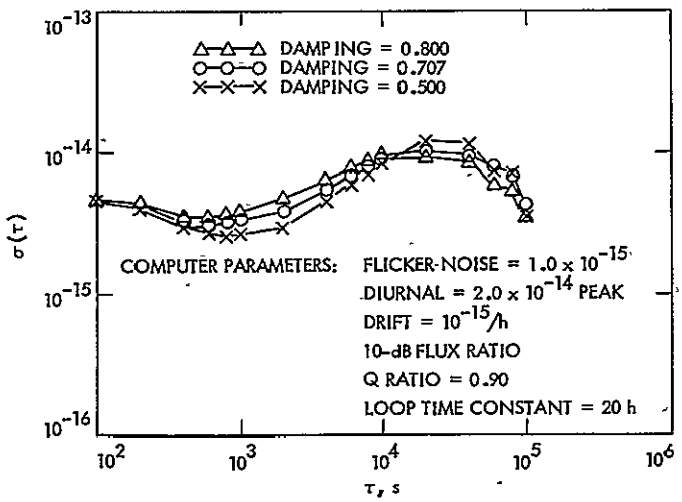

Fig. 12. Second-order autotuner simulations, effect of loop damping

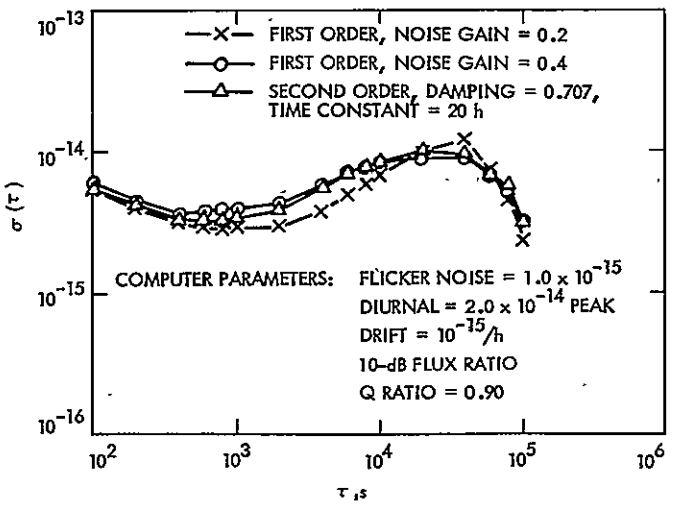

Fig. 14. Comparison of first- and second-order autotuner loops

A Prototype DSN X-S Band Feed: DSS 13 Application Status (Second Report)

W. F. Williams
Radio Frequency and Microwave Subsystems Section

This article, the second in a series discussing a new prototype X-S band horn feed for future use at various DSN sites, deals with the combiner which was designed and fabricated for injecting X- and S-band into the horn. It also discusses predicted performance at DSS 13 by the calculated scattering of the model radiation patterns from the DSS 13 hyperbola.

The results indicate that the present version of the S-band combiner is much too narrow for use in both receiving and transmitting and that the horn patterns, when scattered, yield an improved efficiency over the present horn-hyperbola system.

I. Introduction

The first status report (Ref. 1) of this series discusses the design of a dual-band (X-S) corrugated horn for DSN applications. A half-scale model of the design was fabricated and measured. It fulfilled the requirements of the X-S feed horn program. The radiation patterns and efficiencies of this horn were presented in Ref. 1.

Since this horn is to perform at both X- and S-band simultaneously, a diplexer or X-S combiner must be developed which can inject these signals into the horn. The most important requirement or characteristic of this combiner is that it does not contribute any significant additional loss to the X-band signal. A 0.02-dB X-band loss in this combiner would add 1.4 kelvin to the system noise temperature and this amount is significant in DSN low noise systems. Therefore, it was concluded that the combiner should add less than 0.02 dB to any existing losses in the presently used horn at X-band.

A design technique for satisfying such a difficult requirement was provided by a consultant to JPL (S. B. Cohn, Seymour Cohn Associates, Encino, Calif.). This technique consists of an outer radial waveguide line concentric with the horn and terminating (at the line inner radius) in the horn. The radial line has two circumferential slot chokes to reject any X-band passage. The outer radius of the radial line is excited with the S-band signal, which then passes through and into the X-S feed horn. The theory is discussed in Section II. This technique was used in a full-scale design and the combiner was fabricated. The combiner performed very well at X-band; loss or additional noise from the unit was immeasurably low. However, it suffers from being extremely narrowband in the S-band. The bandwidth (about 50 MHz) is only

sufficient for one function, and in this case the receiving function (2.295 GHz) is chosen. Future additional work will be directed toward increasing the bandwidth to encompass the transmit band also. The final design is discussed in Section III.

A half-scale model of this combiner was fabricated and used with the half-scale model X-S horn (Ref. 1). S-band pattern measurements indicated that the horn was satisfactorily excited through the combiner. X-band was also unaffected.

It then remained to theoretically scatter these measured horn patterns from a computer model of the Venus site (DSS 13) subreflector. This subreflector is a 96-inch (243.84 cm) diameter hyperboloid, whose central region (25.4 cm diameter) is cone shaped, acting as a vertex plate. The hyperboloid is surrounded by a circumferential flange which deflects most of the forward spillover back into the main paraboloid. This flange is about 30.48 cm wide, making the total subreflector 120 inches (304.8 cm) in diameter. A JPL symmetrical scattering computer program was used to calculate the scattering of the horn patterns from the subreflector at selected frequencies in S-band and X-band. This theoretical scattering is discussed in Section IV.

II. The Combiner

The general specifications that were used to define an X-S combiner are as follows:

Frequency

2.1 to 2.3 GHz at S-band (9.09%)
8.4 to 8.55 GHz at X-band (1.77%)

Output Polarization

RCP at S-band
RCP and LCP simultaneous at X-band

Losses

S-band, < 0.2 dB
X-band, < 0.02 dB (relative to horn without combiner)

Power

S-band, 20 kW CW
X-band, receive only

Growth Potential

S-band from 2.1 to 2.4 GHz at 200 kW CW
X-band from 7.1 to 8.55 GHz with 200 kW CW at 7.1 GHz

The technique chosen for this combiner is to feed the S-band into the horn through a circumferential slot that is designed to stop the X-band with a choke or band stop filter. This is illustrated in Fig. 1. The radial line injection region is shown within the horn proper at a position to obtain good impedance matching. The dimension b' is chosen at less than one-half wavelength at the highest X-band frequency. This limits any attempts at X-band propagation within the line to TM^r_{m0} radial modes, where m = number of $\lambda/2$ variations around the circumference, and there are no $\lambda/2$ variations in b' direction. The TE^r_{20} (m=2) radial mode is excited by the X-band HE_{11} wave. Therefore, the radial line band stop filter is designed to stop X-band in the TE^r_{20} radial line mode, and also to present a short circuit looking into the annular opening at X-band. This will result in negligible effect on the X-band HE_{11} wave, i.e., negligible leakage, reflection, or mode conversion.

The S-band signals S_1 and S_2 are fed inward with 180-deg phase difference to yield the horizontal HE_{11} S-band wave in the conical horn, and similarly with S_3 and S_4 for vertical HE_{11} polarization. Waveguide T-hybrids are used, for example, to achieve the equal amplitude, 180-deg power splits and a waveguide 3-dB quadrature coupler to excite these T hybrids. Then one input will yield RCP and the other LCP at S-band.

The design of the X-band choke slots is illustrated in Fig. 2. Dimension b of Fig. 2(a) is chosen at 0.35 in., about 1/4 a guide wavelength in X-band. Using handbook formulas (Ref. 2) the remaining dimensions for the choke are obtained and are indicated in Fig. 2(b). A second choke was added according to the dimensions of 2(c). Beyond these X-band chokes, the radial line continues for a short distance, and is then terminated in four places with step junction transformers. These transformers have four steps and terminate in standard WR430 waveguide.

A photograph of this combiner is shown in Fig. 3. The unit has been separated into two sections for viewing. The section on the right is the input side, showing the taper to a small X-band input end. On the left is the section with the pair of X-band chokes. The addition of four plugs in the second choke was made to improve matching.

III. Combiner Operation

Figure 4 is a block diagram of the laboratory measurement arrangement used to perform the final design development of the combiner. A unit was constructed to the dimensions of the preceding section and used in this measurement to deter-

mine the final required input transformer design and other final details.

Opposite pairs of S-band inputs (① and ②, Fig. 4) must be measured and developed together since they are used together to create a linear polarization (a HE_{11} circular waveguide mode) and there is significant cross-coupling between them. The other terminals (③ and ④) are decoupled from the first pair and used to create the orthogonal linear mode. The two pairs, taken together, will generate circular polarization. These opposite pairs must be excited in phase opposition, i.e., 180 deg out of phase with each other, in order to properly generate this TE_{11} mode instead of the next higher mode, the TM_{01}.

The S-band test generator is therefore fed into an E-H plane tee (180-deg hybrid). This will immediately develop the 180-deg phase difference when using the E-plane input arm. The arm lengths to the combiner inputs must then be equal in order to maintain this 180-deg phase differential. A slotted line is used to perform the measurement on an input arm, and therefore a straight waveguide section of the same phase length is used in the other input arm to maintain this exact phase relationship. In this manner the mutual coupling between opposite arms is "tuned out" as though part of a mismatch reflection.

It was determined by these measurements that an inductive iris was needed at the waveguide inputs to the combiner. This S-band waveguide is only 0.89 cm (0.35 in.) high and the standard 10.92 cm (4.3 in.) wide. This matched input in narrow waveguide was then transformed up to the standard WR430 size using a 5-step, 4-section, waveguide transformer.

Below are tabulated the final voltage standing wave ratios (VSWR) for this combiner.

Frequency, GHz	VSWR
2.100	9.5
2.150	4.5
2.20	2.685
2.225	2.014
2.250	1.501
2.275	1.237
2.300	1.045
2.325	1.195
2.350	1.54
2.375	2.110
2.400	2.940
2.450	6.2
2.5	16.5

The graph of these numbers is shown in Fig. 5. From this it is noted that the bandwidth is only 100 MHz for a VSWR of less than 1.5. This will be suitable for the receive-only operation; however, another solution must be found for future use of the horn for S-band transmission also.

A final and most important characteristic of the combiner is that it must have extremely low loss at X-band, i.e., that it not contribute any more noise to the system than does the existing 22-dB standard being used at 64- and 34-m stations. This noise was measured by using the combiner and a partial full-scale horn; one being fabricated for final use. The X-band first section, horn input was used with the combiner and a second section of the new horn. This was used with the X-band maser for measuring total noise temperature by comparing it with an identical system using the 22-dB standard X-band horn. The standard horn has a certain measurable noise level when looking to the open sky. The new horn, and combiner, are then substituted to determine a different noise level as caused by this different configuration. A long sequence of these substitution measurements was made. The result of all measurements indicated that essentially no difference existed between the two systems. If some small noise was added by the combiner, then it was cancelled by a slightly lower horn loss. This indicates that when this horn-combiner replaces the present horn-reflex plate, the figure of merit will improve by at least a value equivalent to degradation caused by the reflex plate.

IV. Calculated DSS 13 Performance

Figure 6 depicts the subreflector used on the Venus site antenna, DSS 13. This hyperboloid with vertex plate was originally sized and designed for use with the S-band feed horns typical at the DSN. The outer rim or flange is used to capture energy beyond the normal hyperboloid edge and hence reduce forward spillover. The captured energy is then reflected back into the paraboloid at random phases. The result is a very slight degeneration of phase across the main aperture but a large reduction in rear spillover and hence in noise temperature. The vertex plate, which is a simple conical section in the hyperboloid center, scatters energy away from the center of the paraboloid, thus reducing reflection back into the feed horn and also reducing the amount of energy to be finally blocked by the subreflector. This energy also finds its way onto the main parabola at random phases, thus causing a further slight degeneration of the phase pattern across the main aperture face.

JPL has a computer program (Ref. 3) which calculates the scattered or reflected electric field of an incident field from any symmetric reflective surface. The measured radiation patterns of the X-S band model feed horn were scattered

from the Venus site subreflector using this symmetric scattering program. These resulting scattered patterns are used in a JPL efficiency program to determine the final microwave efficiency of the new X-S feed horn at DSS 13.

Figure 7 is typical of the X-band scattering results. This pattern is obtained by assuming that the half-scale pattern at 17.0 GHz is identical to a full scale pattern of 8.5 GHz. Note the very deep nulls in the shadow region caused by the vertex plate of the subreflector. This shadow area is broader than it needs to be for X-band operation. The vertex plate was developed for S-band use, explaining the less than ideal X-band pattern.

It is interesting to compare this scattering with that of the DSN standard X-band horn scattered from the same subreflector. Figure 8 depicts the result. Note that the null central region (±10 deg) is about the same as Fig. 7. The significant difference is in the middle region, from 30 to 45 deg. Here the energy tapers off somewhat (Fig. 8) while in Fig. 7 a more constant illumination is maintained due to the "squareness" of the new horn pattern at X-band. This will result in a higher illumination efficiency for the new horn.

The following is a tabulation of efficiencies for these two cases:

Efficiency	Frequency = 8.5 GHz	
	22 dB Standard	New X-S Dual Band
Forward spillover	0.9707	0.9897
Rear spillover	0.9968	0.9956
Illumination	0.8019	0.8480
Phase	0.8894	0.9005
Blockage	1.0000	1.0000
Cross-polarization	0.9990	0.9990
Total	0.6894	0.7517

The result is an approximate increase in efficiency of 6%, or about 0.38 dB. Nearly 5% of this is from illumination efficiency (more nearly uniform illumination), while the remainder is from forward spillover and phase. The DSN 22-dB standard horn has some sidelobe energy in the form of shoulders on the main lobe while the new X-S horn is completely free of sidelobe energy. These shoulders represent nearly 2% more spillover than occurs with the new horn.

The S-band pattern of the new horn was also scattered from the Venus site subreflector. Figure 9 depicts this scattering for the new horn at S-band. The 4.6-GHz pattern of the half-scale model is used at 2.3 GHz on the subreflector. Figure 10 depicts the 22-dB standard when scattered at 2.295 GHz. The general shapes of these patterns are much alike. This subreflector with vertex plate was designed to fit the pattern of the 22-dB standard at S-band.

Below is a tabulation of these two S-band pattern efficiencies when scattered from the Venus subreflector.

Efficiency	Frequency = 2.295	
	22-dB standard	New X-S band
Forward spillover	0.9707	0.9420
Rear spillover	0.9943	0.9960
Illumination	0.8654	0.8430
Phase	0.9637	0.9120
Blockage	0.9741	0.9690
Cross-polarization	0.9998	0.9998
Total	0.7839	0.6988

The result for S-band has been a drop in efficiency of 8.5% or about 0.5 dB. The most significant difference is in phase efficiency. This is due in part to the S-band displaced phase center from the X-band phase center in the new X-S horn. It is also due in part to the vertex plate and subreflector flange, which were specifically designed for the S-band 22-dB standard horn, and which result in some phase error, as discussed above.

Forward spillover and illumination are also poorer in the new horn at S-band. An investigation of the radiation patterns (Ref. 1) will indicate the reason.

The very slow falloff of energy beyond the −10 dB level contributes to excessive spillover and the "triangular" shaped beam gives more illumination taper and hence a lower illumination efficiency. If the new X-S horn is made larger (larger aperture at the same flare or cone angle) the S-band performance will slowly improve, approaching X-band performance.

Acknowledgement

The author would like to acknowledge the efforts of Dave Nixon, Harry Reilly, and Jim Withington in this program. They have done a major portion of the work of bringing this task to a successful conclusion.

References

1. Williams, W. F., "A Prototype DSN X-S Band Feed: DSS 13 First Application Status," in *The Deep Space Network Progress Report 42-44,* pp 98-103, Jet Propulsion Laboratory, Pasadena, Calif., Apr. 15, 1978.
2. *Radiation Laboratory Waveguide Handbook,* Vol. 10, pp. 337-350, edited by N. Marcuvitz.
3. Rusch, W. V. T., *Scattering of an Arbitrary Spherical Wave by An Arbitrary Surface of Revolution,* Tech. Report 32-979, Vol. 1, Jet Propulsion Laboratory, Pasadena, Calif., pp. 31-39, April 1967.

Addendum

Since this second report was originally prepared, the full-scale X-S horn has been fabricated and its radiation patterns were measured. Some significant differences were noted from the patterns of the half-scale model discussed in this article. At the upper end of the X-band frequency range, the E and H plane patterns of the new horn were noticeably different from each other and not the near overlays as were those of the half-scale model. It is expected that this is due to some additional hybrid mode generation in the horn because of the combiner input slot or because of the change of flare angle in this slot region.

In any event, these full-scale patterns were scattered from the Venus site subreflector in the manner of the above Section IV with the following results:

	Frequency = 8.5 GHz
Efficiency	New X-S dual band
Forward spillover	0.9670
Rear spillover	0.9958
Illumination	0.8410
Phase	0.8980
Blockage	1.0000
Cross-polarization	0.9920
Total	0.7214

We observe about 3% less in efficiency than anticipated from the half-scale model; 2% of this occurs in forward spillover while the remainder is divided among the other factors. This occurs because one plane (E-plane) is broadened in this upper frequency region and results in the additional forward spillover. The expected 0.38 dB improvement, for this particular version of the new horn, is therefore reduced to 0.2 dB improvement. Effects during subsequent development of this horn may regain the full improvement potential.

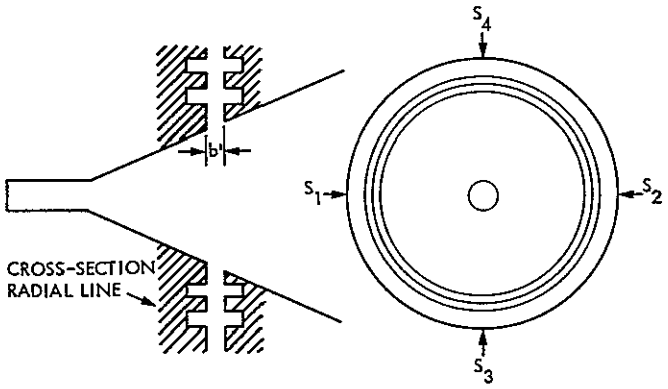

Fig. 1. The combiner concept

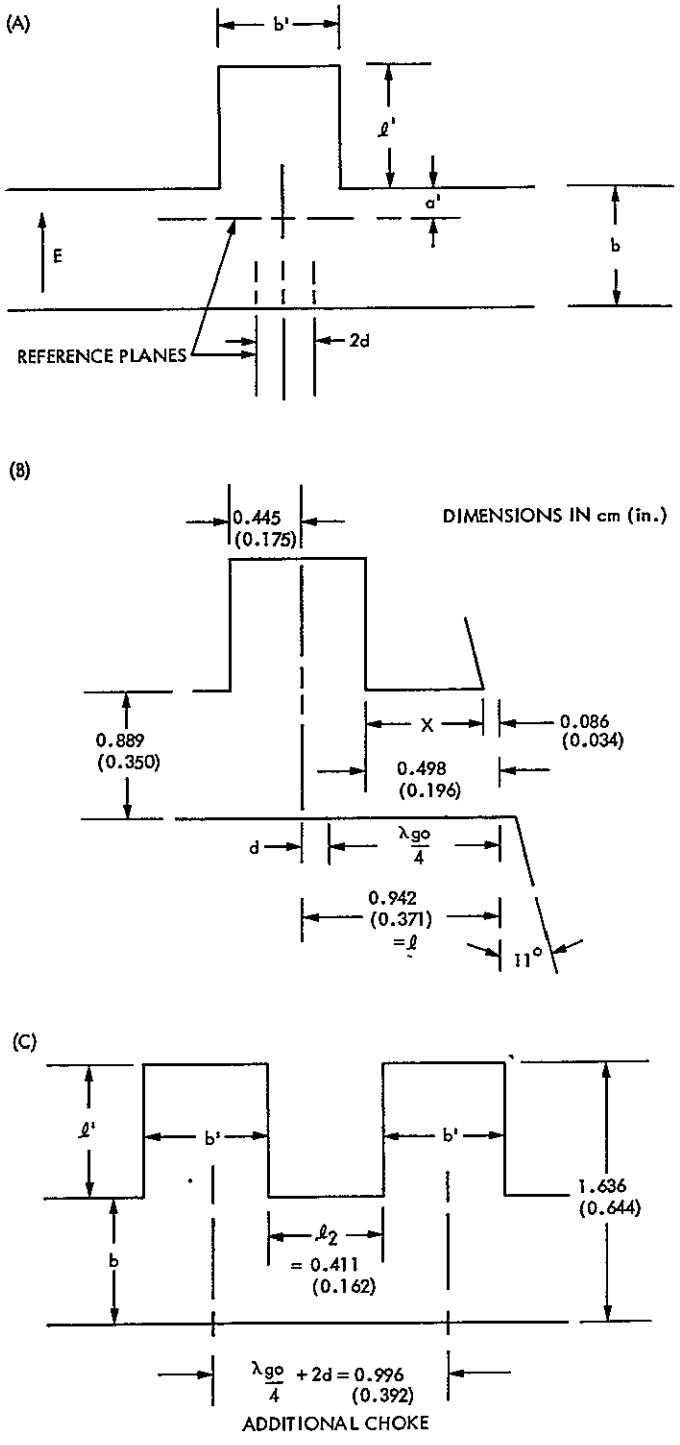

Fig. 2. Choke design

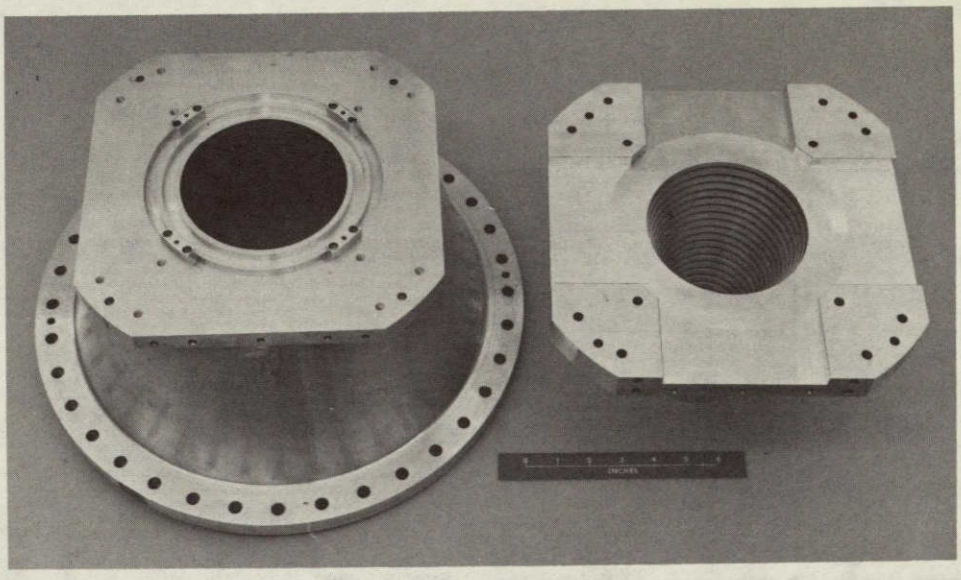

Fig. 3. The combiner

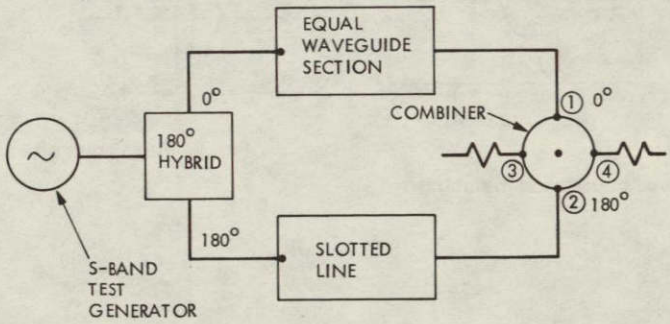

Fig. 4. Laboratory testing setup

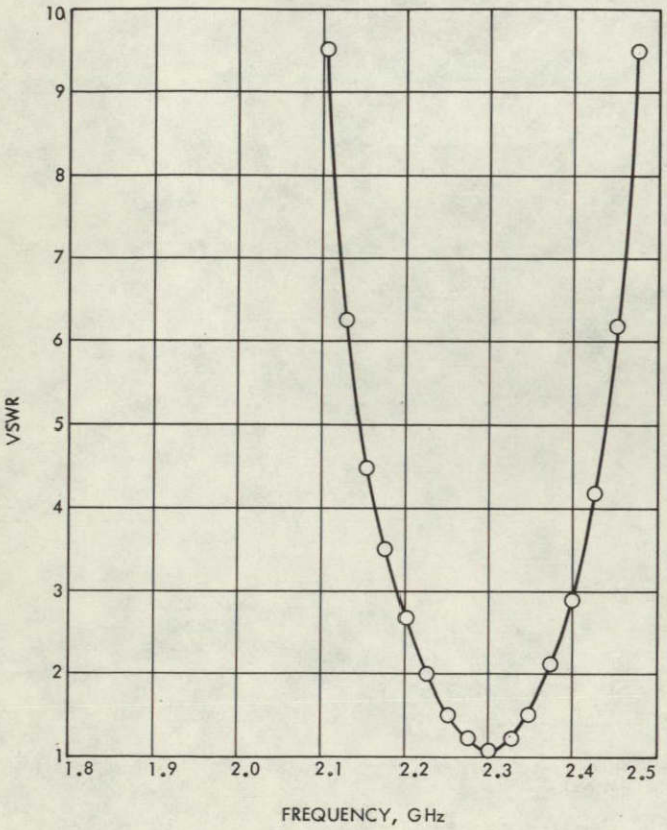

Fig. 5. X-S diplexer S-band slot feed impedance matching

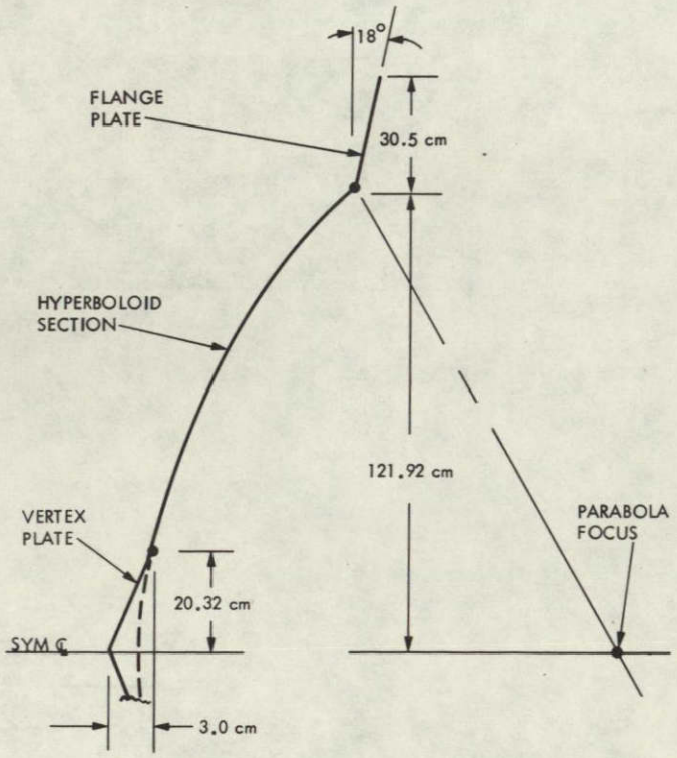

Fig. 6. The Venus site subreflector cross-section

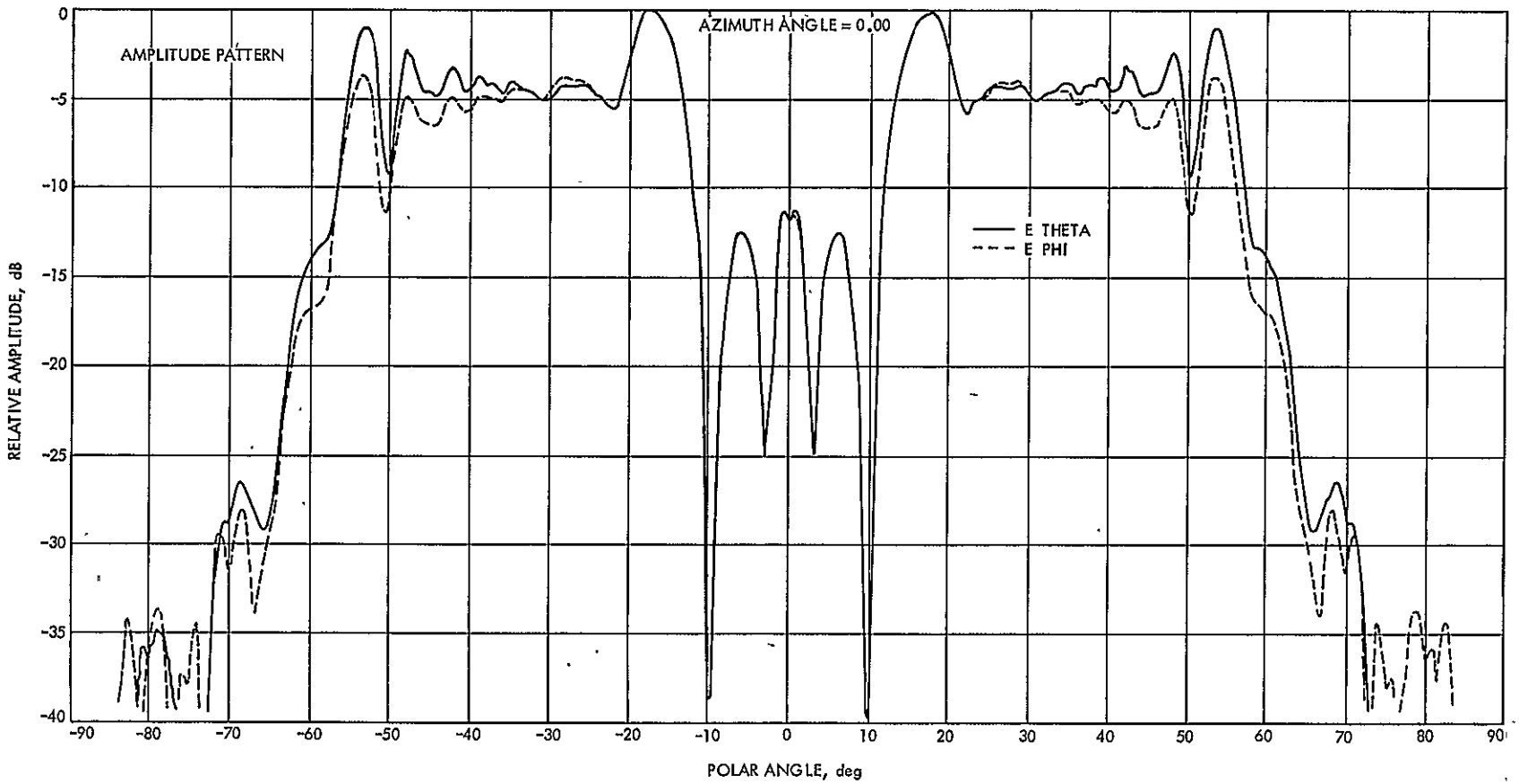

Fig. 7. The 17.1-deg horn at 17.0 (8.5) GHz; Venus site hyperboloid with flange and vertex plate

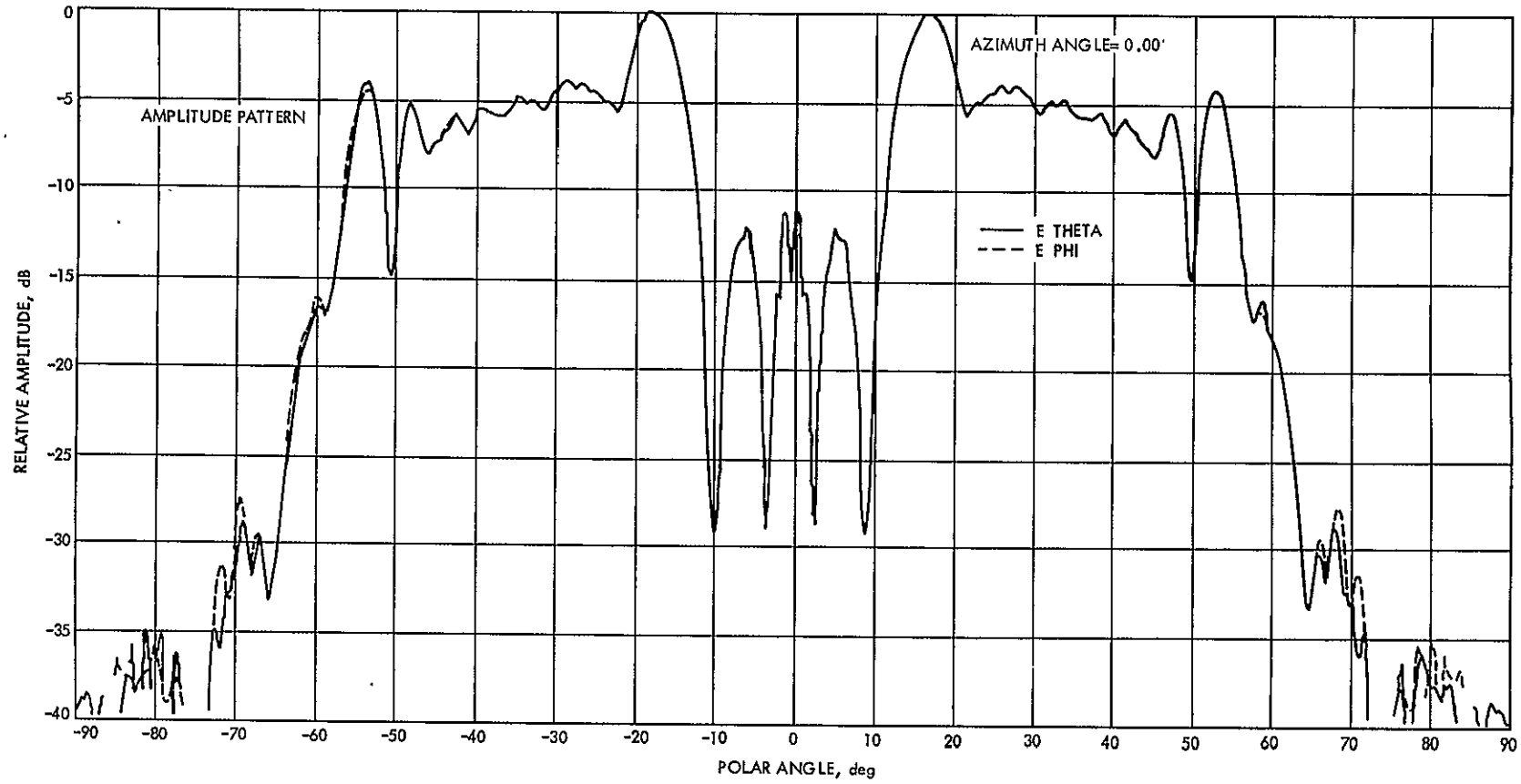

Fig. 8. The 22-dB standard horn at 8.5 GHz; Venus site hyperboloid with flange and vertex plate

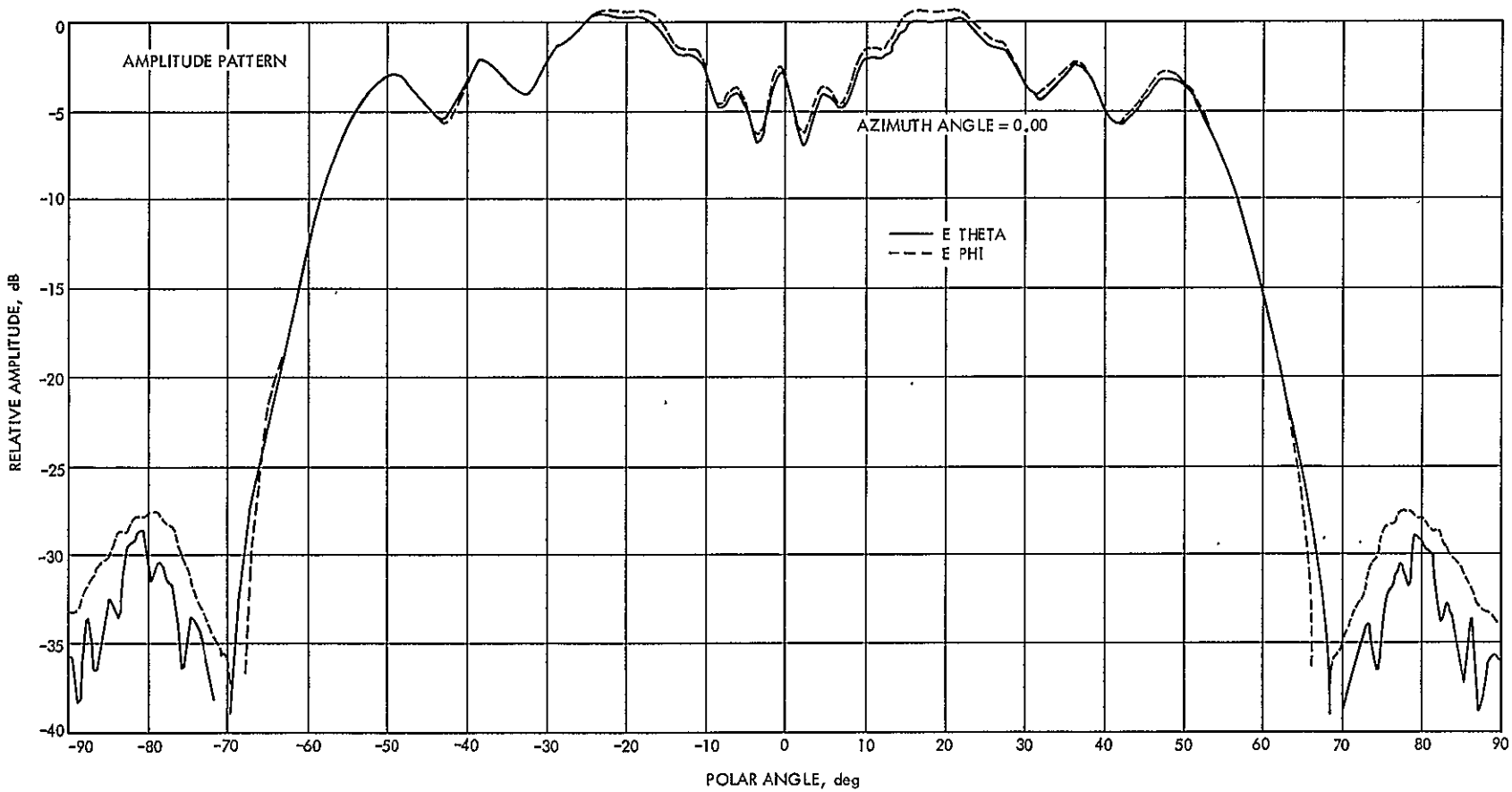

Fig. 9. The 17.1-deg horn at 4.6 (2.3) GHz; Venus site hyperboloid with flange and vertex plate

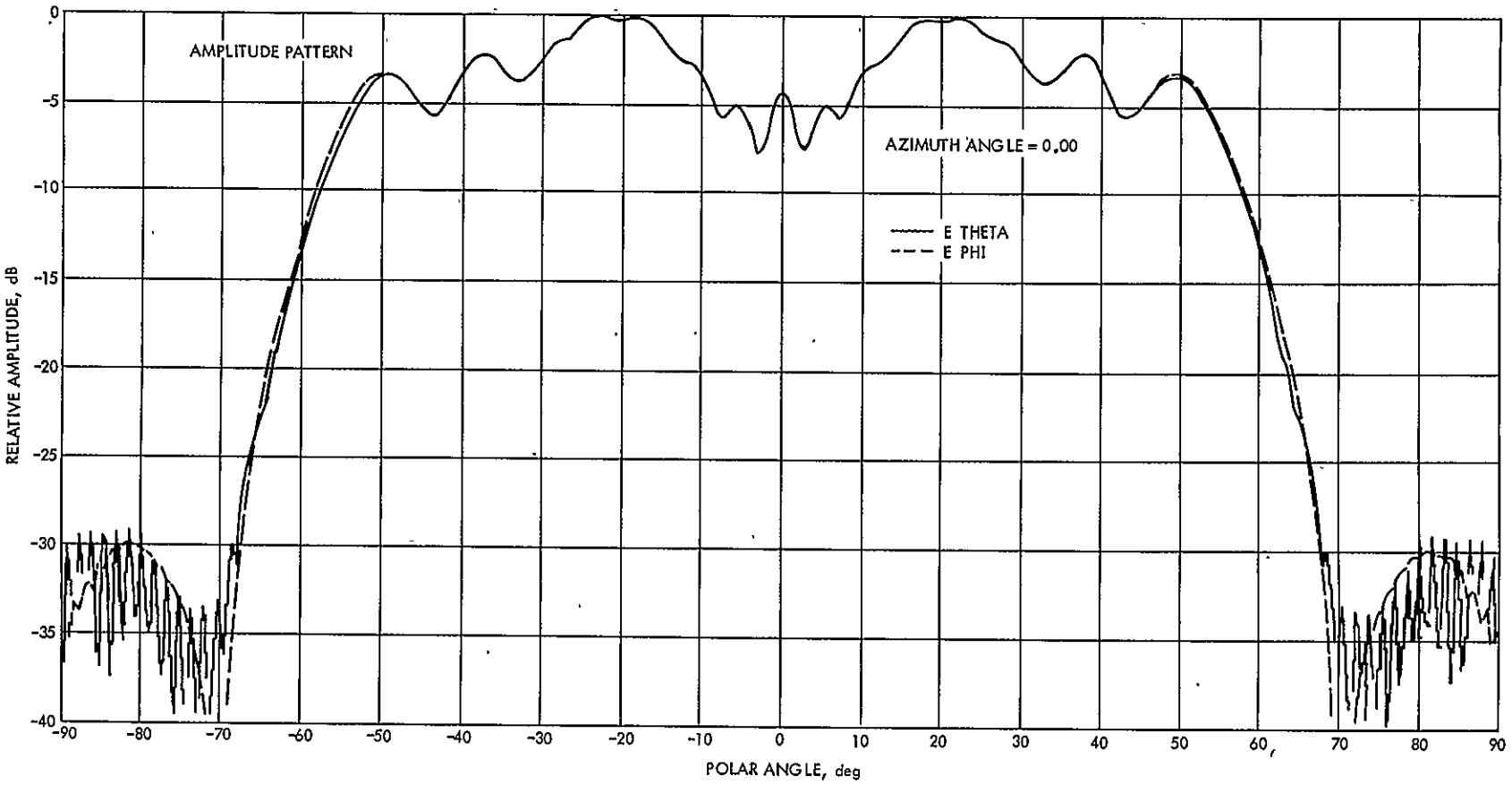

Fig. 10. The 22-dB standard horn at 2.3 GHz; Venus site hyperboloid with flange and vertex plate

An Iterative Algorithm for Decoding Block Codes Transmitted Over a Memoryless Channel

H. Greenberger
Communications Systems Research Section

An algorithm has been developed which optimally decodes a block code for minimum probability of symbol error in an iterative manner. The initial estimate is made by looking at each bit independently and is improved by considering bits related to it through the parity check equations. The dependent bits are considered in order of increasing probability of error. Since the computation proceeds in a systematic way with the bits having the greatest effect being used first, the algorithm approaches the optimum estimate after only a fraction of the parity check equations have been used. This decoding algorithm will be tested via simulations of the (128, 64, 22) BCH code over the deep space channel.

I. Introduction

The measure of performance most commonly used in comparing error-correcting codes for transmitting binary information over noisy channels is the information bit probability of error. When block codes are used, an alternative measure is the code word probability of error. An optimum decoding algorithm which minimizes the probability of error for one measure is not optimum for the other; however, they are very close and become asymptotically equal at very high signal-to-noise ratios.

The optimum algorithm, under either measure, requires an amount of computation proportional to the number of possible code words that can be transmitted, thus limiting the size of the code for which such algorithms can be used. This problem can be bypassed at high signal-to-noise ratios where one can use nonoptimum decoders having simple decoding algorithms and make up the loss by using larger codes with greater minimum distance. At low signal-to-noise, however, there is an absolute limit to the minimum probability of error, depending only upon the decoding algorithm but not upon the code used. In this region, if algebraic decoding is used, the minimum probability of error is greater than what is currently realizable using convolutional coding with an optimum decoding algorithm. The bound for optimum decoding, however, is considerably lower, and worthwhile improvement in performance can be achieved if this limit can be approached. For this reason, approximations to optimum algorithms are being sought whose complexities are very much less but whose performances are close to optimum.

The approximations that can be made are of two types. First, some of the information available at the receiver can be ignored. An example is to decode each bit of the received code word independently, disregarding the dependence between the bits of each code word. This approach is called hard decision

decoding and is equivalent to approximating the channel by a binary symmetric one. Second, an incomplete algorithm can be used. Optimum decoding of block codes is equivalent to calculating the distance, according to some metric, between the received vector and all possible code words and selecting as the best estimate of the transmitted code word that one which is "closest" to it. Examples of incomplete algorithms for block codes are those which search for code words only within a certain distance of the received vector or select, in some other way, a subset of all possible code words among which the best estimate of the full decoding algorithm has a high probability of being found (Refs. 1-3).

II. An Iterative Algorithm

Rather than selecting a set of candidate code words according to some scheme as those mentioned above, an alternate approach is to disregard some of the channel information and make an optimum decision on what remains. This method works well at low signal-to-noise ratios where many bits have a high probability of error and can be disregarded with only a small penalty in performance. Such an algorithm can be put into an iterative form. Starting with an independent estimate of each received bit, the estimate can be improved by successively looking at bits related to it through the parity check equations of the code. These redundant bits are examined in order of increasing probability error. Each bit, as it is examined, improves the estimate of the other bits, the ones with a higher probability of error having a smaller effect than those with a lower probability of error. As poorer and poorer bits are examined, they perturb the previous estimate less and less, and a point is reached where the algorithm may be stopped with a high probability of being close to the optimum estimate.

As each symbol is received, the likelihood ratio

$$\phi_m = \frac{Pr(r_m \mid C_m = 0)}{Pr(r_m \mid C_m = 1)}$$

is calculated and mapped into the region (−1, +1) by the transformation

$$P_m = \frac{1 - \phi_m}{1 + \phi_m}$$

When the entire code word has been received, the symbols are sorted according to increasing probability of error (or equivalently, magnitude of P_m) so that the least reliable bits are to the right. The columns of the parity check matrix of the code are then permuted to the same order as the symbols have been. By using row operations only, the permuted parity check matrix can be reduced to a form which has a triangle of zeros in the upper-right-hand corner. The first P rows of this matrix represent the dependency among the $k+p$ symbols with the least probability of error. If the remaining $n-(k+p)$ symbols are considered erased, then an "optimum" decision, in the sense of minimum probability of symbol error, can be made using only this portion of the matrix. This form of the matrix also leads to an iterative algorithm. Starting with $p=0$ and increasing p by one each iteration, successively poorer received bits are considered in estimating the transmitted symbols, until for $p=n-k$ the "true" optimum estimate is reached.

The decoding rule, for minimum probability of symbol error, using the method of decoding in the dual space of the code, is (see appendix)

$$\Lambda_m = \sum_j \prod_l P_l^{C'_{jl} \oplus \delta_{ml}} \underset{H_0}{\overset{H_1}{\gtrless}} 0$$

C'_{jl} is the lth bit of the jth code word in the dual code, that is, one formed by a linear combination of the rows of the parity check matrix; $\delta_{ml}=1$ if $m=l$ and 0 if $m \neq l$. Thus when estimating the mth bit, the term P_l is included in the product if the lth bit of $C'_j=1$ and $m \neq l$, or the lth bit of $C'_j=0$ and $m=l$.

As an initial estimate of the transmitted symbols ($p=0$), let $\hat{C}_m=1$ if $P_m>0$ and $\hat{C}_m=0$ if $P_m \leqslant 0$. The first iteration uses only a single parity check equation so that there are only two words in the dual code, the all-zero code word and the one equal to the first row of the parity check matrix. The all-zero vector contributes to Λ_m the term P_m, which is the initial estimate, and the single parity check equation contributes a single product term of the P_l's.

The algorithm is then iterated, each time adding another parity check equation and taking into consideration the "best" of the remaining received bits. At each iteration the number of terms in the sum is doubled. Because of the reduced form of the parity check matrix, with zeros in the upper-right-hand corner, the terms Λ_m from previous iterations are not changed when a new row of the matrix is added and the new terms can be added directly to the previous stages' estimate. At each iteration the estimate of each bit is improved and the bit probability of error decreases.

A detailed example of this algorithm will be given for the (23,11) Golay code. The block length of this code is long enough to see the convergence of the algorithm to the optimum solution as the number of iterations increases and yet short enough so that a complete decoding can be done in a reasonable time. In order to estimate the performance of the algorithm at a given SNR, a large number of received vectors was generated and fully decoded. Only the 12 most reliable bits are estimated by the algorithm; the remainder are calculated through the parity check matrix. This forces the estimate of the transmitted vector to be a code word. The estimates of these bits were stored after each iteration, and the code word was considered to be correctly decoded when the 12 bits indicated as most reliable were estimated correctly.

Since the code is linear, the code space looks the same when viewed from any code word. Therefore, in an example, it can be assumed without loss of generality that the all-zero code word is transmitted. The received word can be represented by a vector of dimension 23, $y = (y, y_2, \ldots, y_{23})$. Each element of the vector is of the form $y_i = 1 + n_i$, where n_i is a sample of a zero mean gaussian process of variance $1/2\beta$, where

$$\beta = \sqrt{2 \frac{E_b}{N_0} rate}$$

As a numerical example, consider a received code word which contains four hard errors and therefore cannot be decoded correctly using algebraic decoding. In addition, one of the errors is among the 12 best bits so that the initial estimate of this algorithm would also be in error. A received vector (SNR = 1.0 dB) and the corresponding likelihood ratios are tabulated below

m	1	2	3	4	5	6	7	8	9	10
A_m	.99	1.25	.44	-.63	.52	.25	.01	.97	.36	-.90
Λ_m	.074	.041	.26	3.04	.22	.41	.70	.080	.32	5.62
P_m	.86	.92	.59	-.50	.64	.42	.17	.86	.52	-.70

m	11	12	13	14	15	16	17	18	19
A_m	1.13	.41	.11	.06	1.12	.33	-.74	-.24	.94
Λ_m	.054	.28	.56	.62	.054	.33	3.90	1.24	.083
P_m	.90	.56	.28	.24	.90	.50	-.59	-.11	.85

m	20	21	22	23
A_m	1.86	.71	2.87	1.73
Λ_m	.010	.14	.001	.013
P_m	.98	.75	.99	.97

m = bit number.

A_m = amplitude of mth bit.

Λ_m = likelihood ratio of mth bit.

P_m = transformed likelihood ratio of mth bit.

The first step of the algorithm is to sort the bits according to the absolute values of the transformed likelihood ratios P_m. The sorted order is

Sorted bit order	1	2	3	4	5	6	7	8	9
Original bit order	22	20	23	2	11	15	8	1	19
Sorted P_m	.99	.98	.97	.92	.90	.90	.86	.86	.85

Sorted bit order	10	11	12	13	14	15	16	17
Original bit order	21	10	5	17	3	12	9	16
Sorted P_m	.75	-.70	.64	-.59	.59	.56	.52	.50

Sorted bit order	18	19	20	21	22	23
Original bit order	4	6	13	14	7	18
Sorted P_m	-.50	.42	.28	.24	.17	-.11

The original parity check matrix for this code is

$$\begin{bmatrix}
10100100111110000000000 \\
01010010011111000000000 \\
00101001001111100000000 \\
00010100100111110000000 \\
00001010010011111000000 \\
00000101001001111100000 \\
00000010100100111110000 \\
00000001010010011111000 \\
00000000101001001111100 \\
00000000010100100111110 \\
00000000001010010011111
\end{bmatrix}$$

The columns are permuted to the same order as the received symbols to yield

$$\begin{bmatrix}
0000101000100111001 1000\\
0001100000100010100 1110\\
0000110100010110000 1100\\
0000010000000011111 1100\\
0000010000111000010 1110\\
0000110100001000011 0101\\
0000010010001011010 0011\\
0100000110101000010 1001\\
0100100011001001000 0101\\
1100010011100010000 0001\\
1110100011000000010 1000
\end{bmatrix}$$

Reducing this matrix by row operations to form a triangle of zeros in the upper-right-hand corner yields

$$\begin{bmatrix}
0011101011011000000 0000\\
1111000001110100000 0000\\
0110110110001010000 0000\\
1100100101000111000 0000\\
1000010110010011100 0000\\
1100110100110000010 0000\\
0100010111000001011 0000\\
1000010101001010010 1000\\
1000110000101011000 0100\\
1100000001101001010 0010\\
1100010011100010000 0001
\end{bmatrix}$$

The estimator $\Lambda_m^{(i)} = \sum_j \prod_l P_l^{C'_{jl} \oplus \delta_{ml}}$ (i = iteration number) will be used with this matrix and the sorted P_m's. For the ith iteration the code words C'_j are formed by all linear combinations of the first i rows of the matrix.

The initial estimate can be thought of as using the estimator with a dual code consisting of the all-zero vector alone. The index j, which indicates the jth code word in the dual code, has only the value 1, and C'_{jl} is zero for all values of l. In this case $\Lambda_m^{(0)} = \prod_l P_l^{\delta_{ml}}$ since $\delta_{ml} = 0$ for $m \neq l$ and 1 for $m = l$, $\Lambda_m^{(0)} = P_m$. When the only code word in the dual code is the all-zero one, the code itself contains all possible binary n-tuples. All the bits are independent, and the best estimate of any bit depends only upon the likelihood ratio of that bit itself.

The first iteration begins to use the dependence between the bits as expressed by the first parity check equation (the first row) of the H matrix

$$h_1 = 00111\ 01011\ 01100\ 00000\ 000$$

There are only two code words in the dual code, the all-zero code word and h_1, so that

$$\Lambda_m^{(1)} = P_m + \frac{P_3P_4P_5P_7P_9P_{10}P_{12}P_{13}}{P_m}$$

for m = 3,4,5,7,9,10,12,13

$$= P_m + P_mP_3P_4P_5P_7P_9P_{10}P_{12}P_{13}$$

otherwise.

Note that each term corresponds to a code word in the dual code. Each term contains the product of the transformed likelihood ratios of all the bits in the code word which are equal to one multiplied or divided by the ratio of the mth bit.

The second iteration uses two parity check equations h_1 and h_2.

$$h_2 = 11110\ 00001\ 11010\ 00000\ 000$$

The four code words in the dual code are

$$C'_1 = 0h_2 + 0h_1 = 00000\ 00000\ 00000\ 00000\ 000$$

$$C'_2 = 0h_2 + 1h_1 = 00111\ 01011\ 01100\ 00000\ 000$$

$$C'_3 = 1h_2 + 0h_1 = 11110\ 00001\ 11010\ 00000\ 000$$

$$C'_4 = 1h_2 + 1h_1 = 11001\ 01010\ 10110\ 00000\ 000$$

At this step the purpose of permuting the columns of the H matrix and reducing it to one with all zeros in a triangle in the upper-right-hand corner becomes clear. First, the code words in the dual code at the lth iteration contain all the code words of the $l-1$th iteration so that $\Lambda_m^{(l)} = \Lambda_m^{(l-1)} + 2^{l-1}$ new products. These new products are formed from the code words generated by adding modulo 2, the new parity

check equation h_l, to all the code words of the previous iteration. Second, all the new products include the transformed likelihood ratio of the $(k+l)$th bit but not of bits less reliable than this. Thus the lth iteration uses the previous estimate and the parity check equation containing the best bit not yet used to obtain an improved estimate.

At each iteration the estimate as to which bits are best may change. This is seen in Fig. 1, where the $\Lambda_m^{(l)}$'s are plotted as a function of iteration number. As more parity check equations are used, the absolute value of Λ (which is a measure of goodness) of the bits whose initial estimate was wrong decreases relatively rapidly. At the seventh iteration the best 13 bits are correct and the code word would be decoded correctly if the algorithm would be stopped at this point. At the final iteration, using the full decoding algorithm (equivalent to maximum likelihood), the best 17 bits are correct. Of the four bits whose initial estimate was wrong, only the one with the poorest initial estimate was corrected. In cases where there are few errors or the likelihood ratios of the correct bits are initially higher, the wrong bits are also corrected, but this is not necessary for correct decoding using this algorithm.

The performance of this code as a function of number of iterations is shown in Fig. 2. The zero iteration curve illustrates the performance possible by assuming there are no errors in the best 12 bits, while the 11th iteration curve represents the performance using the full decoding algorithm. Note that at the sixth iteration using $2^6 = 64$ terms in the sum of the estimator, the performance is almost equivalent to the full decoding algorithm which requires $2^{11} = 2048$ terms in the sum.

III. Conclusion

This algorithm is unique among those which approximate maximum likelihood decoders since it is not based upon generating a set of candidate code words. Its performance, in terms of probability of error for a given amount of computation, is comparable to these techniques and may be the basis of more efficient algorithms to be developed in the future.

Appendix

Minimum Probability of Symbol Error Decoding in the Dual Space of the Code (Ref. 4)

The decision rule which minimizes the error probability of the ith symbol is

$$Pr(C_i = 0 \mid \mathrm{y}) \underset{H_1}{\overset{H_0}{\gtrless}} Pr(C_i = 1 \mid \mathrm{y})$$

where the hypotheses are

H_0: The ith symbol of the transmitted code word $C_i = 0$

H_1: The ith symbol of the transmitted code word $C_i = 1$

In terms of the set of possible transmitted code words $\mathrm{C}_m \in C$

$$\sum_{\substack{\mathrm{C}_m \in C \\ C_{mi}=0}} Pr(\mathrm{C}_m \mid \mathrm{y}) \underset{H_1}{\overset{H_0}{\gtrless}} \sum_{\substack{\mathrm{C}_m \in C \\ C_{mi}=1}} Pr(\mathrm{C}_m \mid \mathrm{y})$$

If the code words are equally likely, using Bayes rule yields

$$\sum_{\substack{\mathrm{C}_m \in C \\ C_{mi}=0}} Pr(\mathrm{y} \mid \mathrm{C}_m) \underset{H_1}{\overset{H_0}{\gtrless}} \sum_{\substack{\mathrm{C}_m \in C \\ C_{mi}=1}} Pr(\mathrm{y} \mid \mathrm{C}_m)$$

Both sides of the inequality can be combined so that the sum is over the entire set of code words

$$\sum_{\mathrm{C}_m \in C} Pr(\mathrm{y} \mid \mathrm{C}_m)(-1)^{C_{mi}} \underset{H_1}{\overset{H_0}{\gtrless}} 0$$

This decision rule requires calculating the probability of a given received vector for all words in the code. The estimate of the ith bit is found by summing separately all the probabilities for which the ith bit is equal to 1 and those for which the bit equals 0. The estimate is that value for which the sum is greater. The amount of computation required is proportional to 2^k, the number of words in the code. This decision rule can be transformed to a sum over the code words in the dual codes where the number of calculations required is proportional to 2^{n-k}. This in itself is not of much help when 2^{n-k} is also very large; however, this form of the decision rule can be converted to an approximate decoding algorithm where the sum is over only a small number of code words in the dual code. Such a decoding algorithm is useful if, for a large reduction in the amount of computation, only a small increase in the bit probability of error results, which indeed is the case.

To convert the decision rule to a sum over the dual code, the finite Fourier transform is used. Defining the input points as the elements of V_N, where V_N is the vector space of the 2^N possible binary vectors of dimension N, the Fourier transform of the function $f(\mu)$ defined on these points is

$$F(\mu) = \sum_{\mathrm{v} \in V_N} f(\mathrm{v})(-1)^{\mu \cdot \mathrm{v}}$$

Summing $F(\mu)$ over all $\mu \in C$

$$\sum_{\mu \in C} F(\mu) = \sum_{\mu \in C} \sum_{\mathrm{v} \in V_N} f(\mathrm{v})(-1)^{\mu \cdot \mathrm{v}}$$

Interchanging the order of summation

$$\sum_{\mu \in C} F(\mu) = \sum_{\mathrm{v} \in V_N} f(\mathrm{v}) \sum_{\mu \in C} (-1)^{\mu \cdot \mathrm{v}}$$

Representing the code by a set of basis vectors b_i, which may be the rows of the generator matrix,

$$\mu = a_1 \mathrm{b}_1 + a_2 b_2 + \cdots + a_k \mathrm{b}_k \text{ (where } a \in \{0, 1\})$$

All possible code words are generated as the a_i take on the 2^k possible values so that

$$\sum_{\mu \in C} F(\mu) = \sum_{\mathrm{v} \in V_N} f(\mathrm{v}) \sum_{a_1, a_2 \cdots a_k} (-1)^{(a_1 \mathrm{b}_1 + a_2 \mathrm{b}_2 + \cdots + a_k \mathrm{b}_k) \cdot \mathrm{v}}$$

$$= \sum_{v \in V_N} f(v) \left(\sum_{a_1=0}^{1} (-1)^{a_1 b_1 \cdot v} \right)$$

$$\cdot \left(\sum_{a_2=0}^{1} (-1)^{a_2 b_2 \cdot v} \right) \cdots \left(\sum_{a_k=0}^{1} (-1)^{a_k b_k \cdot v} \right)$$

Any term, and therefore the entire expression equals zero if $vb_i \neq 0$. The only nonzero case is when $v \cdot b_i = 0$ for all i, that is for those v which are in the null space of the code C. These vectors are the elements of the dual code C' and the sum over μ for these vectors is $|C|$ = the number of vectors in C. The sum over C therefore reduces to

$$\sum_{\mu \in C} F(\mu) = |C| \sum_{v \in C'} f(v)$$

For convenience the names of the code and its dual may be interchanged so that

$$\sum_{v \in C} f(v) = \frac{1}{|C'|} \sum_{\mu \in C'} F(\mu)$$

This expression can now be used to simplify the decision rule. Letting

$$f(v) = Pr(y|v)(-1)^{v_i}$$

the decision rule can be written as

$$\sum_{v \in C} f(v) \underset{H_1}{\overset{H_0}{\gtrless}} 0$$

or

$$\sum_{\mu \in C'} F(\mu) \underset{H_1}{\overset{H_0}{\gtrless}} 0$$

$F(\mu)$ may be calculated from the definition of the Fourier transform

$$\sum_{\mu \in C'} \sum_{v \in V_N} Pr(y|v)(-1)^{v_i}(-1)^{\mu \cdot v} \underset{H_1}{\overset{H_0}{\gtrless}} 0$$

The inner sum is over all possible vectors in the space V_N. In the general case this requires a summation over 2^N terms. However, if the channel is memoryless, this can be reduced to only $2N$ terms. In this case,

$$Pr(y|v) = \prod_{j=1}^{N} Pr(y_j|v_j)$$

So that the decision rule becomes

$$\sum_{\mu \in C'} \prod_{j=1}^{N} \sum_{v_j=0}^{1} Pr(y_i|v_j)(-1)^{\mu_j v_i}(-1)^{v_j \delta_{ij}} \underset{H_1}{\overset{H_0}{\gtrless}} 0$$

Note that the term $(-1)^{v_i}$ is included only in the product for $i = j$ by representing it as $(-1)^{v_j \delta_{ij}}$. Expanding the inner sum

$$\sum_{\mu \in C'} \prod_{j=1}^{N} \left[Pr(y_j|v_j = 0) + Pr(y_j|v_j = 1)(-1)^{\mu_j + \delta_{ij}} \right] \underset{H_1}{\overset{H_0}{\gtrless}} 0$$

This expression can be written in terms of the likelihood ratio

$$\phi_j = \frac{Pr(y_j|v_j = 0)}{Pr(y_j|v_j = 1)}$$

by dividing by

$$\prod_{j=1}^{N} Pr(y_j|v_j = 0)$$

The decision rule is then

$$\sum_{\mu \in C'} \prod_{j=1}^{N} \left[1 + \phi_j (-1)^{\mu_j \delta_{ij}} \right] \underset{H_1}{\overset{H_0}{\gtrless}} 0$$

Simplifying even further by dividing by $\prod_{j=1}^{N}(1+\phi_j)$

$$\sum_{\mu \in C'} \prod_{j=1}^{N} \left(\frac{1+\phi_j(-1)^{\mu_j \delta_{ij}}}{1+\phi_j} \right) \underset{H_1}{\overset{H_0}{\gtrless}} 0$$

or in its simplest form

$$\sum_{\mu \in C'} \prod_{j=1}^{N} \left(\frac{1-\phi_j}{1+\phi_j} \right)^{\mu_j \oplus \delta_{ij}} \underset{H_1}{\overset{H_0}{\gtrless}} 0$$

References

1. Chase, David, "A Class of Algorithms for Decoding Block Codes with Channel Measurement Information," *IEEE Trans. Inform. Th.*, Vol. 17-18, Jan. 72, pp. 170-180.

2. Dorsh, B. G., "A Decoding Algorithm for Binary Block Codes and J-ary Output Channels," *IEEE Trans. Inform. Th.*, Vol. 17-20, May 1974, pp. 391-394.

3. Baumert, L. D., and McEliece, R. J., "Performance of Some Codes on a Gaussian Channel," Proc. 1975 International Telemetry Conference, Washington D.C., pp. 189-195.

4. Hartmann, C. P., and Rudolph, L. D., "An Optimum Symbol-By-Symbol Decoding Rule for Linear Codes," *IEEE Trans. Inform. Th.*, Vol. 17-22, Sept. 1976, pp. 514-517.

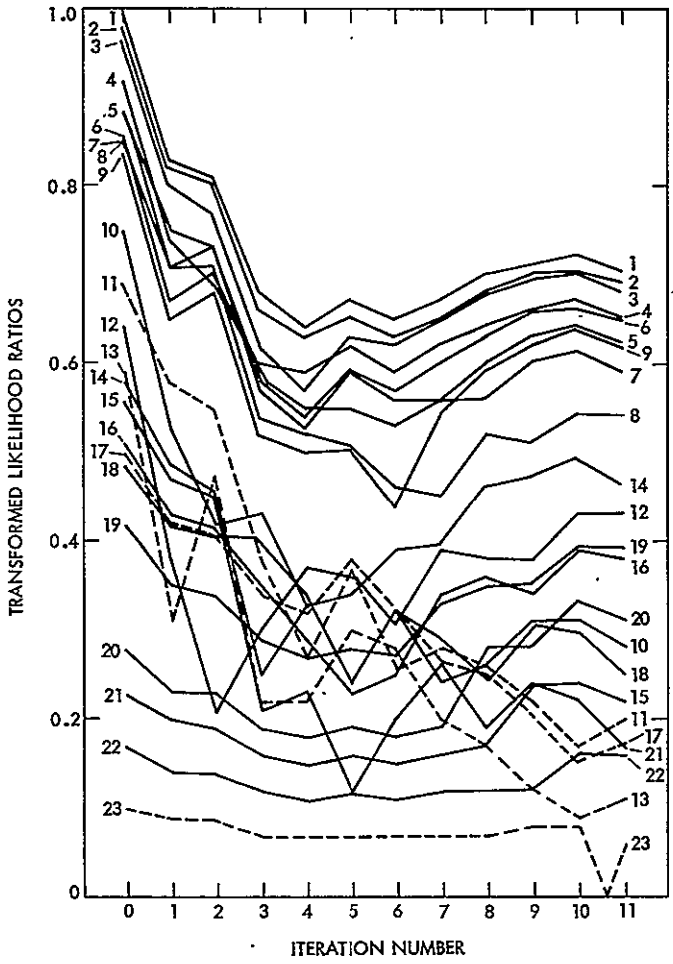

Fig. 1. Improvement of bit estimates as a function of iteration number

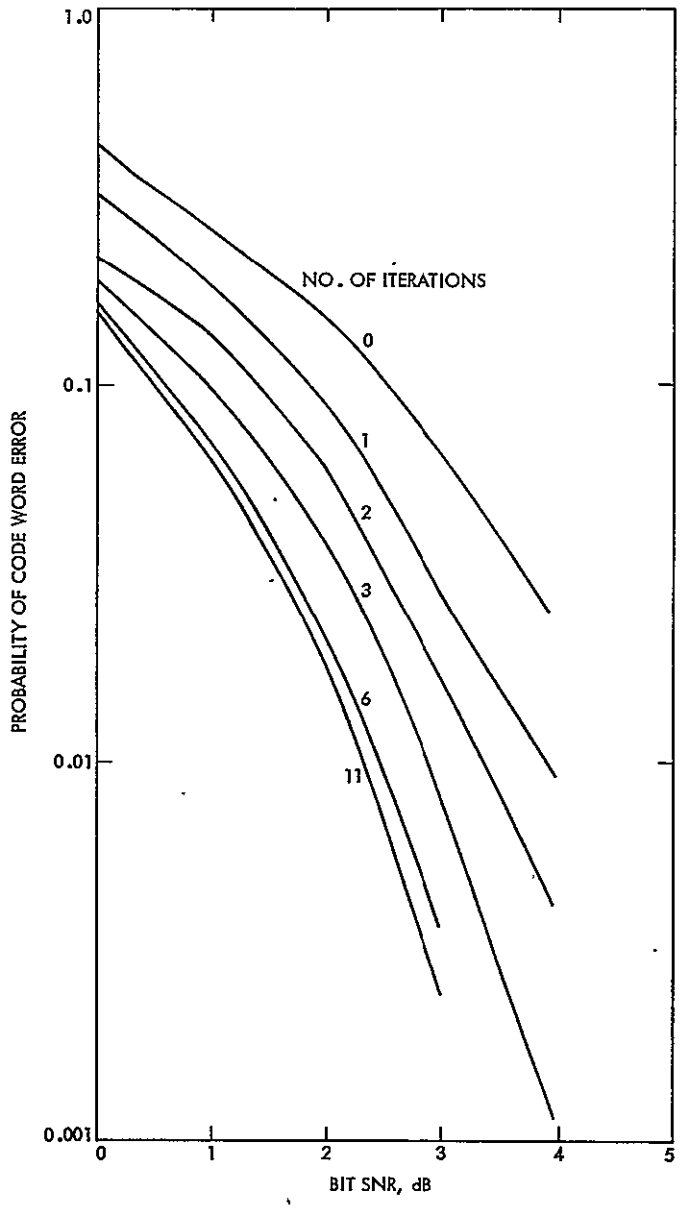

Fig. 2. Performance of the algorithm for the Golay (23.12) code

Soft Decision Decoding of Block Codes

L. D. Baumert and R. J. McEliece
Communications Systems Research Section

The performance of certain block codes on a gaussian channel is evaluated. Two of these codes, the BCH codes of rates 1/2 and 1/3 and length 128, are markedly superior to the constraint length 7 rate 1/2 convolutional code currently used for deep space missions. The algorithm used to derive these results provides a basis for a simple, almost optimum procedure for decoding these codes.

I. Introduction

If one wishes to improve the performance of deep space telemetry beyond the capabilities of short constraint length convolutional codes currently in use, perhaps the most promising approach involves the soft decision decoding of block codes. With this in mind we have employed a general decoding process of Solomon, called "decoding with multipliers" (Ref. 1), to evaluate the performance of certain block codes on a gaussian channel. Two of these codes, the BCH codes of length 128 and rates 1/2 and 1/3, show marked superiority over the constraint length 7 rate 1/2 convolutional code currently in use.

Earlier block code simulations for a gaussian channel are described in Refs. 2-4.

II. Soft Decision Decoding

If a binary quantizer is added to a gaussian channel its capacity is diminished by a factor of $\pi/2(\sim 2$ dB). Thus, optimal code performance on a gaussian channel cannot be achieved by a hard limiting decoding process.

By *soft decision decoding* we mean any decoding process which makes use of the relative magnitudes of the received code symbols. In this article we use a particular soft decision decoding process of Solomon which applies to all linear codes and has the advantage that it does not require the use of a binary decoding algorithm. Thus, it is perfectly general and can be used, for example, to decode the quadratic residue codes.

Suppose a codeword $w = w_1, \ldots, w_n$ from a binary (n,k) linear code is transmitted over a memoryless zero mean gaussian channel. The code symbols are assumed to be ± 1. Thus a received codeword is a sequence of n real numbers, each number representing the integrated value of $w_i + \eta_i$ over one symbol time $-\eta_i$ being the noise. Since the noise is zero mean, the absolute value of these real numbers is a measure of their reliability (the larger the absolute value, the higher the probability that the hard limited version of the real number actually is w_i). In the decoding technique used, the j least probably correct symbols are determined and excluded from consideration. Then k of the remaining $n - j$ symbols are assumed to have proper sign and all codewords (if any) of the code whose signs agree in these k places are constructed. The codewords so

constructed are correlated with the sequence of real numbers from the receiver. Several choices of k of the remaining $n - j$ symbols are made. Among all the codes words thus generated, that one having the maximum correlation value is assumed to have been sent.

III. Simulation Results

The number $Q = (k/n) \cdot d$, where d is the minimum distance of a linear code, is a measure of its asymptotic decoding behavior, since

$$\lim_{\gamma \to \infty} \frac{1}{\gamma} \log P_e = -Q$$

where γ is the bit signal-to-noise ratio and P_e is the bit error probability. Thus, the bigger Q is the better the code should perform, at least for large γ.

As a point of reference our performance graphs show curves for "no coding" and for the maximum likelihood performance of the 7, 1/2 convolutional code being used on NASA's Mariner-class spacecraft (Ref. 5).

A. The (48,24) Quadratic Residue Code

This code is a 5-error-correcting block code with $Q = 6.0$. Two different decodings of this code were simulated. The first of these had $j = 8$, and 130 k-tuples of positions were selected from the remaining $n - j = 40$ positions in such a way that all $\binom{n-j}{4}$ of the 4-tuples were omitted from at least one of these k-tuples. Thus, if there were no more than four hard decision errors among the 40 positions most probably correct, the decoding process would necessarily construct the correct codeword. So, in that instance, the only possible errors would also be made by a maximum likelihood decoder.

The second decoding was done for $j = 16$ with 124 k-tuples such that all 3-tuples from the $n - j = 32$ remaining positions were excluded from at least one of the 124. This performed better, as is shown in Fig. 1. In fact, since about 90% of the errors in this simulation were *identifiably* maximum likelihood errors, it is reasonable to conclude that this decoding is essentially a maximum likelihood decoding of the (48,24) quadratic residue code.

B. The (80,40) Quadratic Residue Code

This code is a 7-error-correcting code with $Q = 8.0$. Five decodings were simulated for this code. The best performance occurred for two different decodings. The first of these had $j = 28$ and 130 k-tuples from the remaining 52 positions such that all $\binom{52}{3}$ triples of positions were omitted from k-tuple. The other used $j = 36$ and 165 k-tuples from the remaining 44 positions such that all pairs of positions were omitted from some k-tuple. Figure 2 shows the performance curve for these two decodings as well as our estimate of the maximum likelihood behavior of the code. This estimate is based on the identifiably maximum likelihood errors which occurred during the simulation.

C. The (128,64) BCH Code

This is a 10-error-correcting block code with $Q = 11.0$. Several different decodings were tried here. We tried k-tuples for $j = 40$, 55 and 56 such that 3, 2 and 2 errors would be allowed among the 88, 73 and 72 remaining most reliable positions. The results were not very good. Note that this kind of selection of the k-tuples really divides the received symbols into two classes: $n - j$ symbols among which k are sought with the correct sign and the other j. Within these classes, all symbols are treated the same – just as if they were equally likely to be in error. This is, of course, not a valid assumption. We tried a further breakdown of the $n - j$ symbols in one decoding as follows: $j = 40$, $n - j = 88$ and these 88 symbols were ordered by magnitude to establish their relative error probability. The 16 most likely correct were assumed to be correct; two errors were allowed among the next 40 most likely correct positions and four errors were allowed among the remaining 32. This performed better than the simpler collections of k-tuples mentioned above.

The improved performance in this last decoding suggested that we might try to match the finer gradations of error probability among the symbols a little more closely. We did this by gathering (at 1.5 dB's) the error frequencies of the least likely correct, . . . , most likely correct symbols. Then we constructed k-tuples by a random placing of 1's approximately in accordance with the entropy of these error frequencies. This collection of k-tuples performed much better than the previous collections, and when 1500 of them were used, the identifiably maximum likelihood errors predominated; so much so that it is reasonable to assume that the performance achieved (Fig. 3) is within 0.1 dB of maximum likelihood behavior.

As a by-product of this simulation we also determined that the number of minimum weight (=22) codewords of this code is almost certainly 243,840 (see Ref. 6 for details of this determination).

D. The (128,43) BCH Code

This is a 15-error-correcting code with $Q = 10.75$. It was decoded using 1500 k-tuples selected to fit the observed error statistics at 1.5 dB, as described in more detail above for the (128,64) code. Within the accuracy of this simulation the performance of this code (Fig. 4) is the same as the (128,64) code and seems also to be within 0.1 dB of its maximum likelihood behavior.

Much of the analysis of Ref. 6 applies to this code also, and using it we can conclude that the number of minimum weight (=32) codewords of this code is almost certainly 124,460.

References

1. Baumert, L. D., McEliece, R. J., and Solomon, G., "Decoding with Multipliers," in *The Deep Space Network Progress Report 42-34*, Jet Propulsion Laboratory, Pasadena, Calif., Aug. 1976, pp. 43-46.

2. Chase, D., "A Class of Algorithms for Decoding Block Codes with Channel Measurement Information," *IEEE Trans. Inform. Th.*, IT-18 (1972), pp. 170-182.

3. Baumert, L. D., and McEliece, R. J., "Performance of Some Block Codes on a Gaussian Channel," Proc. 1975, International Telemetry Conference, Washington, D.C., pp. 189-195.

4. Chase, D., and Goldfein, H. D., "Long Block Codes Can Offer Good Performance," Information Theory International Symposium, Cornell University, October 1977.

5. Webster, L., "Maximum Likelihood Convolutional Decoding (MCD) Performance Due to System Losses," in *The Deep Space Network Progress Report 42-34*, Jet Propulsion Laboratory, Pasadena, Calif., Aug. 1976, pp. 108-118.

6. Baumert, L. D., and Welch, L. R., "Minimum Weight Codewords in the (128,64) BCH Code," in *The Deep Space Network Progress Report 42-42*, Jet Propulsion Laboratory, Pasadena, Calif., Dec. 1977, pp. 92-94.

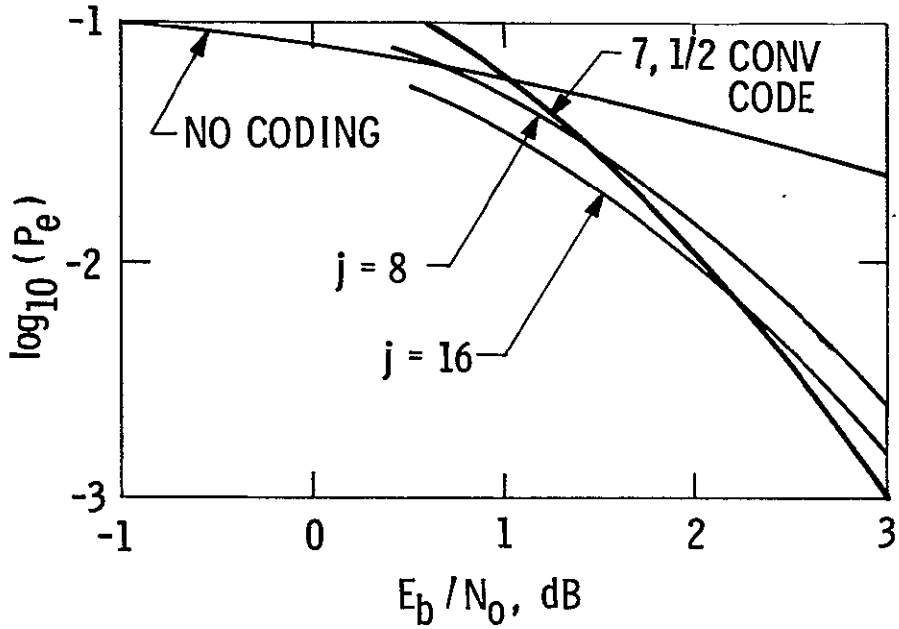

Fig. 1. (48,24) QR, Q = 6.0

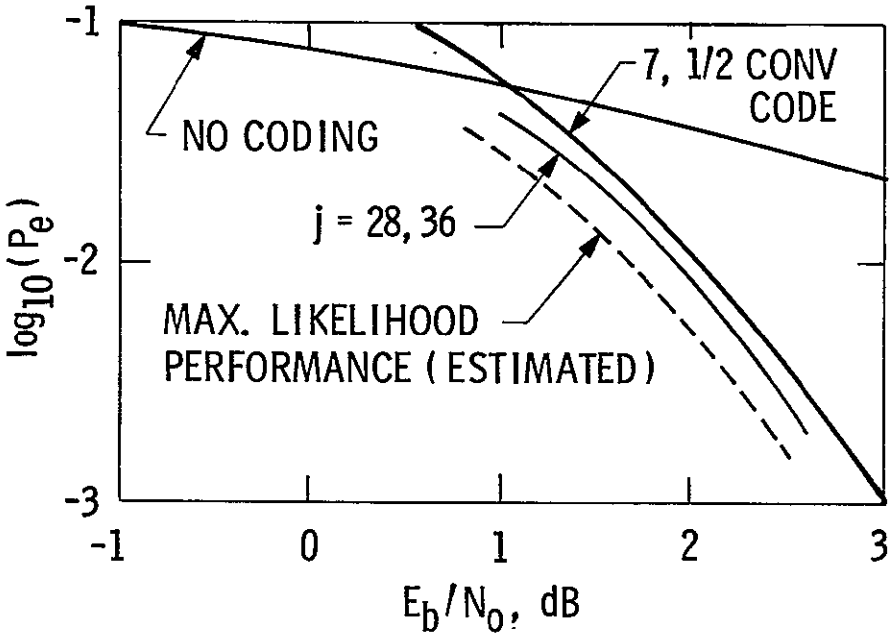

Fig. 2. (80,40) QR, Q = 8.0

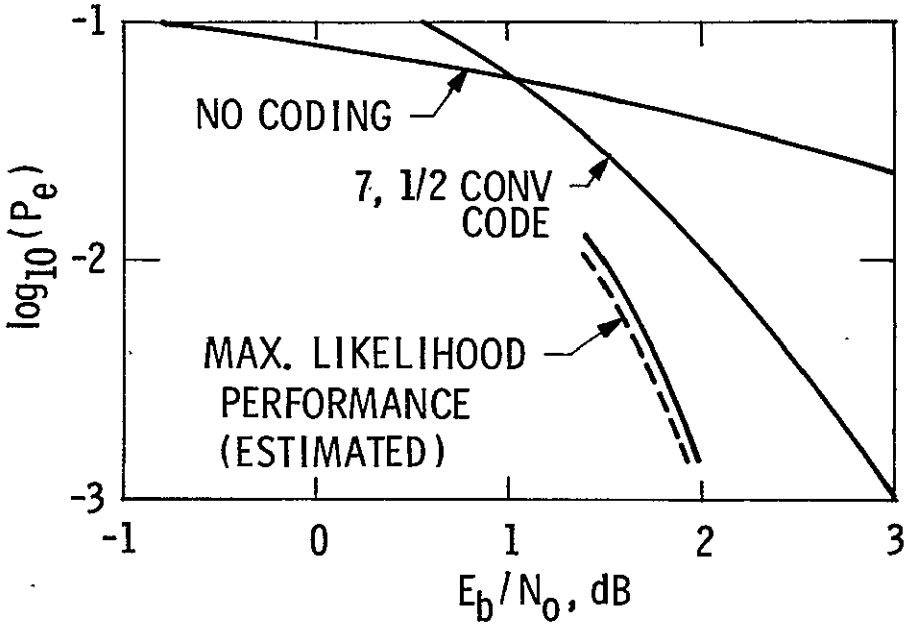

Fig. 3. (128,64) BCH, $Q = 11.0$

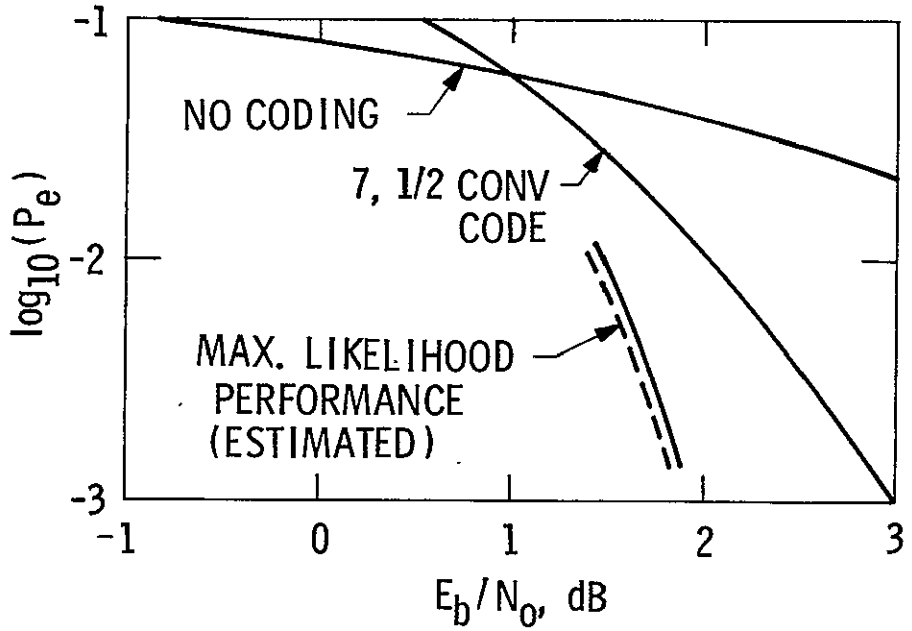

Fig. 4. (128,43) BCH, $Q = 10.75$

Radio Science Requirements and the End-to-End Ranging System

A. L. Berman
TDA Engineering Office

Radio science ranging requirements negotiated between past and present flight projects and the DSN have generally focused on just the DSS and spacecraft hardware. All elements in the end-to-end ranging system must be analyzed and considered in terms of an error hierarchy before reasonable and cost-effective requirements can be levied upon any individual element. This article defines and examines the end-to-end ranging system as it applies to the generation of radio science ranging requirements. Particularly emphasized is the variability of the performance levels of certain of the system elements with respect to the type of radio science experiment being performed and the DSN-spacecraft frequency band configuration.

I. Introduction

To date, negotiations between flight projects and the Deep Space Network (DSN) have assumed that ranging system[1] "errors" occur primarily in the Deep Space Station (DSS) and spacecraft (S/C) hardware, and, therefore, radio science ranging[2] requirements were generally levied solely on these elements. Conversely, the radio science experimenter is typically most concerned with the total data "noise" and "accuracy" of the final *processed* radio science ranging data. It would thus seem immediately apparent that an end-to-end systems approach to radio science ranging requirements would be more appropriate; this article further suggests that without such an approach, requirements levied on a partial subset of elements (i.e., DSS and S/C hardware) as per the current practice will not produce the data quality desired by radio science experimenters, nor will it produce the cost-effective employment of resources.

To illustrate the problem, consider the ranging accuracy level of 2 to 10 centimeters being projected for the Mark IV DSN (1980s). Preliminary calculations (see the appendix), assuming the "ultimate" DSN configuration of S- and X-band simultaneously on uplink and downlink, suggest that for conditions of very dense plasma (i.e., as will apply during relativity experiments), the plasma error *after calibration* will be

[1]The expression "ranging system" is being used generically in this article, and is specifically not meant to imply the more formal DSN "System."

[2]Although this article deals solely with the *radio science* applications of ranging data, it is considered entirely likely that the methodology being here proposed is equally valid in the case of the *navigational* applications of ranging data.

significantly larger than 10 centimeters! Should this prove true, further consideration of a 2- to 10-centimeter ranging system (at least for relativity experiments) would have to be considered as unrealistic.

In the following sections, this article will attempt to define the "end-to-end radio science ranging system," and will explore how such a system description and analysis provides the proper framework for the levying of cost effective and justifiable requirements on both the flight projects and the DSN.

II. The End-to-End Radio Science Ranging System

The end-to-end radio science ranging system is schematically illustrated in Fig. 1. Ranging signals which have been modulated onto a carrier are transmitted from the DSS to the spacecraft, are transponded and retransmitted by the spacecraft, and are received by the DSS, where the range delay information is extracted. During this operation, the ranging signals pass through various interactive media, including the troposphere, ionosphere, and solar wind, which all induce additional and either partially or wholly unknown range delays in the signals. The ranging data are passed from the DSS to the Orbit Determination Program (ODP), along with DSS calibrations consisting of antenna structure measurements and ranging system internal (electrical) delay measurements. In the ODP, both the DSS and spacecraft calibrations (made prior to launch) are applied to the data. In the case of relativity and celestial mechanical experiments, the data are directly referenced to the spacecraft ephemeris, the accuracy of which is determined by the various ODP internal models. An additional error source is the spacecraft unmodeled (or nongravitational) forces. One is now in a position to identify the major elements of the end-to-end radio science ranging system, as follows:

(1) DSS ranging system hardware

(2) Spacecraft Radio Subsystem hardware

(3) Unmodeled spacecraft forces

(4) Interactive media, including

  (a) Troposphere

  (b) Ionosphere

  (c) Solar Wind

(5) DSS antenna structure measurements

(6) DSS internal range delay calibrations

(7) Spacecraft calibrations

(8) Orbit Determination Program, including

  (a) Heliocentric Cruise Models

  (b) Planetary Orbiter Models

  (c) Planetary Lander Models

III. Development of a Radio Science Ranging Error Hierarchy

With the identification of the major elements of the end-to-end radio science ranging system, one wishes to assess the current or projected performance of each element, with the goal being the ranking of the error contributions from largest to smallest. Obviously, it would hardly be cost-effective to levy a performance requirement on a given element which is more stringent than an "inherent" limitation of one or more of the other system elements (unless such a requirement can be levied with little attendant impact on resources). To illustrate with the example of Section I, if there exists an "inherent" plasma limitation of approximately 1 meter, it surely makes little sense to levy the exceedingly difficult requirement of 10-centimeter accuracy on the DSS ranging (hardware) system. What is not generally recognized is that certain of the ranging system elements are variable with regard to:

(1) The *type* of radio science experiment being considered

(2) The DSN and spacecraft *configuration*

and that these elements are in no way directly related to the DSS and spacecraft hardware performance! Further, it is here suggested that these "other" elements are frequently the dominant error sources in radio science ranging experiments.

One can first consider the case of (uncalibrated) plasma errors. Although both single- and dual-frequency plasma range measurements themselves constitute a prime radio science experiment (solar corona/solar wind), plasma becomes a difficult "error" for all other radio science ranging experiments. Although some celestial mechanics experiments may be fortunate in that they are capable of being performed at large Sun-Earth-probe (SEP) angles (i.e., minimum plasma conditions), radio science *relativity* ranging experiments must always be performed under conditions of very dense plasma. For instance, a very preliminary estimate of the plasma "error" during the 1976 Viking ranging relativity experiment is a ranging data noise of about $1\sigma \approx 15$ meters (Ref. 1), over a time scale of several months. The important point here is that this error contribution is a direct function of the (frequency band) configuration of the DSN and spacecraft. Should the S-band uplink be replaced with X-band, one would expect this error source to immediately drop from the 15-meter level to about 1 meter, due simply to the inverse frequency squared plasma dependence. If simultaneous dual-frequency (uplink

and downlink) capability is achieved, this improvement could be expected to be even better.

The Orbit Determination Program (ODP) provides a good example as to how the type (or phase) of a mission directly influences the total end-to-end radio science ranging system performance. It is considered that the ODP modeling of planetary landers has the smallest error, followed by planetary orbiters, and, finally, the worst case, heliocentric cruise. Unfortunately, ODP performance numbers for the three mission phases over the several month time scales of interest are not well known. At any rate, one could generate a *hypothetical* ranging system error hierarchy by making some guesses as to the relative size of the ranging error contribution of plasma, ODP, unmodeled forces, etc. The point of the exercise is to underscore the need to consider the type of the radio science experiment, the DSN and spacecraft frequency band configuration, and spacecraft unmodeled forces, long before one attempts to levy the appropriate requirements on the DSN and spacecraft ranging system hardware performance. Let one *assume* the following error sources (time scales of several months):

(1) Plasma	
(a) S-Band Uplink	15 meters
(b) X-Band Uplink	1 meter
(2) Orbit Determination Program	
(a) Heliocentric Cruise	30 meters
(b) Planetary Orbiter	10 meters
(c) Planetary Lander	3 meters
(3) Unmodeled S/C forces	
(a) Heliocentric Cruise	20 meters
(b) Planetary Orbiter	20 meters
(4) DSS ranging hardware	5 meters
(5) Spacecraft ranging hardware	0.5 meters

The error hierarchy for these assumptions is presented as a function of mission type and frequency band configuration in Fig. 2. The important point of Fig. 2 is that the dominant ranging system errors vary greatly as a function of the mission type or phase and the DSN-spacecraft frequency band configuration, and these are parameters not generally addressed in the generation of radio science ranging requirements.

As an example of the type of decision which might emerge after an end-to-end system error hierarchy is constructed, consider the case of the hypothetical planetary lander of Fig. 2. Normally, if one wanted to achieve a substantial increase in ranging accuracy, one would straightforwardly consider implementing a new generation of DSS ranging hardware. In this particular case, however, it would appear far more cost-effective to stay with the current DSS ranging hardware and implement X-band uplink capability instead.

Celestial mechanics ranging experiments would require a similarly complex error hierarchy. On the other hand, (dual-frequency) plasma experiments are much simpler in that they do not depend on the ODP (models), the uplink frequency band, or spacecraft unmodeled forces. Obviously, the end-to-end ranging system for this type of radio science ranging experiment is vastly simpler, and the appropriate requirements are expected to be generated with far less difficulty.

IV. Performance Validation

As was already mentioned, the only performance of vital interest to the radio science experimenter is the total data accuracy and noise of the final (ODP) processed data. This is the end-to-end system product, and examination and evaluation of such (actual in-flight) data can represent the only true measure of how well radio science ranging requirements are being met. It is true, of course, that individual elements can be tested in stand-alone (DSS hardware) or laboratory (spacecraft hardware) environments, or possibly via simulation (ODP software); however, final processed in-flight data over time scales of several months must be considered the final standard by which the success in meeting radio science ranging requirements for relativity and celestial mechanics experiments is gauged.

Dual-frequency downlink plasma experiments are an entirely different case, however; here the major determinant of accuracy is the DSS hardware and calibrations, and these can be routinely validated for time scales under 12 hours via the dual-frequency equivalent of the "pseudo-DRVID" scheme (Ref. 2). In this approach differenced dual-frequency range measurements are compared to (integrated) dual-frequency doppler measurements. Also, single-frequency range measurements can be used in the same fashion to check a subset of the end-to-end radio science ranging system elements (DSS and spacecraft hardware, DSS calibrations) over time scales of less than 12 hours.

One finally concludes that the only pertinent tests of the end-to-end ranging system for the relativity and celestial mechanics experiments are:

evaluation of processed in-flight data

and for dual-frequency downlink plasma experiments:

dual-frequency pseudo-DRVID

V. Summary

Radio science ranging requirements negotiated between past and present flight projects and the DSN have generally focused on just the DSS and spacecraft hardware. All elements in the end-to-end system must be analyzed and considered in terms of the error hierarchy before reasonable and cost-effective requirements can be levied upon any individual element. Quite important to this process are plasma and ODP software considerations, which are shown to be especially complex in that their performance level depends on the type of radio science experiment to be performed and the DSN-spacecraft configuration. Finally, it is noted that while laboratory or stand-alone type tests of individual elements may be possible and useful in an interim sense, the final validation of radio science ranging system performance can only be achieved via evaluation of the final processed in-flight radio science ranging data themselves.

References

1. Anderson, J. D., private communication (meeting, June 7, 1978).
2. Berman, A. L., "Pseudo-DRVID: A New Technique for Near-Real-Time Validation of Ranging System Data," in *The Deep Space Network Progress Report 42-29,* pp. 180-187, Jet Propulsion Laboratory, Pasadena, Calif., Oct. 15, 1975.
3. Berman, A. L., "Phase Fluctuation Spectra: New Radio Science Information to Become Available in the DSN Tracking System Mark III-77," in *The Deep Space Network Progress Report 42-40,* pp. 134-140, Jet Propulsion Laboratory, Pasadena, Calif., Aug. 15, 1977.
4. Berman, A. L., "A Telecommunications 'Design Table' for The Solar Corona," IOM ALB-77-63, Sept. 21, 1977 (JPL internal document).

Appendix

Inherent Ranging Accuracy Limitations Under Conditions of Dense Plasma

One would like to know what the residual (i.e., uncalibrated) plasma errors might be when X-band uplink capability is achieved. Two very preliminary methods of calculating the expected error for near sun ranging both yield errors at about the 1-meter level. The calculations are described below.

A. X-Band Uplink; S- and X-Band Downlink

The simplest method of producing plasma corrections when dual-frequency downlink is available is to "double" the downlink dual-frequency (differenced) range. Assuming that the range delay is induced at the signal path closest approach point and given a signal Round-Trip-Light-Time (RTLT) and closest approach distance, one can use the Solar Wind Phase Fluctuation Spectrum (Ref. 3) to deduce the expected range error. Assuming an RTLT of 4000 seconds (which yields approximately 3000 seconds as the time between uplink and downlink closest approach) and a closest approach distance of 10 solar radii, one expects a range error of about 20 meters at S-band. To translate this error to X-band uplink, one simply scales by the square of the ratio of S-band to X-band (3/11), which immediately yields an "inherent" plasma limitation for near sun ranging with X-band uplink of approximately 1.5 meters.

B. Simultaneous S- and X-Band Uplink and Downlink

Theoretically, round-trip dual-frequency range measurements should provide "perfect" plasma calibrations. Unfortunately, the X-band uplink being implemented is in a slightly different ratio to the S-band uplink than is the X-band downlink as compared to S-band downlink (i.e., the spacecraft S- and X-band turnaround ratios will be slightly different). This effect will cause an error in the *round trip* plasma measurement of perhaps 1 to 10 percent. Again assuming a closest approach distance of 10 solar radii, one has (Ref. 4) an S-band plasma delay of 1200 meters, or, scaling to X-band, 90 meters. If one optimistically assumes that the round-trip plasma measurement is good to 1 percent, one is still left with an error of approximately 0.9 meter for near sun ranging with simultaneous S- and X-band on both uplink and downlink.

In conclusion, even assuming the 1980s implementation of X-band uplink, it is difficult to see that near Sun ranging (as is required by relativity experiments) can be achieved beyond about the 1-meter accuracy level.

Fig. 1. The end-to-end radio science ranging system

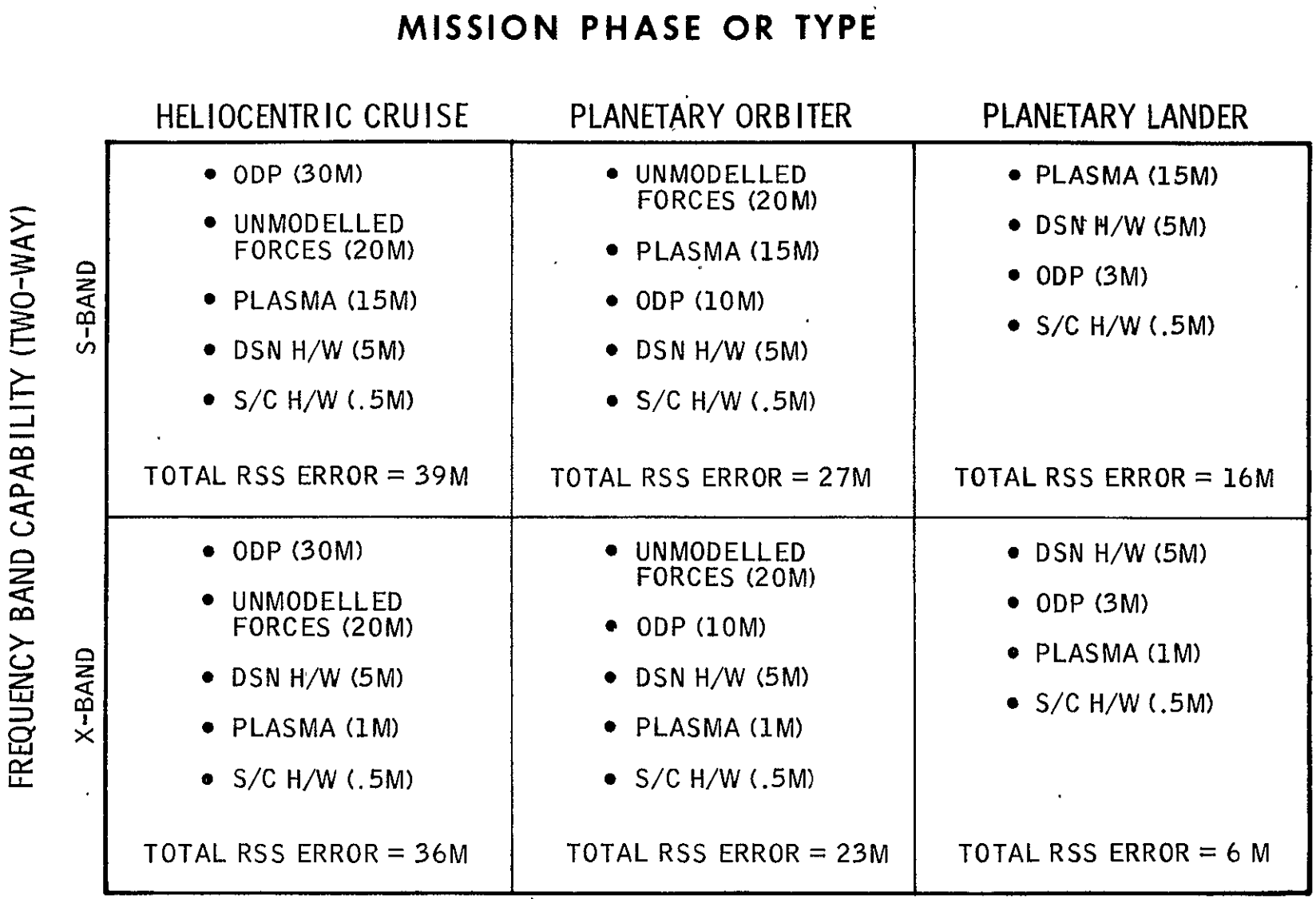

Fig. 2. Hypothetical error matrix for a radio science relativity experiment

D11

Parametric Modeling of Low-Frequency Water-Vapor-Induced Tropospheric Path Length Fluctuations

A. L. Berman
TDA Engineering Office

Detailed wet tropospheric fluctuation information will be required to support proposals to search for gravitational waves in ultra-precise Doppler data. In this article, similarities between the solar wind and tropospheric effects on apparent signal path length ("signal delay") are used to hypothesize the following parametric model for low-frequency wet tropospheric path length fluctuation (with σ_{R_w} = RMS signal delay fluctuation, R_{wz} = total zenith signal delay, θ = elevation angle, and τ_a = averaging time):

$$\sigma_{R_w}(R_{wz},\theta,\tau_a) = 2 \times 10^{-2} R_{wz} (\sin\theta)^{-1} (\tau_a/1000)^{0.6}$$

Recent experimental observations of wet tropospheric signal delay fluctuations can be interpreted as confirming this parametric form. The model is used to suggest the appropriate conditions for collection of experimental tropospheric fluctuation data.

I. Introduction

Proposals have recently been advanced to search for "gravitational waves" in ultra-precise two-way Doppler data. Preliminary estimates of gravitational wave characteristics indicate that a total measurement system fractional frequency fluctuation ($\sigma(\Delta F/F)$, where F is an S- or X-band frequency) of 1×10^{-15} over the time scales of interest (50 to 5000 seconds) will be required (Ref. 1). At this level, fluctuations in the wet (water vapor) component of the tropospheric signal delay (R_w) will surely constitute a major error source. Unfortunately, little work has been done to date on the (complete) parametric form of the wet tropospheric fluctuation spectrum. This article *hypothesizes* a tropospheric fluctuation model based on observed functional similarities in the tropospheric and solar wind effects on microwave frequency propagation. The derived model is then utilized to suggest appropriate conditions for the acquisition of experimental tropospheric fluctuation data.

II. Derivation of a Tropospheric Fluctuation Model

The recent past has seen a considerable effort expended in the parametric modeling of the solar wind fluctuation spectrum (for example, Refs. 2 and 3). In light of functional similarities between the troposphere and solar wind, it seems reasonable to investigate whether this recently acquired knowledge might be useful in understanding and modeling tropo-

spheric fluctuations. Although the solar wind is composed of charged particles, in contrast to the neutral particles of the wet troposphere, there are two very basic similarities between the solar wind and the troposphere:

(1) The apparent signal path length ("signal delay") increases in proportion to the total columnar particulate matter.

(2) The particulate matter convects as a "wind" across and along the signal path.

The recently found significant features of the solar wind fluctuation spectrum (for instance, Refs. 2 and 3) are as follows:

(1) The fluctuations are power law with time scale.

(2) The fluctuations are proportional to the total particulate density along the signal path.

Experimental evidence that wet tropospheric signal delay fluctuations are power law with time scale has been obtained by Thompson *et al.*, (Ref. 4). Further, Thompson is quoted (Ref. 5) as stating: "The RMS phase fluctuation is proportional to the total path length." Since the test paths utilized by Thompson are line-of-sight between surface (Hawaiian) stations, one expects a nearly constant water vapor density *per unit path length*, and hence a total columnar density nearly proportional to the total path length. Thompson's statement would certainly appear to imply experimental confirmation that wet tropospheric signal delay fluctuations are (approximately) proportional to total (particulate) columnar density.

If one were to use these relationships in hypothesizing a wet tropospheric fluctuation model, the result would be:

$$\sigma_{R_w}(R_w, \tau_a) = K_0 R_w (\tau_a)^{K_1}$$

where

σ_{R_w} = RMS wet tropospheric path length fluctuation

τ_a = averaging time, seconds

R_w = total wet tropospheric path length, centimeters

K_0, K_1 = coefficients

One further models (Ref. 6) the wet tropospheric signal delay variation with elevation angle as:

$$R_w \approx R_{wz} (\sin \theta)^{-1}$$

where

R_{wz} = total wet tropospheric path length at zenith, centimeters

θ = elevation angle

so that one has a parametric form as follows:

$$\sigma_{R_w}(R_{wz}, \theta, \tau_a) = K_0 R_{wz} (\sin \theta)^{-1} (\tau_a)^{K_1}$$

It would now be appropriate to inquire as to expected values for the coefficients K_0 and K_1. Thompson (Ref. 4) determined a value of −2.6 for the wet tropospheric columnar fluctuation spectral index. This directly yields a value for K_1 of 0.8, which, rather interestingly, happens to be very close to the numerical value for the columnar solar wind fluctuation (~0.7). A value for K_0 cannot be obtained directly from Ref. 4 since total wet tropospheric signal delay values are not indicated for the phase spectral density measurements; however, Ref. 7 provides a very tentative estimate of:

$$\sigma_{R_w} \approx 2 \times 10^{-2} (R_w); \qquad \tau_a = 1000 \text{ seconds}$$

These estimates for K_0 and K_1 yield:

$$\sigma_{R_w}(R_{wz}, \theta, \tau_a) = 2 \times 10^{-2} R_{wz} (\sin \theta)^{-1} (\tau_a/1000)^{0.8}$$

The model is tested for reasonableness by computing the averaging time for which:

$$\sigma_{R_w}/R_w = 0.5$$

The value of 0.5 (σ_{R_w}/R_w) is chosen as an upper bound for the very low frequency fluctuations. With this model a value of 0.5 is achieved for averaging times of about 16 hours. This (averaging time) value seems somewhat small; one might expect the lowest frequency fluctuations to be related to the movement of large scale air masses occurring over periods of several days, at least for temperate, semi-arid Deep Space Station (DSS) locations like Goldstone, California (one could expect a substantially different very low frequency wet tropospheric fluctuation spectrum for radically different climatic environments; for example, near ocean, tropical, and polar). To accommodate the expected DSS climatic environment, a value of 0.5 (σ_{R_w}/R_w) will be adopted for τ_a = 260,000 seconds (approximately 3.0 days); this yields a somewhat smaller value for K_1 (≈ 0.6). The final hypothesized wet tropospheric model then becomes:

$$\sigma_{R_w}(R_{wz}, \theta, \tau_a) = 2 \times 10^{-2} R_{wz} (\sin \theta)^{-1} (\tau_a/1000)^{0.6}$$

III. Model Results

Two bounding cases are briefly considered as follows:

(1) Desert winter (cold and dry)

$$R_{wz} \approx 2 \text{ centimeters}$$

(2) Desert summer (warm and humid)

$$R_{wz} \approx 20 \text{ centimeters}$$

These assumptions translate to fractional frequency fluctuation as follows (with $\sigma(\Delta F/F) \equiv \sigma_{R_w}/\tau_a \cdot c$; c = speed of light):

R_{wz} \ τ_a	100 seconds	1000 seconds
2 centimeters	$3.3 \times 10^{-15} (\sin\theta)^{-1}$	$1.3 \times 10^{-15} (\sin\theta)^{-1}$
20 centimeters	$3.3 \times 10^{-14} (\sin\theta)^{-1}$	$1.3 \times 10^{-14} (\sin\theta)^{-1}$

The above data are graphically illustrated in Fig. 1. The significance of these very preliminary estimates is that for the following conditions:

(1) Winter climatic conditions

(2) Longer averaging times

(3) Near zenith observations

wet tropospheric signal delay fluctuations may not pose too serious an error source for the gravitational wave detection experiment. On the other hand, the following conditions:

(1) Summer climatic conditions

(2) Shorter averaging times

(3) Low elevation observations

will most certainly present a very difficult error source for the gravitational wave detection experiment.

IV. Discussion and Summary

Knowledge of low frequency wet tropospheric fluctuation will be very important to the suggested use of ultra-precise Doppler data in the search for gravitational waves. By noting the similarities between the solar wind and the troposphere, one can hypothesize a parametric model for the tropospheric path length fluctuations. In addition, recent experimental observations of the wet tropospheric signal delay fluctuation spectrum can be interpreted as confirmation of the hypothesized model.

The hypothesized model immediately suggests certain bounding conditions under which experimental tropospheric fluctuation data should be acquired. These are as follows (chosen to maximize the expected parametric variations):

(1) Climatic conditions

  (a) Winter (cold and dry)

  (b) Summer (warm and humid)

(2) Elevation angle

  (a) Zenith

  (b) Near horizon

(3) Averaging times

  (a) 60 seconds

  (b) 260,000 seconds

References

1. Berman, A. L., "The Gravitational Wave Detection Experiment: Description and Anticipated Requirements," in *The Deep Space Network Progress Report 42-46*, pp. 100-108, Jet Propulsion Laboratory, Pasadena, Calif., Aug. 15, 1978.

2. Berman, A. L., "Phase Fluctuation Spectra: New Radio Science Information To Become Available in the DSN Tracking System Mark III-77," in *The Deep Space Network Progress Report 42-40*, pp. 134-140, Jet Propulsion Laboratory, Pasadena, Calif., Aug. 15, 1977.

3. Berman, A. L., "Solar Wind Turbulence Models Evaluated via Observations of Doppler RMS Phase Fluctuation and Spectral Broadening in the Inner Corona," in *The Deep Space Network Progress Report 42-44*, pp. 197-202, Jet Propulsion Laboratory, Pasadena, Calif., Apr. 15, 1978.

4. Thompson, M. C., Wood, L. E., Harris, B. J., and Smith, D., "Phase and Amplitude Scintillations in the 10 to 40 GHz Band," *IEEE Transactions on Antennas and Propagation*, Vol. AP-23, No. 6, Nov. 1975.

5. Callahan, P. S., "A First Look at Errors from Small Scale Tropospheric Fluctuations," IOM 315.1-272, Apr. 24, 1978 (JPL internal document).

6. Ondrasik, V. J., and Thuleen, K. L., "Variations on the Zenith Tropospheric Range Effect Computed from Radiosonde Balloon Data," in *Space Programs Summary 37-65*, Volume II, Jet Propulsion Laboratory, Pasadena, Calif., Sept. 30, 1970.

7. Berman, A. L., "Gravitational Wave Detection Requirements for Calibration of the Troposphere," IOM ALB-78-16, Jan. 26, 1978 (JPL internal document).

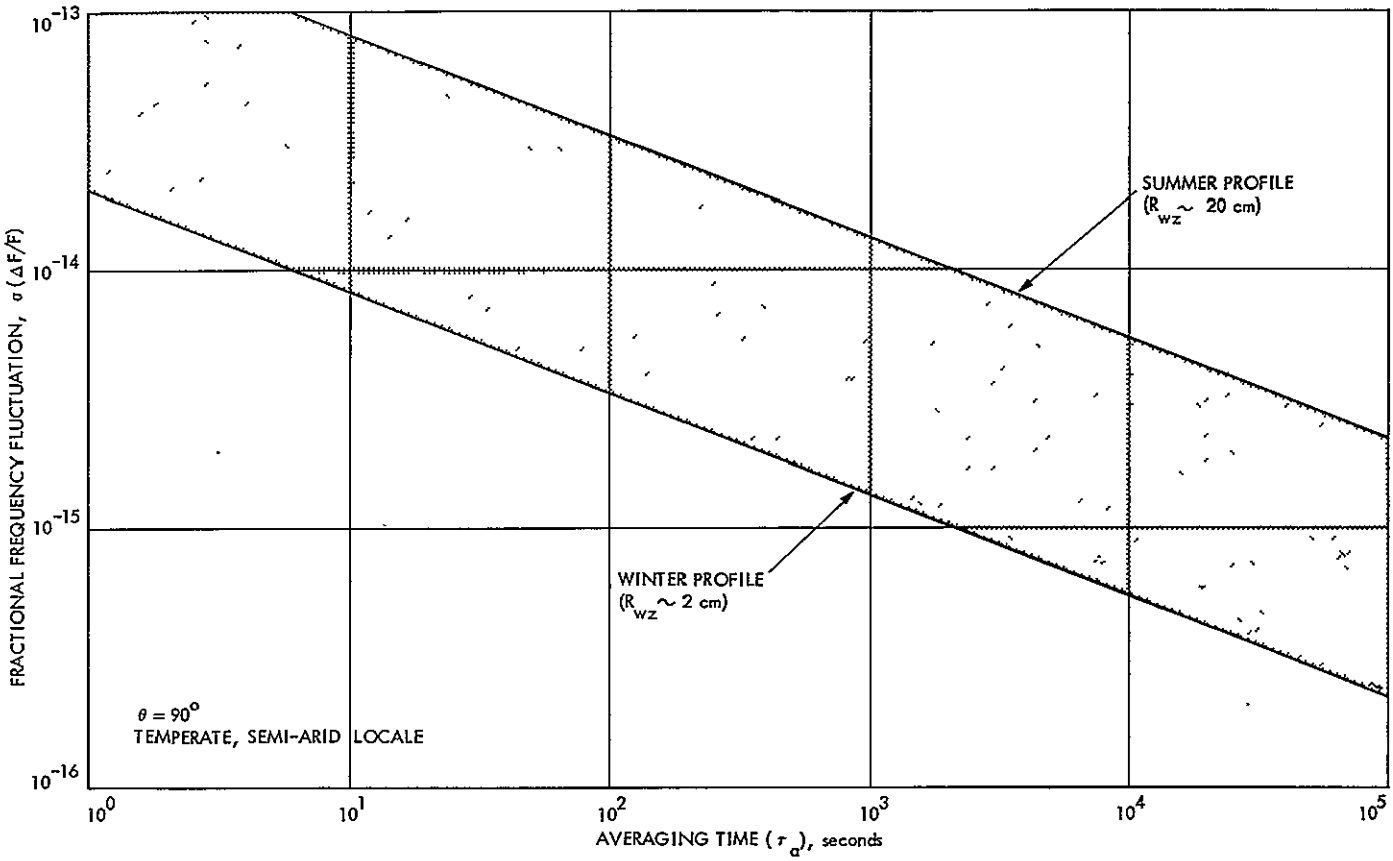

Fig. 1. Wet tropospheric signal delay fluctuation versus averaging time

Updated Z-Corrections for 64-m DSS Ground Station Delay Calibrations

T. Y. Otoshi
Radio Frequency and Microwave Subsystems Section

K. R. Weld
Deep Space Network Operations Section

This article presents new Z-corrections which resulted from recent translator path delay calibrations made at DSS 14, 43, and 63 with newly developed DSN Portable Zero Delay Assemblies.

I. Introduction

In recent months, new Portable Zero Delay Assemblies (PZDA) were developed for the DSN (Ref. 1). These PDZAs were shipped to DSS 14, 43, and 63 for purposes of making calibrations of the Block IV translator paths. Each of the 64-m antenna stations is now equipped with its own calibrated PDZA and is therefore capable of making translator path delay calibrations upon request.

The purpose of this article is to provide the necessary information and data required by Network Operations to make future Z-correction calculations based upon the translator delay values furnished by each 64-m Deep Space Station. It is also the purpose of this article to show that the technology for the "Translator Method" (Ref. 2) has been successfully transferred to Network Operations.

II. Z-Correction Equation

As discussed in Ref. 2, Z-corrections are necessary for correcting the measured ground station delays and referring them to the DSS reference location. This information is needed for determining the true range to the spacecraft. The Z-corrections for 64-m Deep Space Stations are determined from the basic equation derived in Ref. 2 for the Block 4 Translator Method. This equation is:

$$Z = \tau_{XLTR} - \sum_{i=3}^{6} \tau_i \qquad (1)$$

where τ_{XLTR} is the delay of the translator path between the uplink sampling point and the downlink injection point. The term τ_3 is the microwave delay from the uplink sampling point to the transmit horn phase center and τ_4 is the microwave delay from the receive horn phase center to the downlink injection point. The terms τ_5 and τ_6 are, respectively, the uplink and downlink airpath delays from the horn phase centers to the DSS reference location via the convoluted Cassegrain antenna optics paths. These terms are defined more clearly and precisely in Ref. 2.

As may be seen in Eq. (1), one of the terms needed to determine the Z-correction is the translator path delay τ_{XLTR}. This term includes the delays of the Level Set Attenuator Assembly, Block IV Translator Assembly, Test Signal Control Assembly, and interconnecting cables. Because of the complexity of this path, this delay is measured rather than calculated.

The procedure for the measurement of τ_{XLTR} has been described previously in Refs. 3 and 4 and repeated here for convenience. A portable Zero Delay Device (ZDD) and its cables are substituted for the Block IV translator path and the range delay R_{ZDD} is measured. Then the *ZDD* cables are inserted in series with the Block IV translator path and the range delay is again measured and denoted as R_{XLTR}. The measured translator delay is calculated from (see Ref. 3 for derivation)

$$(\tau_{XLTR})_m = R_{XLTR} - R_{ZDD} + \tau_{ZDD} \qquad (2)$$

where τ_{ZDD} is the delay of the portable *ZDD* without its external cables. This value of τ_{ZDD} is known and had been precisely precalibrated in the laboratory. For future reference purposes, the values of τ_{ZDD} for the PDZA at each 64-m DSS is tabulated in Table 1. It should be pointed out that the terms R_{ZDD} and R_{XLTR} in Eq. (2) are symbols used in DSN test procedures. They are the same as the terms D_{ZDD} and D'_{XLTR} defined in Refs. 3 and 4.

Equation (2) results in a measured value of the translator path between coaxial connection points to which the *ZDD* cables can be conveniently connected. This is the value furnished by the station using DSN Test Procedures 853-100. However, the actual translator path must be defined internal to the waveguide system to points common to the "range on S/C path." Therefore, small corrections need to be applied to the measured values for the additional lengths of coax to waveguide paths involved. The true translator path delay is determined from the expression

$$\tau_{XLTR} = (\tau_{XLTR})_m + \tau_{WG,up} + \tau_{WG,down} \qquad (3)$$

The term $\tau_{WG,up}$ is a small correction term needed to go from the actual measurement uplink sampling point to the same point where τ_3 is defined. The term $\tau_{WG,down}$ is a small correction term needed to go from the actual measurement downlink sampling point to the same point where τ_4 is defined.

The current values of constants needed to calculate Z-corrections from Eqs. (1) and (3) are tabulated in Table 2. It should be pointed out that the S-band constants at DSS 14 are different from those of DSS 43 and 63 because of a dual coupler configuration which was implemented in June 1977. The terms τ_3, τ_4, τ_{XLTR} at DSS 14 are defined at a common reference plane where the WR430 flange on the dual coupler assembly connects to the WR430 switch SW3. The terms $\tau_{WG,up}$ and $\tau_{WG,down}$ are the delays between the coaxial sampling-injection ports on the dual coupler and the described common reference plane. For the X-band downlink path, τ_4 and τ_{XLTR} are defined up to the midpoint of the X-band waveguide coupler installed directly in front of the XRO maser. For X-band the last coaxial connection point is the input to the XRO noise box, and the correction term $\tau_{WG,down}$ is the additional delay of the waveguide run through the XRO noise box assembly to the midpoint of the X-band waveguide coupler.

At DSS 43 and 63, τ_{XLTR} for the (S,S) path is defined between a high-power WR430 coupler (located in the Mod III Section) and the midpoint of a WR430 crossguide coupler installed in front of the SPD maser. At these two overseas stations, the term $\tau_{WG,up}$ value is assumed to be negligibly small. The term $\tau_{WG,down}$ for S-band is the small (but non-negligible) delay between (1) a 7/8 coaxial port on the 7/8-to-WR430 transition connected to the SPD maser WR430 crossguide coupler and (2) the midpoint of the SPD maser crossguide coupler. The $\tau_{WG,down}$ value for X-band is defined between the same points described above for DSS 14.

The constants given in Table 2 may undergo changes in the future if any changes are made in the S/X feed system for the SPD and XRO cones. It is expected that if new configurations affect these tabulated constants, the JPL section responsible for the redesign and implementation will provide new values to Network Operations.

III. Measured Values

During the period of May through July 1978, at the request of Network Operations, measurements were made by the 64-m stations to calibrate the translator path delays using the new PDZAs. Some difficulties were experienced at some of the stations, and therefore reliable test data was not obtained until July 31. The test procedures have since been revised to help overcome some of the problems experienced by station personnel.

The final measured translator path delays and new Z-corrections for DSS 14, 43, and 63 are presented in Tables 3-5. The Z-corrections are average values for the frequencies of Channels 5 through 25. (The relationship of channel numbers to frequency may be found in Table 1 of Ref. 3.) It should be pointed out that at both DSS 14 and DSS 43, the Z-correction

for X-band appears to be frequency-sensitive. For critical experiments involving interstation ranging comparisons, it is recommended that instead of using the average X-band value, Z-corrections be determined specifically for the channel frequencies involved. All of the necessary values for recalculating Z-corrections at a particular channel are supplied in this article.

For comparison purposes, the old and new translator path delays and Z-corrections for all 64-m DSS are shown in Table 6. Examination of the data for DSS 14 shows that the old and new Z-correction values agree to within 0.2 m at both S- and X-band. For DSS 43 and 63, the old and new Z-correction values agree to within 2.2 m at S-band and ±1.0 m at X-band. Causes of the disagreement for DSS 43 and 63 values are difficult to determine. It is possible that since the calibrations at these two overseas stations were last performed about 2.5 years ago, cable and component changes might have been made in the translator paths without our knowledge*. At DSS 14, the last calibration was performed about 1 year ago and the configuration remained basically unchanged. It is recommended that Network Operations have these calibrations performed more often (on a 6-month periodic basis) or whenever a major known configuration change is made in the translator path.

*After submitting this article for publication, investigations made of past ECOs revealed that new cables and components had been added to the (S,S) translator path at the overseas stations. These additions account for most of the changes observed in the (S,S) translator path values shown in Table 6.

IV. Concluding Remarks

New Z-corrections for 64-m stations have been derived. These new values are based upon translator path delay measurements made with a new PDZA supplied to each 64-m DSS. In the case of DSS 14 measurements, the values of old and new Z-corrections agreed within 0.2 m. Considering that the old values at DSS 14 were obtained with the use of an R&D portable ZDD and new values were obtained with a DSN PDZA having different cables and internal mixers and components, the results are very encouraging and lend confidence to the measurement technique.

The test results indicate a successful transfer of technology from development to implementation and finally to the operations phase. Each 64-m station is now capable of making these measurements upon request, and constants have been supplied to Network Operations for making future Z-correction calculations. It is recommended that Z-correction determinations be repeated on a periodic 6 month basis.

References

1. Serhal, E. J., and Otoshi, T. Y., "DSN Portable Zero Delay Assembly," in *The Deep Space Network Progress Report 42-46*, pp. 130-138, Jet Propulsion Laboratory, Pasadena, Calif., Aug. 15, 1978.
2. Komarek, T., and Otoshi, T., "Terminology of Ranging Measurements and DSS Calibrations," in *The Deep Space Network Progress Report 42-36*, pp. 35-40, Jet Propulsion Laboratory, Pasadena, Calif., Dec. 15, 1976.
3. Otoshi, T. Y., Batelaan, P. D., Wallace, K. B., and Ibanez, F., "Calibration of Block 4 Translator Path Delays at DSS 14 and CTA 21," in *The Deep Space Network Progress Report 42-37*, pp. 188-197, Jet Propulsion Laboratory, Pasadena, Calif., Feb. 15, 1977.
4. Otoshi, T. Y., Wallace, K. B., and Lyon, R. B., "Dual Coupler Configuration at DSS 14 for the Voyager Era," in *The Deep Space Network Progress Report 42-42*, pp. 184-192, Jet Propulsion Laboratory, Pasadena, Calif., Dec. 15, 1977.

Table 1. Calibrated delays for DSN portable zero delay assemblies

DSS	Serial number	τ_{ZDD}, ns (S,S) path	τ_{ZDD}, ns (S,X) path
14	2	18.84	14.28
43	3	18.13	14.18
63	4	18.24	13.93

Table 2. Constants for Z-correction calculations

DSS	$\tau_{WG,up}$, ns	$\tau_{WG,down}$, ns	τ_3, ns	τ_4, ns	Airpath τ_5, ns	Airpath τ_6, ns
(S,S) path[a]						
14	0.42	0.41	22.18	19.66	102.56	102.56
43	–	1.05	62.00	45.44	102.56	102.56
63	–	1.05	62.00	45.44	102.56	102.56
(S,X) path[b]						
14	0.42	6.01	22.18	5.34	102.56	93.42
43	–	6.01	62.00	5.34	102.56	93.42
63	–	6.01	62.00	5.34	102.56	93.42

[a]DSS 14 only has the dual coupler configuration. The constants for DSS 14 are the same as given in Ref. 4.

[b]Some of the values for DSS 43 and 63 have been changed from previously reported values in JPL internal memos because of improved S- and X-band horn delay values and XRO cone updates at the overseas stations.

Table 3. DSS 14 calibrations (July 30, 1978)

Measured translator path delays

Channel	$(\tau_{XLTR})_m$, ns		Comments
	(S,S) path	(S,X) path	
5	203.7	173.7	S-band measurement corrected for missing cable
9	204.0	168.5	
14	206.4	170.3	
17	209.0	173.0	
21	206.7	170.0	
25	207.1	158.4	X-band delay is about 10 ns shorter than average
Average	206.15 ±0.82(1σ)	168.98 ±2.26(1σ)	

Corrected translator path delays and Z-corrections

Path	Average $(\tau_{XLTR})_m$, ns	$\tau_{WG,up}$, ns	$\tau_{WG,down}$, ns	τ_{XLTR}, ns	$\sum_{i=3}^{6}\tau_i^a$, ns	Z_r, ns	Z_r, m
(S,S)	206.15	0.42	0.41	206.98	246.96	−39.98	−5.99
(S,X)	168.98	0.42	6.01	175.41	223.50	−48.09	−7.21

[a]See Table 2

Table 4. DSS 43 calibrations (May 26, 1978)

Measured translator path delays			
Channel	$(\tau_{XLTR})_m$, ns		Comments
	(S,S) path	(S,X) path	
5	181.1	183.8	
9	184.8	186.6	
14	[184.7 185.6]	[179.8 181.7]	
18	185.5	175.9	Delay at X-band is about 5.6 ns lower than average
21	189.2	178.7	
25	187.2	184.2	
Average	185.44 ±0.94(1σ)	181.53 ±1.39(1σ)	

Corrected translator path delays and Z-corrections								
Path	Average $(\tau_{XLTR})_m$, ns	$\tau_{WG,up}$, ns	$\tau_{WG,down}$, ns	τ_{XLTR}, ns	$\sum_{i=3}^{6} \tau_i$[a], ns	Z_s, ns	Z_s, m
(S,S)	185.44	–	[1.05 + 2.93][b]	189.42	312.56	−123.14	−18.46
(S,X)	181.53	–	6.01	187.54	263.32	−75.78	−11.36

[a] See Table 2.

[b] Actual measurement point used was not as specified in DSN test procedures. Therefore additional correction of 2.93 ns was required.

Table 5. DSS 63 calibrations (May 10, 1978 and July 31, 1978)

Measured translator path delays

Channel	$(\tau_{XLTR})_m$, ns		Comments
	(S,S) path	(S,X) path	
5	184.1	173.6	
9	187.8	174.0	
14	193.3 186.7	170.7 171.0	Second row numbers at this channel are from the May 10, 1978, measurement
17	188.5	171.5	
21	188.4	171.6	
25	192.1	169.2	
Average	188.70 ±1.18(1σ)	171.66 ±0.63(1σ)	

Corrected translator path delays and Z-corrections

Path	Average $(\tau_{XLTR})_m$, ns	$\tau_{WG,up}$, ns	$\tau_{WG,down}$, ns	τ_{XLTR}, ns	$\sum_{i=3}^{6} \tau_i$[a], ns	Z, ns	Z, m
(S,S)	188.70	–	1.05	189.75	312.56	−122.81	−18.4i
(S,X)	171.66	–	6.01	177.67	263.32	−85.65	−12 84

[a]See Table 2.

Table 6. Comparisons of old and new values of corrected translator path delays and Z-corrections for 64-m DSS

Old values					
DSS	Band	τ_{XLTR}, ns	Z, ns	Z, m	Approx. date of calibration
14	S	208.13	−38.83	−5.82	June 15, 1977
	X	174.83	−48.67	−7.30	
43	S	176.95	−136.37	−20.46	Dec. 3, 1975
	X	183.41	−81.17	−12.18	Dec. 19, 1975
63	S	176.02	−137.30	−20.60	Jan. 20, 1976
	X	184.31	−80.27	−12.04	

New values					
DSS	Band	τ_{XLTR}, ns	Z, ns	Z, m	Date of calibration
14	S	206.98	−39.98	−5.99	July 30, 1978
	X	175.41	−48.09	−7.21	
43	S	189.42	−123.14	−18.46	May 26, 1978
	X	187.54	−75.78	−11.36	
63	S	189.75	−122.81	−18.41	July 31, 1978
	X	177.67	−85.65	−12.84	

DSN Progress Report 42-47 July and August 1978

Dual-Frequency Feed Cone Assemblies for 34-Meter Antennas

R. W. Hartop
Radio Frequency and Microwave Subsystems Section

New Cassegrain cone assemblies have been designed for the upgrade of three 26-meter-diameter antennas to 34-meter diameter with improved performance. The new dual-frequency feed cone (SXD) provides both S- and X-band feed systems and traveling wave masers with a reflex reflector system to permit simultaneous operation analogous to the 64-meter antennas. One cone assembly has been completed and two more are in fabrication, with deliveries set for early and midyear 1979.

I. Introduction

In order to extend the capabilities of a subnet of 26-m antennas, three stations are being upgraded to 34-m diameter with improved structural and microwave performance. The early design and performance goals have been reported in earlier articles (Refs. 1 and 2).

II. SXD Cone Assembly for DSS 12

Since the last reporting, the first SXD cone has been fabricated, assembled, tested at high power, and transferred to operations for installation on the upgraded DSS 12 antenna during August 1978. The cone exterior is shown in Fig. 1. The S-band horn is in the foreground and the X-band horn is atop the cone extension.

Figure 2 shows the S-band diplexer and low-noise (receive-only) bypass loop of waveguide that connect to the switches. Part of the S-band feed horn can be seen behind the diplexer.

Figure 3 shows the lower portions of the S-band feed, including the polarizer and rotary joints. To the left of the picture is the transmitter waveguide run and transmit filter.

Figure 4 shows the X-band monitor receiver and maser support racks during the final stages of assembly and cabling. This is the first installation and use of the new traveling wave maser package design.

III. Performance Tests

During June the first SXD cone assembly was transported to the Microwave Test Facility at Goldstone and connected to the test transmitter. Repeated tests at 20 to 24 kW CW showed no significant noise bursts or system noise temperature increase while diplexing the cone-mounted maser. With the ellipsoidal reflector and dichroic plate mounted atop the cone, the same results were obtained. Measured system temperatures at S-band were approximately 14 kelvins in the low-noise

receive-only configuration (diplexer bypassed) and .22 kelvins in the diplexed configuration. It is expected that each of these figures will increase about 4 kelvins when the cone is mounted on the DSS 12 antenna due to quadripod scatter and spillover.

At X-band the system temperature was 17.5 K without the dichroic plate installed. Because of backscatter reaching the ground when the cone is not on the antenna, the installation of the dichroic plate caused a 3.6-K increase in noise temperature. This is expected to be reduced to less than 2.5 K on the antenna which, with the other contributions, should make the final X-band temperature about 24 K.

IV. Overseas SXD Cone Assemblies

Fabrication of all parts is nearly complete for two more SXD cones, and assembly of the second unit is beginning. Assembly of the third unit is expected to begin in September. When completed, these cone assemblies will also be tested at Goldstone prior to overseas shipment.

References

1. Hartop, R. W., "Dual Frequency Feed System for 26-Meter Antenna Conversion," in *The Deep Space Network Progress Report 42-40*, Jet Propulsion Laboratory, Pasadena, Calif., Aug 15, 1977.
2. Nixon, D. L., and Bathker, D., "S/X-Band Microwave Optics Design and Analysis for DSN 34-Meter-Diameter Antenna," in *The Deep Space Network Progress Report 42-41*, Jet Propulsion Laboratory, Pasadena, Calif., Oct 15, 1977.

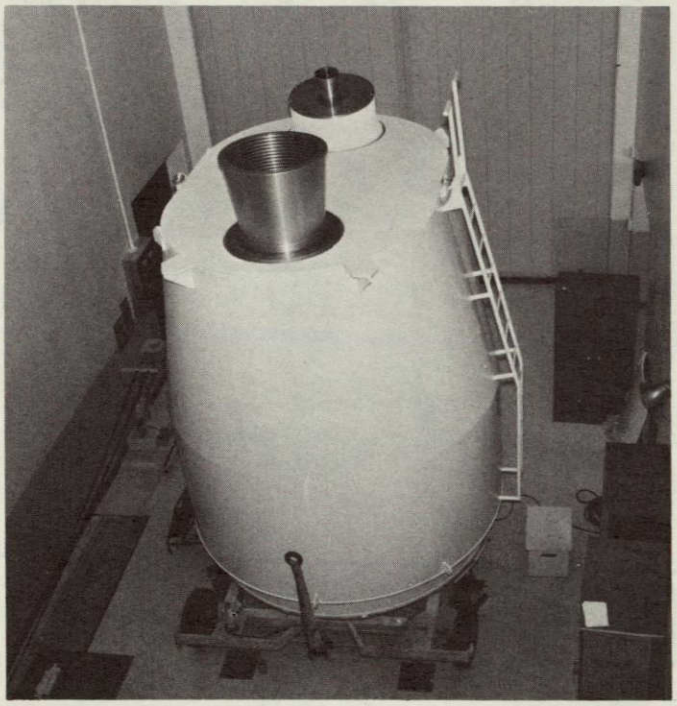

Fig. 1. SXD cone assembly

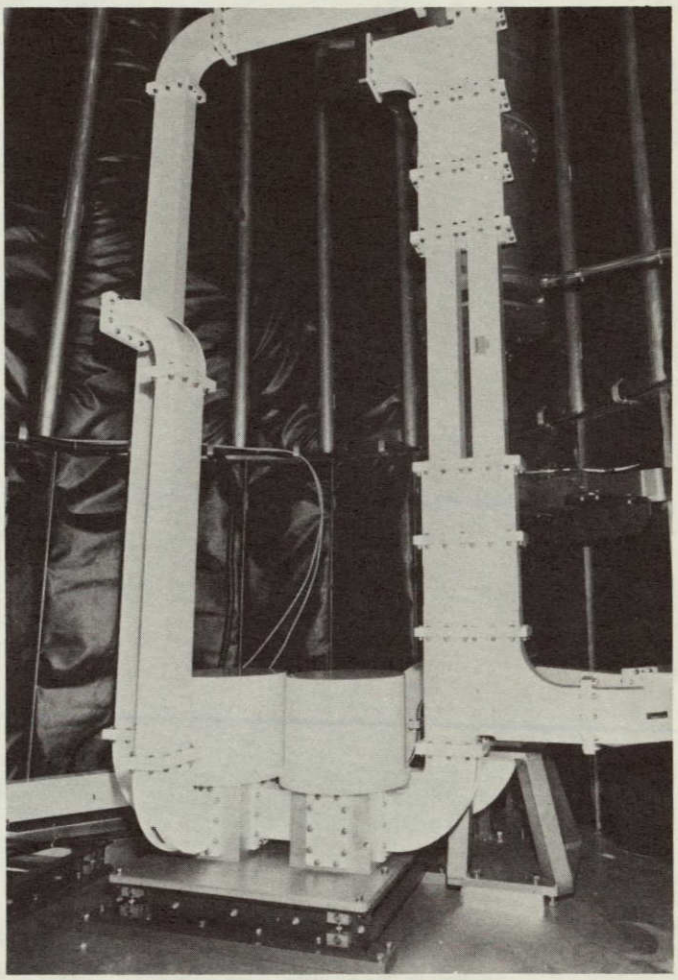

Fig. 2. Cone interior

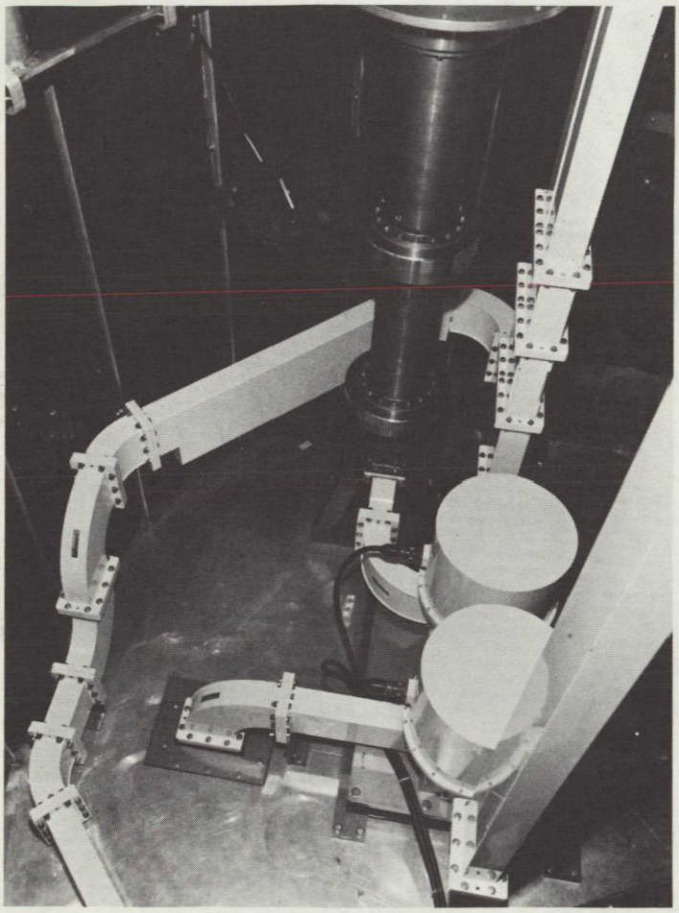

Fig. 3. Transmitter waveguide

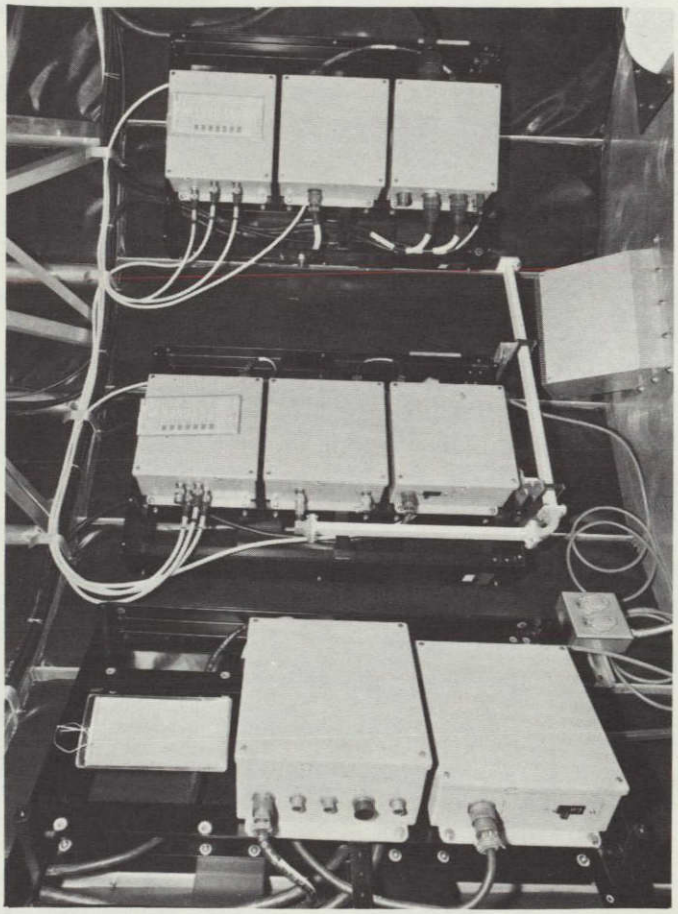

Fig. 4. Instrumentation racks

Stable Low Noise Voltage Source

G. F. Lutes
Communications Systems Research Section

Hum and noise on power sources can have a significant effect on system noise, and because it is predominately low frequency, 60 or 120 Hz, it is extremely difficult to reduce to levels in the order of 1 $\mu V/\sqrt{Hz}$, particularly at high current levels. Filtering to achieve low hum and noise is best accomplished at low current levels and should therefore be done locally. The diode regulator circuit described in this article is nearly ideal for this type of local filtering.

I. Introduction

A stable low noise voltage source has been designed for use in the Very Long Baseline Interferometry (VLBI) phase calibrator in order to reduce the hum and noise associated with typical power supplies to a level that results in a sufficiently small contribution to the phase noise on the output signal.

II. Effect of Hum and Noise

The hum and noise on the power supplies used in the phase calibrator is specified at 250 μV and is predominately at 60 Hz and 120 Hz. This noise is translated by the circuitry to phase noise on the output signal. The voltage-controlled oscillator (VCO), voltage-controlled phase shifter (VCS) and related circuitry are most susceptible to power supply hum and noise. The rest of the circuitry contributes relatively little phase noise.

If the 15-volt power supply voltage is applied to the bias input to the voltage variable capacitance diode in the VCO through a 3:1 voltage divider to provide 5 V bias, the hum and noise on the power supply is translated to sidebands at "X" band equal in amplitude to the desired calibration signal.

It is necessary to have at least a 40-dB ratio between the calibration signal and the hum and noise sidebands at X-band. To achieve this ratio, hum and noise on the power supply must be reduced by more than 50 dB before it is applied to the critical circuitry.

III. Method Used

A voltage source to supply the critical circuitry was needed with the following requirements.

(1) Low noise down to dc.

(2) Low temperature coefficient.

(3) Physically small.

(4) Low cost.

(5) Reliable.

(6) High rejection of power supply hum and noise.

Circuits were designed using constant current diodes in series with low-voltage avalanche diodes, taking advantage of the large difference in dynamic impedance of the two types of diodes to obtain a very high rejection ratio to power supply hum and noise. The rejection ratio is essentially the ratio of dynamic impedances of the two diodes.

IV. Example

An example of a practical circuit is shown in Fig. 1. It consists of a 1N5314 (4.7-mA) constant current diode in series with an LVA 347A (4.7-V) low-voltage avalanche diode. A general-purpose rectifier is placed in series with the constant current diode to protect the circuit from an inadvertent application of a negative voltage, in which case the circuit would probably be damaged.

This circuit will supply about 2 mA to a load at 4.7 V and meet the following specifications:

(1) Output noise	$<1\ \mu V/\sqrt{Hz}$
(2) Temperature coefficient	±0.01%/°C
(3) Size	0.01 $in.^3$
(4) Cost	<$10
(5) Reliability	>50,000 h MTBF
(6) Hum and noise rejection	>85 dB

The power to the VCO in the calibration generator was conditioned as shown in Fig. 2 with a primary regulator supplying power to the VCO and a secondary regulator in series with it to supply the varactor bias.

V. Tradeoffs

It is possible to make tradeoffs between hum and noise rejection, desired output current and temperature coefficient. If maximum hum and noise rejection is desirable it can be achieved by maximizing the impedance ratio between the constant current diodes and the LVA. The diode impedance curves show that for a given current, higher dynamic impedance with constant current diodes may be obtained by paralleling lower current diodes and that LVA diodes with about a 6-V avalanche voltage have the lowest impedance for a given current. Hum and noise rejection > 110 dB can be achieved.

The best temperature coefficient will be achieved using an LVA 347A (4.7-V) avalanche diode. Any constant current diode which supplies 470 μA or more when used with an LVA 347A, which has a nearly zero temperature coefficient, should result in a temperature coefficient <0.015%/°C. An order-of-magnitude improvement over this should be possible by selecting diodes.

Available output current can be increased by paralleling constant current diodes. This will result in less hum and noise rejection provided the current through the avalanche diode is not increased.

See Figs. 3 through 6 for typical parameter curves for constant current diodes and low-voltage avalanche diodes.

VI. Conclusion

Extremely low noise voltages are difficult to achieve at the level of a systems primary power supply. The large currents at this level would necessitate the use of large and expensive components.

Even if low noise voltages were achieved at this level, great care would be required in the form of careful shielding and grounding techniques to prevent excessive degradation of these voltages. Local filtering of the supply to critical circuits is a more practical approach.

The diode regulator circuit described herein works very well in this application. It achieves excellent hum and noise rejection, with good output voltage stability in a small, low-cost, reliable circuit.

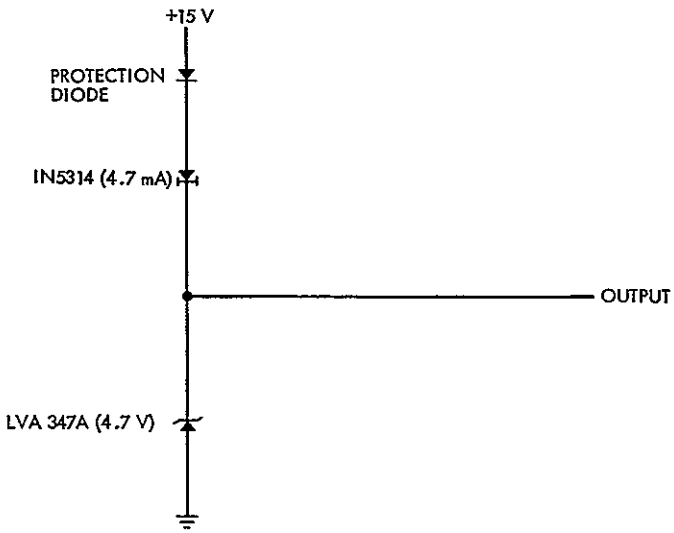

Fig. 1. Example of a practical circuit

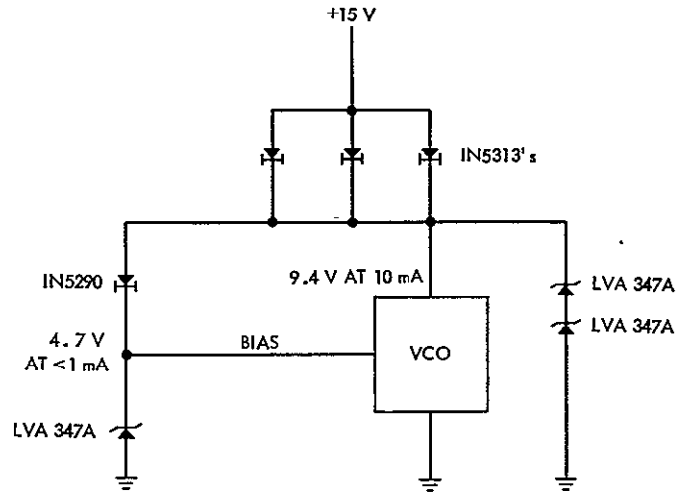

Fig. 2. Circuit used to supply power and bias to the VCO

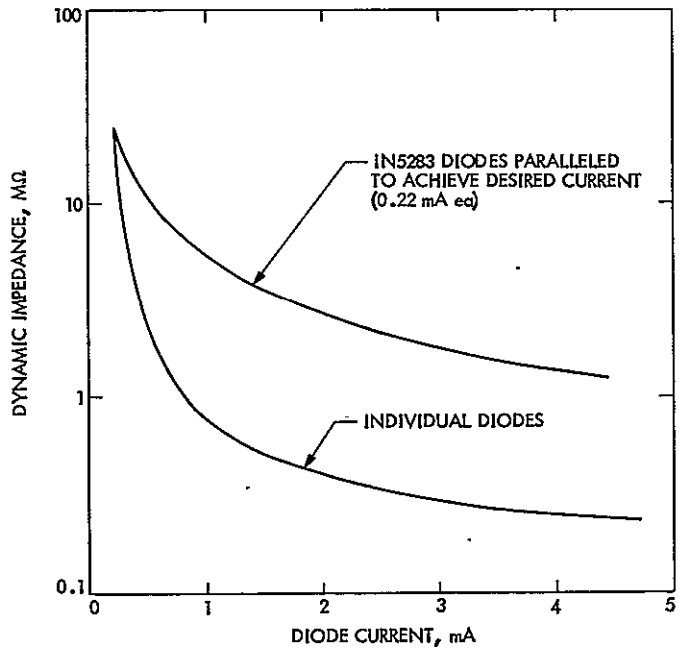

Fig. 3. Constant current diodes dynamic impedance vs current

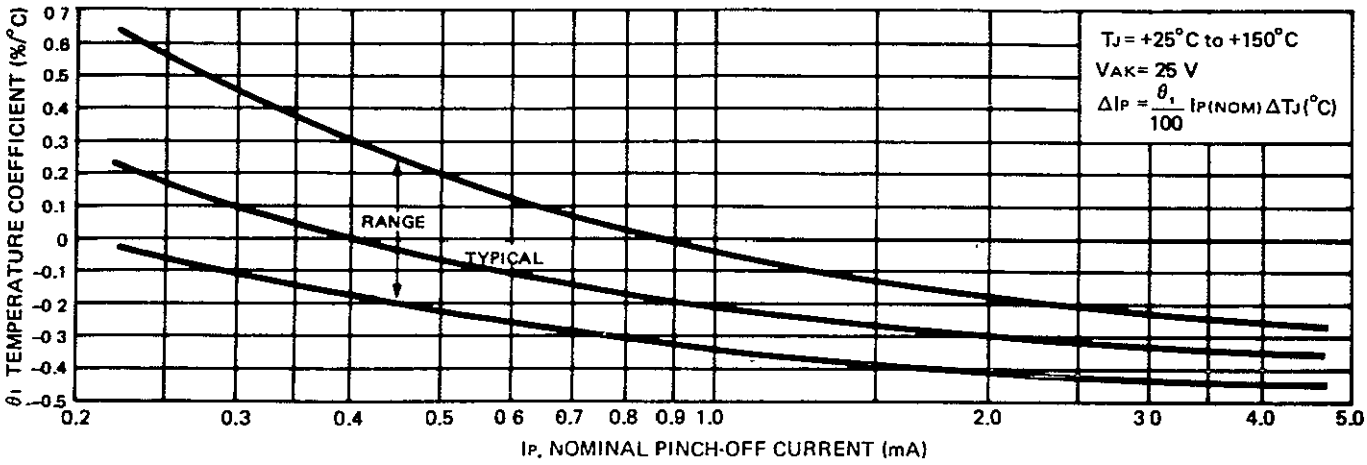

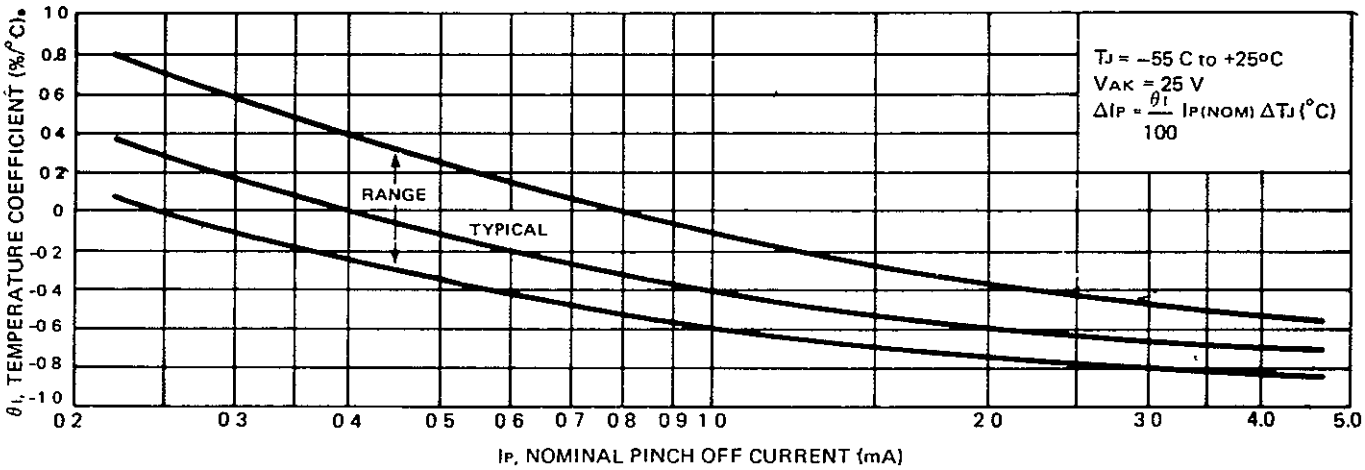

Fig. 4. Constant current diode temperature coefficient

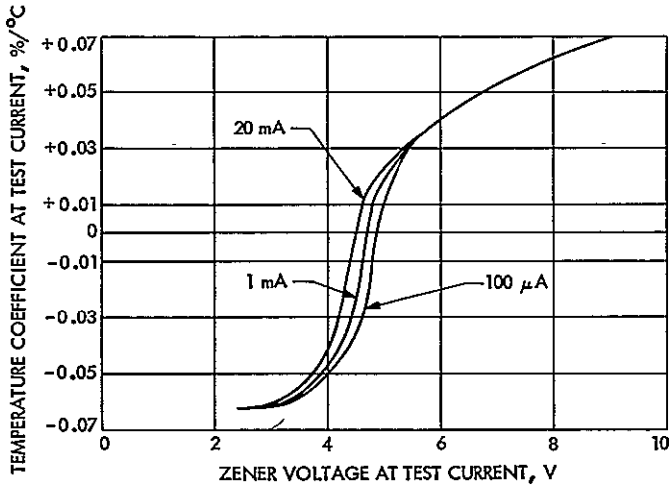

Fig. 5. LVA diode typical temperature coefficient (25 to 100°C)

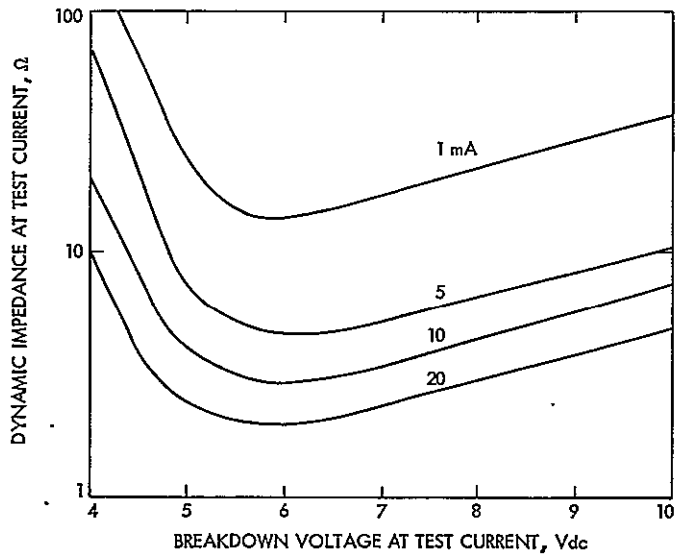

Fig. 6. LVA diode typical dynamic impedances

D15

Automated Radio Astronomy Operations

R. W. Livermore
Tidbinbilla Deep Space Communications Complex

This article describes improvements in using a computer to drive a DSN 64-meter antenna. The purpose of the development has been to simplify operation, improve antenna safety, reduce antenna wear, prevent the abuse of antenna by mis-operation, increase quantity and quality of data gathered, and give users a greater choice of automatic operations.

I. Introduction

The normal startrack method used in DSN operations has been retained. The year, station number, right ascension, declination, azimuth, and elevation are calculated and used to point the antenna. Many improvements have been added. The major additions are:

(1) Rates and acceleration are program controlled.

(2) Automatic boresite in hour angle, declination, azimuth, and elevation. Method used is to scan through a source while sampling data from an analog-to-digital converter. A curve fit of the data is used to calculate the pointing error.

(3) Limits of elevation are monitored and alarms given on the typewriter.

(4) A schedule of sources can be prepared on paper tape. Selection of tape drive will automatically steer the antenna from source to source at pre-set times.

(5) Data may be recorded on magnetic tape for post-track data reduction.

II. Controlled Rates

Increasing antenna drive velocity is performed by an addition of 0.010 degrees per second until maximum velocity of 0.200 degrees per second is reached. Table 1 shows the relationship between time, distance in degrees, and velocity in degrees per second. Figure 1 is a graph of distance in degrees versus time in seconds. Decreasing drive velocity is determined by subtraction of actual position from desired position. If the difference is greater than 2.090 degrees and maximum velocity has not been reached, the increase in velocity is maintained. If the difference is greater than 2.090 degrees and maximum velocity has been reached, maximum velocity is maintained. If the difference is less than 2.090 degrees, decreasing drive velocity is performed by using a look-up table derived from Table 1, velocity versus distance. A second-degree polynomial may be used instead of a look-up table. The coefficients have been calculated as follows:

$$v = 0.024944 + 0.141604d - 0.028102d^2$$

where

v = velocity in degrees per second
d = distance in degrees from desired position

Also, d is <2.090 degrees.

III. Calculating Offsets

The pointing accuracy of the antenna can be determined by scanning through hour angle, declination, azimuth, or elevation. The length of scan is selected from the control panel switches. To obtain very accurate pointing data, it is necessary to scan completely through a source. Consider examining a source at an elevation of 20 degrees – the data gathered from the source could look like Fig. 2. Before curve-fitting, the base and slope are subtracted from the detected output samples. Subtracting the base (a) produces Fig. 3. Subtracting the slope produces Fig. 4. Consider the original data being taken as 162 one-second samples. The slope is subtracted from every sample in the following manner:

Sample	
1	$y_1 - b$
2	$y_2 - \left\{\frac{161}{162} \times b\right\}$
3	$y_3 - \left\{\frac{160}{162} \times b\right\}$
•	•
•	•
•	•
162	$y_{162} - 0$

The maximum point of the curve is found by fitting to a second-degree polynomial. The actual formula used is:

$$x_m = \bar{x} + \frac{3}{2} \cdot \frac{3y_1 + 2y_2 + y_3 - y_5 - 2y_6 - 3y_7}{5y_1 - 3y_3 - 4y_4 - 3y_5 - 5y_7}$$

Seven points are required, and an illustration of typical sample points is given in Fig. 5. Figure 5 is a graph of a declination scan at 0.005 degrees per second through source 4C12.6. The receiver was tuned for S-band. At nominal maximum the azimuth was 332.2 degrees and elevation 34.1 degrees. The graph of Fig. 5 shows the seven sample points. The program performs a running mean of the one-second samples from the detector. Each running mean sample is the mean of seven one-second samples. The points used for the second-degree fit are seven seconds apart so all the data points are actually used. Care is needed when choosing rates and distances to scan. Useful figures are tabulated in Table 2. Shorter scans are only possible if the errors are small. Offsets from previous scans can remain in the program so that the nominal maximum occurs near the center of the scan.

IV. Schedule on Paper Tape

A program has been written for 910/920/930 computers that produces a punched paper tape of schedules for VLBIs or any other radio astronomy experiment such as Quasar Patrol. The tape can be edited, listed, or copied in advance of the experiment. A conversion routine has been included to change TTY code to the XDS code. The schedule can then be sent by line and converted to the correct format for driving the antenna. The data on the tape have a format close to the binary-coded decimal input to the Antenna Pointing Subsystem from the control panel. Parameters used are right ascension, declination, and end time of the source. Tape samples are read into the program by selecting tape drive. RA, DEC, and end time are output on the typewriter. Long schedules of over 12 hours and 100 sources have been used in practice, and proved to be more efficient and easier to run than the manual method.

V. Recording on Magnetic Tape

A 480-word record is written once per minute. Each 8-word line is one second's worth of data, consisting of day of year, time, hour angle, declination, azimuth, elevation, and sample value. The magnetic tape facility has proved to be very successful in an intensive observing period using the DSS 42/43 short-baseline interferometry. Over 350 sources were observed, and fringes have been observed in all sources.

VI. Conclusion

Using software techniques it is possible to control the 64-meter antenna safely and automatically. Wear and tear are greatly reduced. Better use is made of scheduled time, thus increasing productivity.

Acknowledgment

Thanks are due Dr. D. L. Jauncey (Australian Commonwealth Scientific Industrial Research Organisation) for valuable advice on desirable methods of star tracking.

Table 1. Time, distance, and velocity from static start

Time, s	1	2	3	4	5	6	7	8	9	10	11	12	13	14	15	16	17	18	19	20
Distance, deg	0.01	0.03	0.06	0.10	0.15	0.21	0.28	0.36	0.45	0.55	0.66	0.78	0.91	1.1	1.2	1.4	1.5	1.7	1.9	2.1
Velocity, deg/s	0.01	0.02	0.03	0.04	0.05	0.06	0.07	0.08	0.09	0.10	0.11	0.12	0.13	0.14	0.15	0.16	0.17	0.18	0.19	0.20

Table 2. Time required for various scans (distance must be exactly divisible by rate)

Band	Rate, deg/s	Distance off, deg	Time required, min:s
S	0.005	0,300	2:32
S	0.004	0.244	2:22
S	0.003	0.090	1:08
X	0.001	0.083	2:54
X	0.001	0.034	1:15

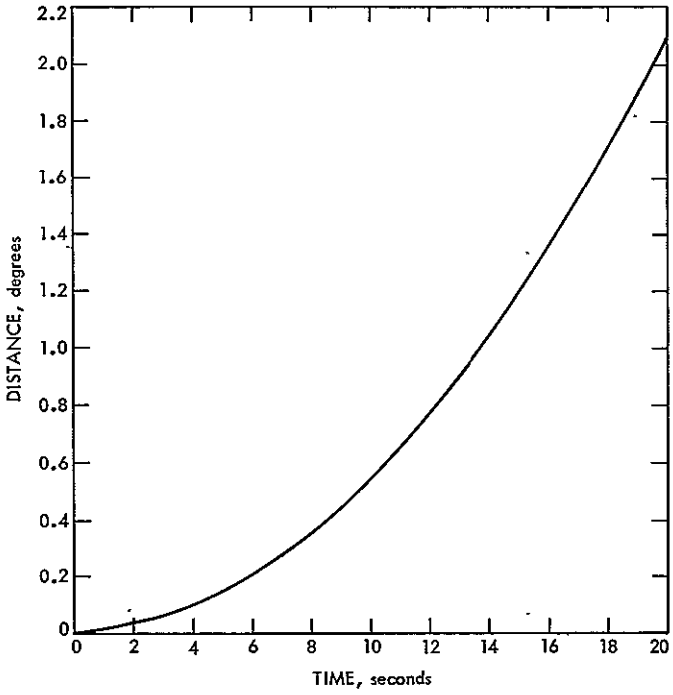

Fig. 1. Distance from static position versus time

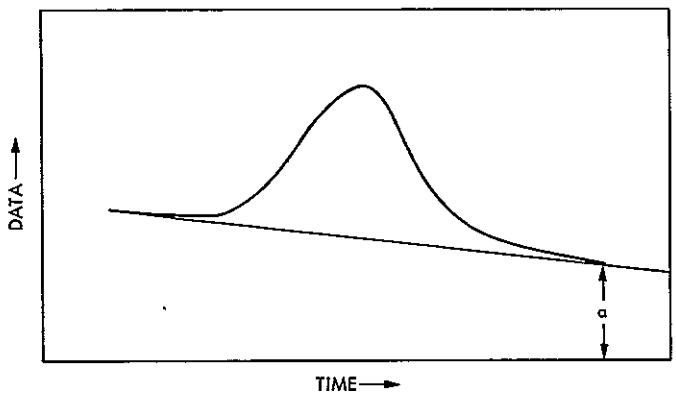

Fig. 2. Square law detector output versus time (S-band total scan is 0.5 deg at 0.004 deg/s)

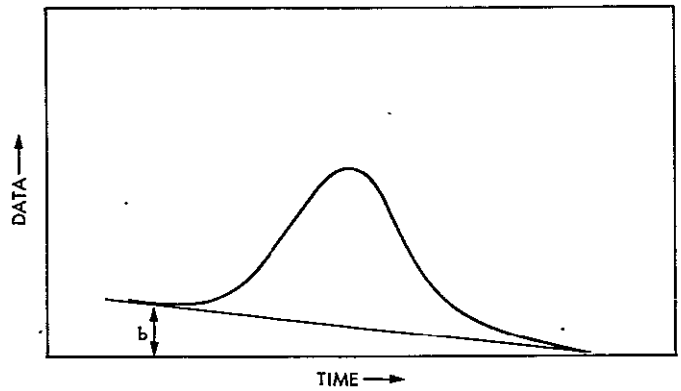

Fig. 3. Bias subtracted from gathered data

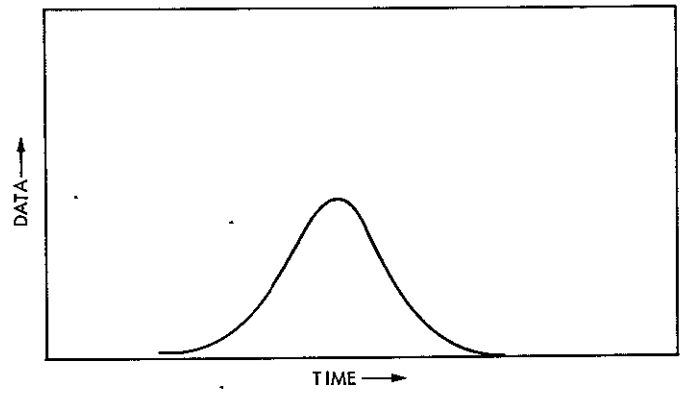

Fig. 4. Slope and bias subtracted from gathered data

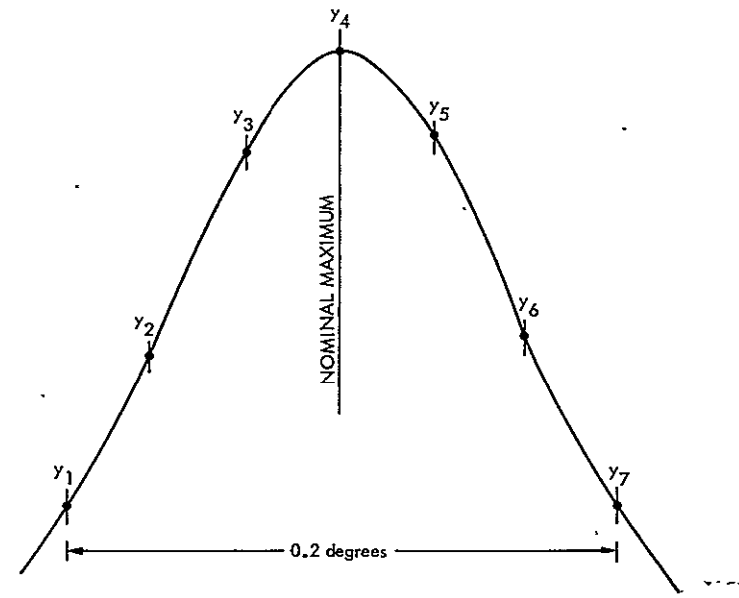

Fig. 5. Actual graph of a declination scan through source 4C12.6 at rate of 0.005 deg/s (slope and bias have been subtracted by pointing program)